Experimental investigation of seawater cooling during severe accidents in a nuclear reactor

by

Zayed Ahmed

M.S., Kansas State University, 2017

AN ABSTRACT OF A DISSERTATION

submitted in partial fulfillment of the
requirements for the degree

DOCTOR OF PHILOSOPHY

Alan Levin Department of Mechanical and Nuclear Engineering
Carl R. Ice College of Engineering

KANSAS STATE UNIVERSITY
Manhattan, Kansas

2022

Abstract

During the Fukushima Daichii nuclear accident, seawater was injected into the reactor core to cool the decay heat generated from the nuclear fuel elements. The impact of dissolved salts in water on the coolability is not well understood, especially on the heat generating porous debris bed, that is expected to form in severe accident scenarios. Under the boiling conditions with seawater, the presence of dissolved salts is expected to impact the heat transfer and hydrodynamic characteristics of the cooling process. The focus of this experimental work is to measure the differences in the cooling performance between seawater and pure water in two geometries - an annulus and an emulated debris bed. Insights from experiments on the annular test section inform the heat transfer degradation of using seawater under different scenarios. The contribution of the boiling mechanism to the total heat removal rate is quantified through high speed image analysis. The experimental setup designed to study debris bed coolability through high spatial resolution temperature measurements and novel void fraction measurements is discussed. The sustainable cooling of the porous debris bed using emergency cooling water requires the continuous supply of coolant to all regions within the bed to prevent a dryout. This dryout is measured using Distributed Temperature Sensing (DTS) and pressure drop measurements and the heat flux at which dryout occurs is quantified at various parameters and salt concentrations. An increase in coolability was observed to occur with an increase in the dissolved salt concentration. First of a kind, non-intrusive void fraction measurements were performed inside the debris bed by utilizing thermal neutrons of the KSU Triga Mark II nuclear reactor. The classical models for estimating the void fraction inside the boiling debris bed were validated for the first time ever. This study gives modelers high fidelity temperature and void fraction data for model validation. From a reactor safety point of view, this work suggests that using seawater has

short term cooling benefits by enhancing the dryout heat flux, but longterm cooling can be limited due to the plugging of pores, which can cause further progression of an accident.

Experimental investigation of seawater cooling during severe accidents in a nuclear reactor

by

Zayed Ahmed

M.S., Kansas State University, 2017

A DISSERTATION

submitted in partial fulfillment of the
requirements for the degree

DOCTOR OF PHILOSOPHY

Alan Levin Department of Mechanical and Nuclear Engineering
Carl R. Ice College of Engineering

KANSAS STATE UNIVERSITY
Manhattan, Kansas

2022

Approved by:	Approved by:
Co-Major Professor Hitesh Bindra	Co-Major Professor Steven Eckels

Copyright

Abstract

During the Fukushima Daichii nuclear accident, seawater was injected into the reactor core to cool the decay heat generated from the nuclear fuel elements. The impact of dissolved salts in water on the coolability is not well understood, especially on the heat generating porous debris bed, that is expected to form in severe accident scenarios. Under the boiling conditions with seawater, the presence of dissolved salts is expected to impact the heat transfer and hydrodynamic characteristics of the cooling process. The focus of this experimental work is to measure the differences in the cooling performance between seawater and pure water in two geometries - an annulus and an emulated debris bed. Insights from experiments on the annular test section inform the heat transfer degradation of using seawater under different scenarios. The contribution of the boiling mechanism to the total heat removal rate is quantified through high speed image analysis. The experimental setup designed to study debris bed coolability through high spatial resolution temperature measurements and novel void fraction measurements is discussed. The sustainable cooling of the porous debris bed using emergency cooling water requires the continuous supply of coolant to all regions within the bed to prevent a dryout. This dryout is measured using Distributed Temperature Sensing (DTS) and pressure drop measurements and the heat flux at which dryout occurs is quantified at various parameters and salt concentrations. An increase in coolability was observed to occur with an increase in the dissolved salt concentration. First of a kind, non-intrusive void fraction measurements were performed inside the debris bed by utilizing thermal neutrons of the KSU Triga Mark II nuclear reactor. The classical models for estimating the void fraction inside the boiling debris bed were validated for the first time ever. This study gives modelers high fidelity temperature and void fraction data for model validation. From a reactor safety point of view, this work suggests that using seawater has

short term cooling benefits by enhancing the dryout heat flux, but longterm cooling can be limited due to the plugging of pores, which can cause further progression of an accident.

Table of Contents

List of Figures

List of Tables

Nomenclature

C_p	Specific heat at constant pressure [J/kg K]
d	Particle diameter [m]
D_d,D_b	Bubble departure diameter [m]
D_h	Hydraulic diameter [m]
d_i	Inner diameter of annulus; heater outer diameter [m]
d_o	Outer diameter of annulus [m]
F	Enhancement factor
f	Frequency of bubble departure [s^{-1}]
f_{tp}	Two phase friction factor
G	Mass flux [kg/m^{2}s]
H	Debris bed height [m]
h	Heat transfer coefficient [W/m^2 K]
h_{fg}	Latent heat of vaporization [J/kg]
I	Intensity after attenuation
I_0	Intensity of the beam before attenuation
j	Superficial velocity [m/s]

$J(\alpha)$	Leverett function
K	Permeability
k	Thermal conductivity [W/m K]
K_{rv}	Relative permeability of vapor
L_c	Chord length [m]
m_l	Mass flow rate [kg/s]
N	Number of active nucleation sites [m^{-2}]
P	Pressure [Pa]
P_a	Pixel intensity at 100% void fraction
P_c	Capillary pressure [Pa]
P_f	Pixel intensity of two phase flow
P_w	Pixel intensity at 0% void fraction
q''	Heat flux [W/m^2]
q''_E	Evaporative heat flux [W/m^2]
Q	Power input into heater [W]
r_c	Radius of cavity [m]
S	Suppression factor
T	Temperature [K]
U	Overall heat transfer coefficient [W/m^2 K]
V	Fluid velocity [m/s]

x	Vapor quality
z	At axial elevation [m]
z	Elevation [m]
Bo	Boiling number $\left(q''/m_l h_{fg}\right)$
Re	Reynolds number $\left(\rho_i V(D-d)/\mu_i\right)$

Greek letters

α	Void fraction
δ	Distance between thermocouple and wall [m]
ϵ	Debris bed porosity
η	Passability
η_0	Induction heating efficiency
η_{rv}	Relative passability of vapor
μ	Viscosity [Pa s]
∇	Gradient
ψ	Coefficient in Shah correlation
ρ	Density [kg/m^3]
ρ_H	Homogeneous density [kg/m^3]
σ	Surface tension [N/m]

Subscripts

exp	Experimentally measured

i	At inlet
l	Liquid
o	At outlet
sp	Single phase
sub	Subcooling
TC	At thermocouple location
tp	Two phase flow
v	Vapor
w	Wall

Acknowledgments

I would like to acknowledge Department of Energy- Nuclear Energy University Program for sponsoring this project. First and foremost, I would like to thank my advisors, Dr. Steven Eckels and Dr. Hitesh Bindra for their invaluable guidance and support in all technical and non-technical matters during my PhD journey. I am grateful to them for their resourcefulness, for setting up a streamlined project and for directing me until the completion, even through the turbulent times of Covid-19 and lockdowns. I am thankful to my committee members Dr. Terry Beck and Dr. Behzad Ghanbarian for their in depth knowledge and guidance in tackling challenging problems related to this research. I would like to thank Dr. Alan Cebula for helping conduct the neutron imaging experiments using the nuclear reactor. I am thankful to Jim Hodgson for manufacturing and repairing glass tubes time and time again. I am thankful to my lab mates: Daniel Franken, Abhinav Gairola, Daniel Gould, Molly Ross, Broderick Sieh, Ruhania Tarannum, Brendan Ward, and Isaiah Wicoff for providing all the help and assistance in conducting experiments and for all the fruitful and productive discussions. I would like to thank my friends Shahid Hossaini and Syed Asrar Ahmed for their moral support through the grind. Finally, I express my profound gratitude to my parents, for their unwavering support and love through all these years. This work would not have been possible without their constant encouragement and valuable guidance.

Chapter 1

Introduction

1.1 Background

Guidelines for Nuclear Reactor safety during an accident require the shutdown of the reactor, to ensure termination of the nuclear fission reaction. However, a significant amount of decay heat is generated continuously within the reactor core even after its shutdown. Removing this decay heat through proper cooling is important to prevent local temperature excursion that can cause a meltdown of the reactor core. In the Fukushima Daichii nuclear accident following the Loss of Coolant from the core, seawater was injected into the reactor to cool the decay heat generated by the nuclear fuel elements as an emergency measure[12–14]. However, very little is known of the efficacy of the cooling process of seawater and to what extent seawater injection contributed to the progression of the accident. Understanding the coolability effects of seawater or raw water in nuclear reactors is important because many nuclear power plants are located close to large water bodies, which presents the option to use raw water as an emergency coolant, in extreme accident scenarios.

During a Loss of Coolant Accident (LOCA) in a Nuclear Reactor, various stages of the accident are anticipated. In the early stages, the loss of coolant causes the intact fuel rods in the reactor to heat up due to their self generated decay heat. This decay heat is $< 5\%$ of the heat generation density in the core during nominal operation and decays exponentially with time. If this heat is not removed, the fuel rods overheat reaching temperatures greater than 1500°C. The resulting molten mass of fuel rods combines with the surrounding support structures and forms a molten mass referred to as *Corium*. Many reactors have an emergency containment pool below the Reactor Vessel for containing the molten Corium during accidents. This molten Corium combines with the coolant and forms a granular structure containing particles of various sizes, referred to as a *Debris Bed*. This debris bed continues to generate decay heat due to the presence of the fissile material and needs to be cooled continuously to prevent further progression towards melt concrete interaction. Insufficient cooling of the debris bed can lead to a breach of the containment and the nuclear material in the debris bed can contaminate the underlying soil and any underlying water bodies, leading to catastrophic scenarios[15;16].

Therefore knowing the cooling limit of a debris bed is extremely important. With the use of seawater as a coolant, many negative impacts on coolability are anticipated over the long and short term. The dissolved salts in seawater can precipitate out and deposit on the heat transfer surfaces creating a thermal resistance caused by the low thermal conductivity of the deposited salts. This process is usually referred to as *Fouling*[17]. The presence of the dissolved salts also creates unique two phase flow characteristics which would alter the hydrodynamic behavior of the flow, which may lead to deterioration of the coolability of the reactor[18]. These cooling characteristics of seawater need to be assessed, and the limiting conditions specified, if seawater has to be considered as an emergency coolant during nuclear accidents.

Very few studies exist in literature where the cooling characteristics of seawater are studied. In particular there are no existing reports in literature where the cooling characteristics of seawater on a porous debris bed are investigated. This study presents an experimental study on the cooling performance of seawater in an emulated debris beds. The experimental findings from this study present the first ever experimental report of seawater related thermal-hydraulic behavior on debris bed coolability that can be used to validate various models and also identify the limiting phenomena associated with seawater cooling related to nuclear reactor safety.

1.2 Seawater as a heat transfer fluid

Seawater, the most abundant form of water on earth, has multiple dissolved ionic constituents. These dissolved ionic constituents vary slightly in concentration across various locations on the planet, but can be generalized to have a fixed global composition represented in Figure 1.1[19]. The majority of the ions are Na^+ and Cl^- but the presence of other ionic constituents can have a significant impact for heat transfer applications. These dissolved constituents can crystallize and form a mixture of positive solubility and inverse solubility salts, where the former means that the solubility increases with the solution temperature and latter means that the solubility decreases with the solution temperature. Studies with

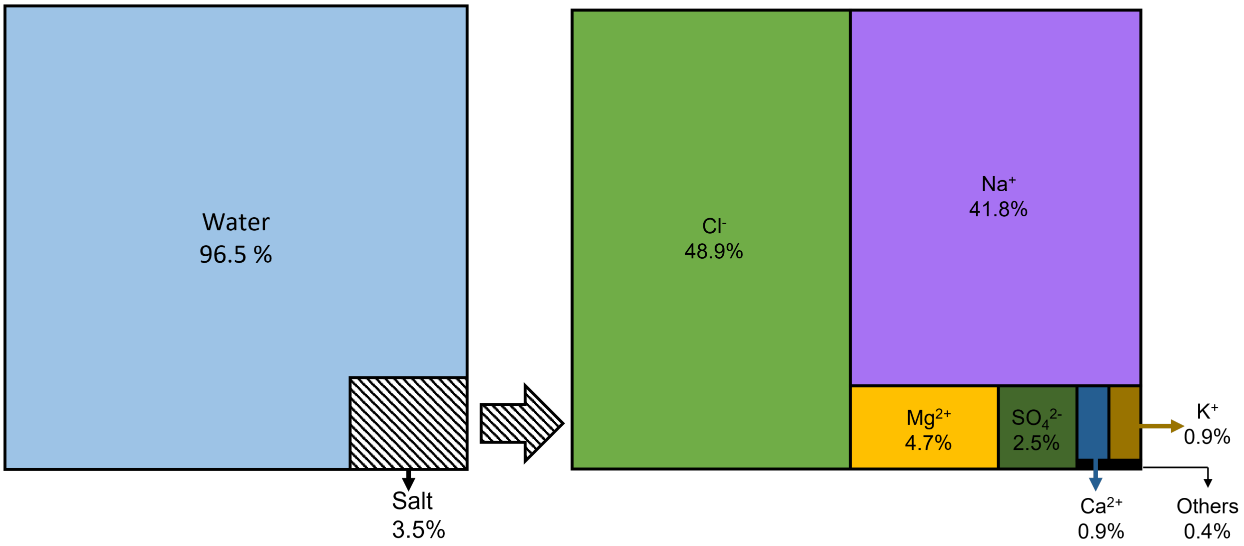

Figure 1.1: *Ionic composition of seawater*

drying of seawater with a focus on the crystallization sequence have shown that Calcium Carbonate and Magnesium Carbonates precipitate out first in small amounts followed by Calcium Sulphate and the major constituent, Sodium Chloride[20–22].

The presence of ionic constituents in water has little effect on its thermophysical properties. The thermophysical properties for pure water and seawater at a salinity of 35g/L, are specified in Table 1.1. This implies that in the absence of phase change, the single phase heat transfer performance of seawater should be similar to that of pure water.

The heat transfer in single phase flow is dictated by the thermophysical properties, and single phase heat transfer can be easily modeled as a pure water system. However, in the presence of boiling, significantly different characteristics are observed. During boiling, the conversion of liquid ionic solution to vapor causes the local concentration of the dissolved constituents in the microlayer beneath the bubble to increase beyond the solubility limit , causing the precipitation of the dissolved constituents from the solution[23]. Some of these precipitates deposit on the heat transfer surface and some get resuspended back into the solution. This high concentration in the microlayer causes the dissolved ions to diffuse from the microlayer to the bulk liquid, simultaneously as the liquid diffuses from the bulk liquid to the microlayer. The diffusion of the liquid into the microlayer therefore gets restricted,

Table 1.1: *Thermophysical properties of seawater at 25°C and 1 atm*[9].

Property	**Pure water, C = 0%**	**Seawater, C = 3.5%**
Density (kg/m^3)	997	1023.6
Specific heat capacity (J/kg K)	4184	4000.8
Thermal conductivity (W/m K)	0.60	0.60
Dynamic viscosity $\times 10^3$ (kg/m s)	0.89	0.96
Surface tension $\times 10^3$ (N/m)	72.0	73.1
Boiling point (°C) at 1 atm	100.0	100.3

thereby causing a reduction in heat transfer in salt solutions. This reduction in heat transfer in electrolyte solutions has been reported in several studies[24–29].

Several studies exist in literature where single electrolyte solutions were used to study the boiling performance[30–33], but very few studies exist where seawater was taken into consideration. Single electrolyte solutions have differing heat transfer performance depending on the kind of electrolyte used[34], but with a complex combination of these electrolytes, the cooling performance in not well understood. Studies on seawater cooling have reported the steady state heat transfer coefficients for varying parameters[27;35]. These studies were performed under high pressure, high mass flux scenarios, which are not representative of Nuclear accident scenario. Alongside the heat transfer coefficient measurements, dissecting the total heat transfer rate into the evaporative and convective component helps in gaining a deeper understanding of the cooling mechanism. This can be achieved by quantifying the bubble nucleation parameters through techniques like high speed imaging and image processing[36;37]. The work presented Chapter 2 in this thesis focuses on quantifying the heat transfer and two phase flow characteristics during flow boiling in a vertical annulus. The insights from these experiments inform the expected heat transfer behavior of seawater during nucleate boiling. Results from these experiments in a simple geometry provide insights into the boiling process associated with the complex geometry of a porous debris bed.

1.3 Boiling in a porous debris bed

To gain an understanding of the effects of seawater cooling in a porous debris bed, the cooling mechanisms and the limiting conditions without the dissolved salts needs to be understood. The cooling in a debris bed is a complex phenomena due to the complex interaction between the liquid, vapor and solid phase within the system.

A stable and coolable condition can be achieved only if the evaporated liquid in the bed is continuously replaced by additional cooling water percolates into the bed from the overlying pool[38]. During stable conditions, a steady liquid and vapor counter-current flow is established in the bed where the liquid percolation downwards into the bed and the vapor travels upwards out of the bed. To maintain steady cooling, it is necessary that the vapor generated is able to exfiltrate the bed and the liquid is able to penetrate the bed. Failure to reach a steady counter-current flow can cause a lack of cooling in some regions of the bed where the liquid fails to percolate. This lack of liquid penetration can cause local temperatures to increase rapidly in the bed, and this can cause remelting of the core and progresses the accident further. This process is usually referred to as dryout, and the maximum heat that can be removed from the debris bed in stable boiling conditions is called the dryout heat flux[38–40].

For heat fluxes higher than the critical dryout heat flux, the higher amount of vapor generation in the pores of the debris bed causes the void fraction and mass flux of vapor to increase. This causes an increase in flow resistance to the percolating liquid in the bed, which causes the mass flux of cooling water penetrating the bed to decrease. This reduced mass of water penetrating the bed boils off before wetting all parts of the bed, which leads to certain regions of the bed becoming dry. The only dominant mode of heat transfer in these dry zones is through conduction heat transfer into the nearby structures and through convection heat transfer into the vapor phase. These modes of heat transfer, not being as effective as boiling heat transfer, cause the local temperature in the bed to rapidly rise, which has the potential to further progress the meltdown of the reactor[41;42]. This process is illustrated in Figure 1.2. Several experiments in literature have characterized the dryout heat flux of a

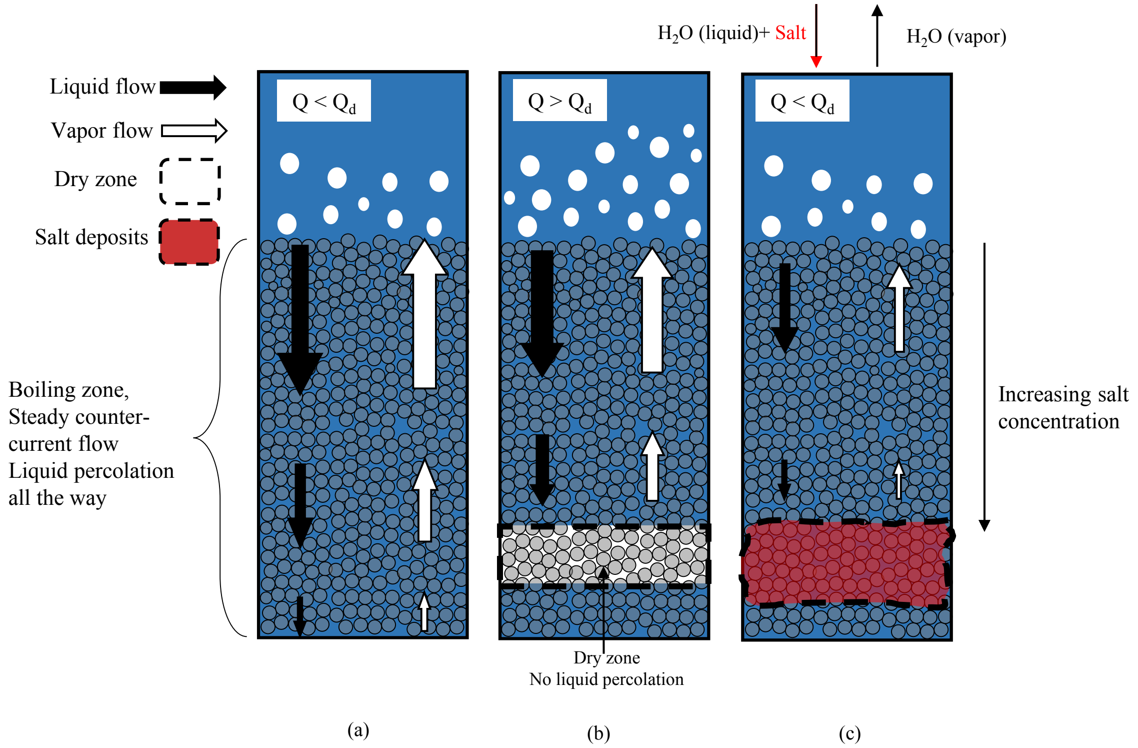

Figure 1.2: *(a) A steady counter current flow is established in a boiling debris bed for heat flux (Q) lower than the critical dryout heat flux (Q_d). (b) Liquid percolation is restricted due to high amount of vapor generation causing dryout ($Q > Q_d$) (c) Salt deposits in the pores with seawater.*[1]

debris bed as a function of various system parameters. However, there is still uncertainty in the measurement of dryout heat flux and different experimental facilities present different dryout heat flux. One of the reasons for this uncertainty is the low spatial resolution of the temperature measurement. Low spatial resolution leads to over prediction of the dryout heat flux[43].

With the addition of salts, the changes in heat transfer and hydrodynamic characteristics can have an impact on the short term cooling behavior of a debris bed with seawater, especially the dryout heat flux. The fouling or the deposition mechanism of salts over time can cause the geometric and thermal characteristics of the porous medium to change over time. This deposition of salts on the heat transfer surface can degrade the heat transfer over time and can lead to plugging of the pores, leading to additional complexities in the cooling of a debris bed. This is schematically represented in Figure 1.2. To date, no study exists in literature where the performance of seawater in a boiling packed bed of spheres is studied. This is one of the first experimental works with a focus on providing debris bed experimental data with a high spatial resolution along side the first ever work to quantify the void fraction within a boiling debris bed.

1.4 This work

The prime motive of this work is to understand the cooling performance of seawater in debris beds to inform nuclear reactor safety decisions during a severe accident. There is a long history of studying the debris bed coolability specifically with a focus on the dryout heat flux, but there exists several uncertainties and scatter in data due to the intrusive nature of the spatially sparse instrumentation[40;43]. There are also no studies focused on evaluating seawater behavior on cooling a debris bed during accidents. Understanding cooling of seawater in a debris bed can define the limiting conditions with regards to reactor safety and present an idea of the feasibility of using seawater in accident scenarios.

The remainder of the thesis is divided up into 4 chapters. Chapter 2 focuses on presenting the experimental studies that were undertaken to understand the boiling behavior of seawater in a simplified geometry, the vertical annulus. The thermal response or the heat transfer coefficients along with the nucleate boiling bubble characterization are quantitatively presented. Chapter 3 focuses on the development of the experimental setup used to study debris bed cooling. The design criteria to build an emulated debris bed along with an array of important instrumentation is presented. In chapter 4, the experimental results showing the cooling performance of the debris bed under a range of heat fluxes ranging from below the critical dryout heat flux, to heat fluxes much higher than the dryout heat flux are presented. A combination of high resolution temperature measurements and state of the art non-intrusive void fraction measurements using the KSU neutron imaging facility are leveraged to draw a deeper understanding of the boiling heat transfer and two phase flow phenomena in a decay heat generating debris bed. The conclusions of this research work and the future recommendations are given in chapter 5.

Chapter 2

Influence of dissolved salts on nucleate boiling

2.1 Introduction and objectives

As mentioned earlier, seawater has its thermophysical properties very similar to that of pure water. Thus the single phase heat transfer performance is very similar with or without salts. Single phase experiments performed by Uesawa et al.[44] on a single heated rod in a vertical annulus have shown that the thermal-hydraulic behavior of seawater is very similar to pure water at varying heat fluxes and mass fluxes. However, the formation of vapor during nuclear boiling has been shown to alter the heat transfer characteristics[45].

Nucleate boiling experiments with single constituent electrolyte solutions have shown different heat transfer limiting mechanisms depending on whether the solute has positive solubility or inverse solubility. Experiments with positive solubility salts have shown that the heat transfer is reduced as compared to its pure water counterpart. This reduction in heat transfer was attributed to the limiting diffusion process in the microlayer as described previously. However, no deposits on the heat transfer surface were observed in presence of positive solubility salts[30;31]. For inverse solubility salts, lower heat transfer coefficients were reported and this reduction in heat transfer coefficient exacerbated with time. This was attributed to the deposition of the precipitates on the heat transfer surface along with the mass transfer resistance in the microlayer[32].

Because seawater is a complex combination of positive and inverse solubility salts, single constituent studies may not be sufficient to study the effect of multiple dissolved salts on the heat transfer performance. Although the major constituent of seawater is NaCl, Huang et al.[31] demonstrated that seawater boiling cannot be simulated using NaCl solution of similar concentration. The primary compounds to deposit on the heater surface have been shown to be Calcium Sulphate and Calcium Carbonate[45]. These compounds deposit on the heater surface and grow, causing a deterioration of heat transfer coefficient over time. A linear increase of the Fouling factor with time was reported in experiments conducted in a vertical annulus[46]. This deterioration in heat transfer has been shown to linearly increase with the dissolved salt concentration. On shorter time scales, the heat transfer coefficient in seawater was reported to be lower than pure water[26], similar to single electrolyte studies.

This chapter presents the results from an experimental study performed in an annular experimental loop built to emulate the nuclear fuel rods. Experimental results are presented that characterize the hydrodynamic and heat transfer characteristics of seawater from flow boiling experiments under steady flow conditions. These experiments were conducted using Artificial Seawater and comparisons of the thermal hydraulic behavior were drawn with pure water.

2.2 Experimental setup

The schematic of the experimental setup is shown in Figure 2.1. The liquid flows in a closed loop that consists of pump, the heat exchanger/condenser and the annular test section along with various instrumentation. A centrifugal pump drives the flow in the system allowing to reach a maximum Reynolds number of 15,000. The condenser is a 316L shell and tube heat exchanger with a heat transfer area of 0.25 m^2. The secondary side of the heat exchanger utilizes a flow temperature control unit to regulate the inlet temperature to the heat exchanger on the secondary side. The temperature of the fluid on the secondary side can be adjusted to get a maximum test section inlet temperature of 358 K on the primary side.

The test section consists of a 1.2 m high borosilicate glass tube with an inner diameter of 25.4 mm. The glass tube encompasses a cartridge heater 0.6 m tall with an outer diameter of 15.8 mm. This leads to a hydraulic diameter in the annular gap as 9.6 mm. The heater is constant heat flux device that is powered by a DC power supply unit with the maximum output of 2.5 kW thermal power, equivalent to 92 kW/m^2.

Various instruments are placed along the loop to record the relevant thermal hydraulic parameters. The flowrate is measured by means of a coriolis flowmeter that is placed in the single phase region after the condenser and before the test section. Two RTD temperature probes measure the temperature of the fluid at the inlet and outlet of the test section respectively. The pressure is also monitored at the inlet and outlet of the test section. The voltage and current going into the heater are measured to estimate the total power being transferred by the DC power supply. A 4-electrode electrical conductivity probe is placed

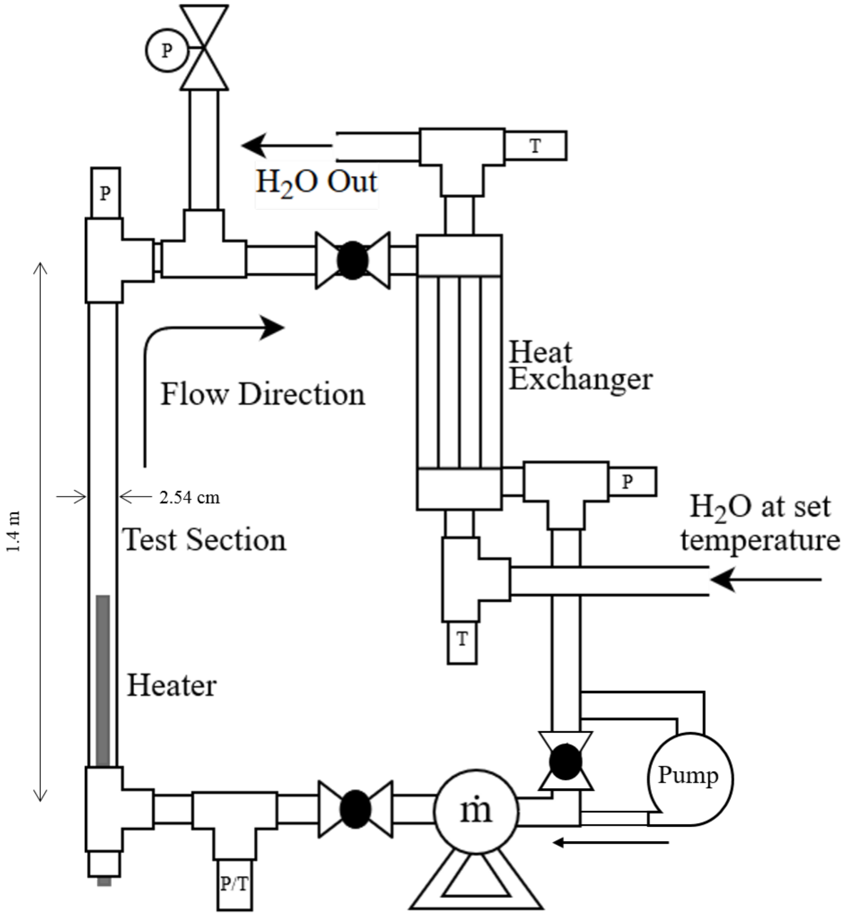

Figure 2.1: *Schematic of the experimental setup.*

before the test section to monitor the salinity of the fluid solution.

The heater has three K-Type thermocouples embedded at various axial locations that measure the local temperature in the heater. The schematic of the heater with the embedded thermocouples is shown in Figure 2.2. The calibration of the heater thermocouples was performed using the Wilson plot method which is discussed in the next section. The uncertainty associated with various flow measurement instruments are shown in Table 2.1.

Table 2.1: *Uncertainty associated with each instrument.*

Instrumentation	**Uncertainty**
Emerson Coriolis Flow Meter	±0.03 g/s
Emerson Conductivity Probe	±4% of reading
Type K Thermocouples	±2.2°C
Pressure Transducers	±0.4% FS
Variac Power Output	±30 W

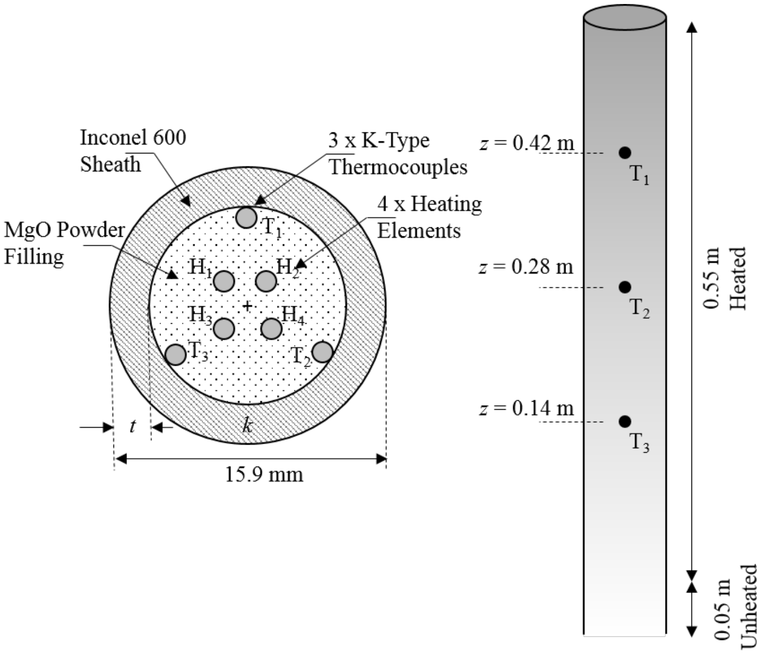

Figure 2.2: *Schematic of the heater showing the locations of the thermocouples.*

2.3 Methodology

2.3.1 Preparation of Artificial Seawater

The seawater solution was prepared by using a commercially available product called Instant Ocean, which was mixed in Deionized water at 3/5 % wt/L. The solution was mixed and left for aeration with a stirrer for 18 hours prior to a test to ensure proper mixing of the solution. This product has been shown to be a good substitute for seawater, with its composition the closest to the global average composition of seawater. The concentration of the major ions is compared with global seawater composition in Table 2.2.

2.3.2 Wall temperature estimation using Wilson Plot technique

The temperatures measured by the heater thermocouples are higher than the wall or surface temperature due to the internal radial heater resistance (as shown in Fig. 2.2). The Wilson plot[47] technique involves estimating the heater wall thermal resistance and in turn wall temperatures from thermocouple measurements obtained during calibration experiments per-

Table 2.2: *Concentration of major ionic constituents in mmol kg^{-1} present in seawater and Instant Ocean*[10].

Ions	Seawater	Instant Ocean
Na^+	470	462
K^+	10.2	9.4
Mg^{2+}	53	52
Ca^{2+}	10.3	9.4
Cl^-	550	521
$SO_4{}^{2-}$	28	23
$HCO_3{}^-$	1.90	1.90

formed with different flow rates and fixed heat flux levels. The relation between the measured temperature, the wall temperature and the heat flux can be written as:

$$q'' = h(T_w - T_l) = U(T_{TC} - T_l) = \frac{k}{\delta}(T_{TC} - T_w) \tag{2.1}$$

where q'' is the heat flux, h is the heat transfer coefficient between the heater wall and the fluid, T_w is the wall temperature, T_l is the fluid temperature, U is the overall heat transfer coefficient, T_{TC} is the temperature measured by the thermocouple, k is the thermal conductivity of the heater material and δ is the radial distance between the thermocouple and the outer heater wall. As $\delta << r_o$, the planar wall assumption can be applied to achieve the expression for the overall heat transfer coefficient can be written as:

$$\frac{1}{U} = \frac{1}{h} + \frac{\delta}{k} \tag{2.2}$$

The heat transfer coefficient, h is usually obtained from dimensionless correlations where the Nusselt number is correlated as a function of the Reynolds number and Prandtl number. In the widely accepted forced convection correlations, such as the Dittus-Boelter correlation or Seider-Tatte correlation, the heat transfer coefficient h is related to Reynolds number as:

$$h \propto \mathbf{Re}^{0.8} \tag{2.3}$$

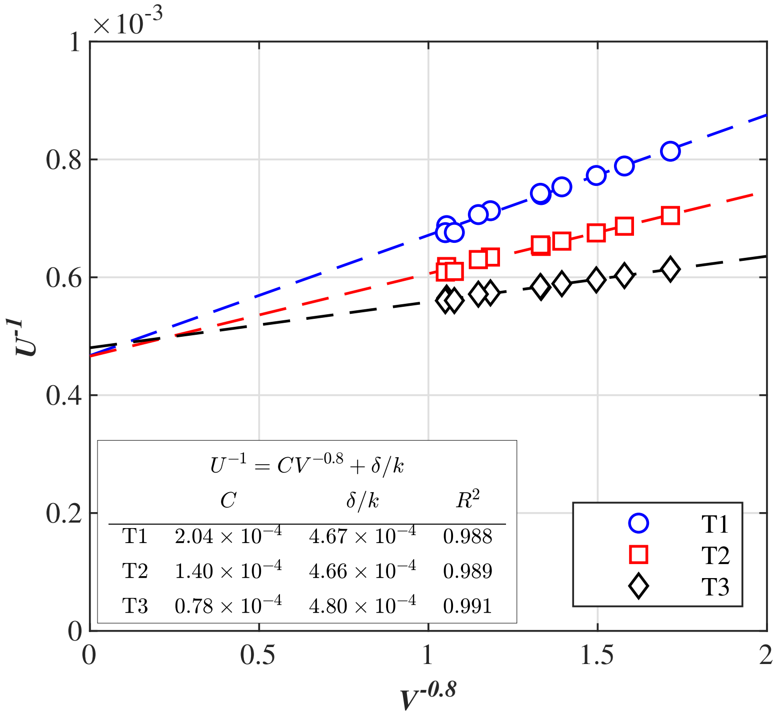

$U^{-1} = CV^{-0.8} + \delta/k$

	C	δ/k	R^2
T1	2.04×10^{-4}	4.67×10^{-4}	0.988
T2	1.40×10^{-4}	4.66×10^{-4}	0.989
T3	0.78×10^{-4}	4.80×10^{-4}	0.991

Figure 2.3: *Wilson plot for calculation of δ/k for the three thermocouples*

As $\mathbf{Re} \propto V$, changing flow rates with constant heat flux varies heat transfer coefficient. Then combining all other controlled parameter as a constant C, the overall heat transfer coefficient can be represented as:

$$\frac{1}{U} = \frac{C}{V^{0.8}} + \frac{\delta}{k} \tag{2.4}$$

Both U and V can be determined experimentally and plotting $1/U$ as a function of $V^{-0.8}$ will lead to a straight line with slope C and intercept as δ/k, as given by Equation 2.4. For the calculation of the overall heat transfer coefficient, U in Equation 2.4, the local fluid temperature T_{lz}, at the thermocouple elevation z_{TC}, was calculated by performing an energy balance between the inlet and the axial location of the thermocouple as follows:

$$T_{l,z} = \frac{\pi d q''}{m_l C_p} z_{TC} + T_{l,i} \tag{2.5}$$

where m_l is the mass flow rate and $T_{l,i}$ is the fluid temperature at the inlet of the test section. The value for U at any thermocouple location can be then estimated using

$$U_z = \frac{q''}{T_{TC} - T_{l,z}} \tag{2.6}$$

Figure 2.3 shows the Wilson plot for the three thermocouples along with the linear regression parameters. Through the regression, the intercept or the δ/k for the three thermocouples was found to be 4.67×10^{-4}, 4.66×10^{-4} and 4.80×10^{-4} for thermocouple T1, T2 and T3 respectively.

The wall temperature, T_w was then calculated from the temperature reported by the thermocouples by using the relation:

$$T_w = T_{TC} - q''\frac{\delta}{k} \tag{2.7}$$

2.3.3 Bubble characterization through high speed image processing

A Photron Fastcam high speed camera was used to perform visualization of the bubble nucleation on the heater surface. The heater test section was backlit with a Fiber Optic Illuminator. To convert the pixels to mm, and to account for the distortions due to the curved nature of the glass section, a calibration scale was developed by placing a grid with known spacing at the center of the test section, as shown in Figure 2.4. This calibration gave the conversion from pixels to mm. In this configuration, the conversion factor near the region of interrogation was about 31 μm/pixel.

Bubble departure diameter

The Matlab image processing toolbox was used to analyze the high speed videos to get bubble departure diameter statistics. The high speed video was split into individual frames or images and each image was individually analyzed. After removing the noise through a 2D Gaussian filter and binarizing the image, the boundary was identified and various objects in the image were marked along with their areas, perimeters and centroids. A circular metric

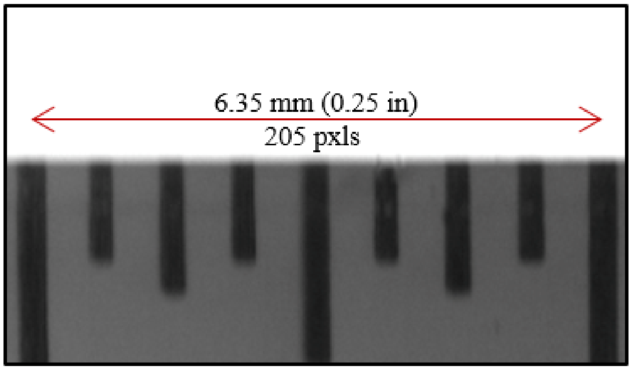

Figure 2.4: *Calibration scale for bubble size determination (Conversion of pixels to mm or inches)*

was defined given by

$$m = \frac{4\pi \times Area}{Perimeter^2} \tag{2.8}$$

where $m = 1$ is associated with a perfect circle. Any objects that lie within a range of $m = 0.7$ to $m = 1$ were classified as individual bubbles. The detected bubbles were tracked between frames using the centroid tracking method[48].

Once the coordinates of the centroid of a bubble were found, the euclidean distance was calculated between the centroid of that bubble and the closest bubble in the next frame. If the euclidean distance was less than 1.25 times the diameter of the detected bubble, the given bubble was identified in the subsequent frame. To identify departure of the bubble from the surface, any bubble that is 0.6 diameters away from the surface was classified as a departure bubble. This was done to distinguish between bubbles sliding on the surface and bubbles departing from the surface.

A total of 1500 frames were analyzed in each high speed video and around 100 departing bubbles per video were measured to get the bubble departure diameter statistics. The algorithm doesn't capture the bubbles that are in front of each other in the viewing window due to the bubbles being out of plane and close to each other. A wide range of bubble departure diameters ranging from 0.1 to 2.5 mm were obtained, which will be discussed in the later section.

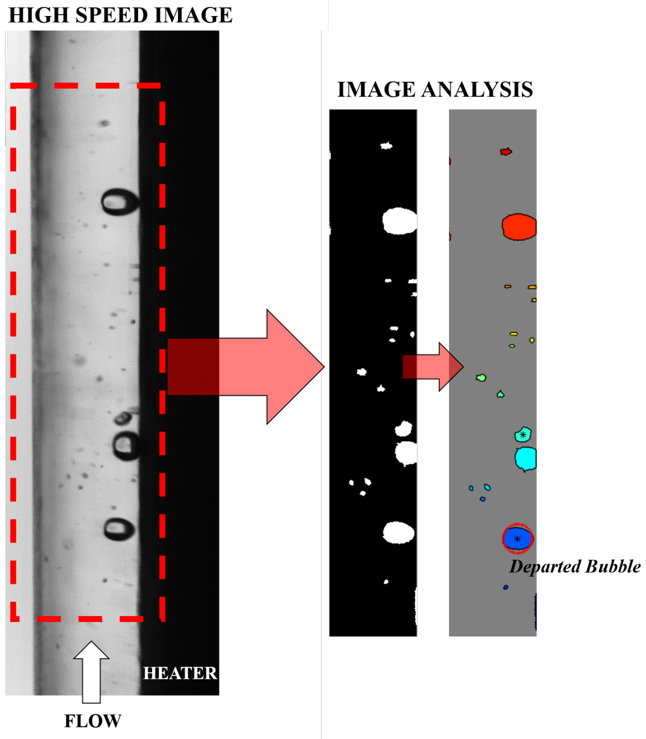

Figure 2.5: *Bubble detection Matlab algorithm*

Number of departing bubbles

The number of bubbles departing the surface per unit area per unit time was estimated by manually counting the bubbles leaving the surface in the view window near thermocouple 2 at $z = 0.28$ m. The automated Matlab algorithm described earlier does not capture all the individual bubbles, so using the algorithm to count the number of departing bubbles gives an inaccurate estimate. Therefore, individual bubbles were manually counted to get a higher accuracy estimate of the evaporative flux, which is a function of the number of bubbles leaving the surface, and the bubble diameter, as will be described in the later sections.

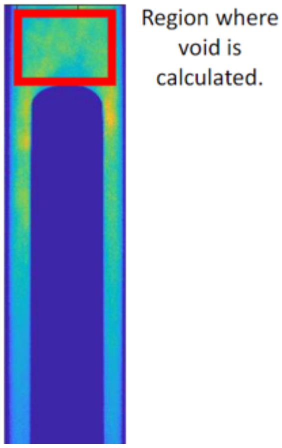

Figure 2.6: *Region above the heater where the void fraction is averaged.*

2.3.4 X-ray radiography setup and methodology for Void fraction quantification

In a two phase flow, X-rays have a higher transmission intensity in vapor as compared to liquid. This phenomena can be exploited to calculate the cross sectional vapor fraction in two phase flow.

The X-ray generator used in the experiments is capable of producing an output power of 2.8 kW and has a current range of 0.4–100 mA and an energy range of 40–120 kV. For the experiments in this study, the following setting was utilized: 20 mA and 40 kV. The generator was positioned at an elevation to view the top portions of the annular test section and the beginning of the riser section. This region is highlighted in Figure 2.6.

To image the transmitted beam through the test section, a high-speed neutron or X-ray imaging camera (XRD 0822 AO/AP) with a Gadox scintillator was used. Some of the features of the neutron or X-ray imaging camera are: real time imaging; 1 megapixel; 0.2 mm pixel pitch; 64,000 gray levels; compatible with X-rays from 20 KeV to 15 MeV; up to 100 frames per second.

The attenuation of X-rays through materials follows the Beer–Lambert law, as shown by[49]:

$$\frac{I}{I_0} = e^{-\mu_f t} \tag{2.9}$$

Since the detector pixel value is directly proportional to the X-ray fluence incident on the detector, the pixel value is given by the equation:

$$P_f = Ce^{-\mu_f t} \tag{2.10}$$

The subscript f denotes a particular experimental test run. Similarly, for air (same as void region) and water filled reference cases, the pixel relationships are $P_a = Ce^{-\mu_a t}$ and $P_w = Ce^{-\mu_w t}$, respectively. The attenuation coefficient for fluid comprising two phases (vapor and water), can be assumed to be linearly related to the water or void fraction and is expressed by:

$$\mu_f = \alpha\mu_a + (1-\alpha)\mu_w \tag{2.11}$$

Taking the log-transform of the pixel-values, P_i, and algebraic manipulation, we get:

$$\alpha = \frac{\log(P_f) - \log(P_w)}{\log(P_a) - \log(P_w)} \tag{2.12}$$

This measure gives the fraction of the X-ray path length occupied by the vapor. Two reference images, at 0% void fraction (completely filled with water) and 100 %void fraction (completely filled with air) are taken before each experimental run. These reference images are then used to calculate the void fraction from the image of the two phase flow.

2.3.5 Experimental procedure

To begin a test, the system was primed with the coolant, the pump was turned on and the heating/cooling load through the heat exchanger was adjusted to get a high temperature of the seawater at the inlet to the test section. Once the inlet temperature was close to the desired or target value, the flowrate was gradually turned down to the desired flowrate and the heater was turned on. The heat flux was increased gradually over the course of 15 minutes to keep the system pressure stable. The system pressure was continuously adjusted during the heat up process until the desired level was reached. The system took about 30 minutes to reach a steady state during which the flowrate, inlet subcooling, system pressure and the heat flux were within the tolerance limit specified. Once the system reached a steady state, the acquisition process was turned on and the heater wall temperature measurements were recorded over the course of the next several hours with the data being recorded at 3 second intervals.

After each seawater test, the system was rinsed with tapwater to clear off the seawater deposits throughout the system followed by a rinse with acetone. The heater surface was also wiped down with an acetone wipe to remove any scale buildup on the heater surface. Once all the major scales were removed from the surface, the system was rinsed multiple times with pure water until the system electrical conductivity reached a steady value of 0.5 mS/cm, which is the electrical conductivity of the water supply. Before conducting a test with seawater, a test with pure water was conducted to verify that the boiling characteristics of the heater surface have not changed between the various seawater tests.

2.4 Results and Discussion

This section presents the results from the experiments conducted during flow boiling with seawater in the annular test section. The heat transfer coefficient measurements in the heated section are presented with comparisons drawn between pure water and seawater. Various wall nucleation parameters are presented to quantify the evaporative flux from the heater surface. Above the heated section, the fraction of area occupied by the vapor phase, or void fraction, is presented at varying heat fluxes. Results from this experimental study provide insights into the seawater cooling behavior in a simplified geometry to help quantify various heat transfer parameters.

2.4.1 Effect of dissolved salts on heat transfer coefficient

A test matrix with different test variables is listed in Table 2.3. Three tests were performed at seawater concentration of 35 kg/m^3. The flow conditions were selected such that the local fluid temperature at thermocouple elevation $z = 0.28$ m and $z = 0.42$ m were the same for all the tests. For each test, the local fluid temperature at each mentioned elevation or thermocouple location was calculated by using Equation 2.13. Each test was performed three times both with seawater and purewater to verify the repeatability of the experiments.

$$T_{l,z} = \frac{\pi d q''}{m_l C_p} z_{TC} + T_{l,i} \tag{2.13}$$

The variation of wall temperature with time for the three axial locations for both pure water and seawater is shown in Figure 2.7. The saturation temperature at the inlet of the test

Table 2.3: *Flow conditions and calculated bulk liquid temperature (T_l) at the three axial locations using Equation 2.5.*

	m_l (kg/s)	$T_{l,i}$ (K)	Q (W)	P_i (Pa)	Salinity (kg/m^3)	T_l(K) $z = 0.42$ m	T_l(K) $z = 0.28$ m	T_l(K) $z = 0.14$ m
Test 1	0.010	353	1800	1.24×10^5	35	379	373	363
Test 2	0.010	346	2200	1.24×10^5	35	379	373	359
Test 3	0.010	343	2600	1.24×10^5	35	379	373	358

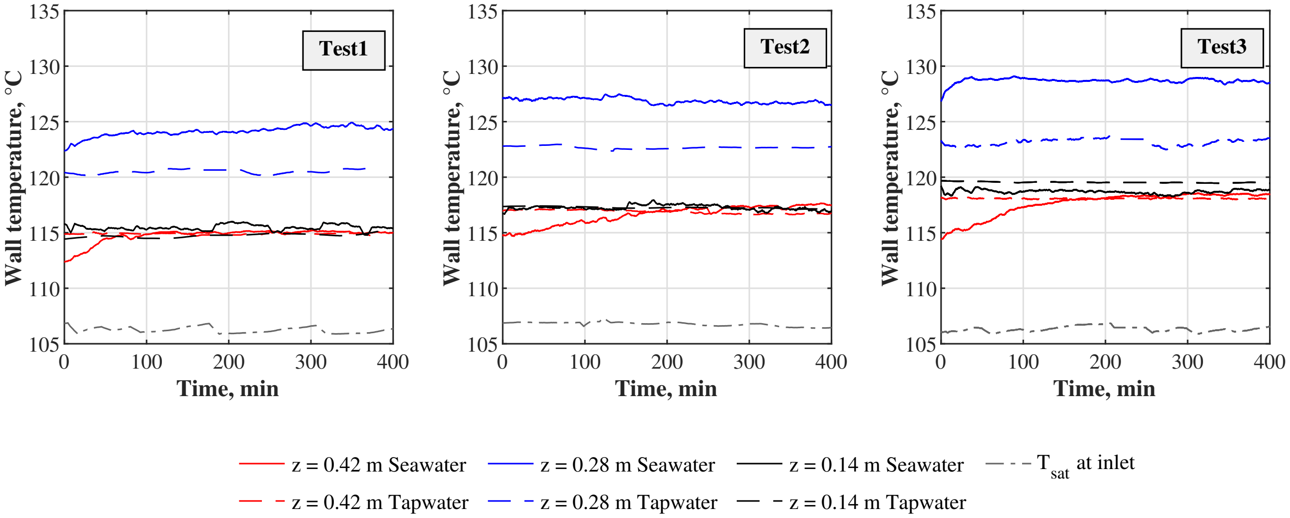

Figure 2.7: *Comparison of the temporal evolution of the wall temperatures in the saturated boiling ($z = 0.42$ m) and subcooled boiling ($z = 0.28$ m) region*

section is also shown in the figure for reference. The heat transfer coefficient that corresponds to the wall temperature measurement is shown in Figure 2.8. The wall temperature and the heat transfer coefficient did not change with time for pure water in all the three tests for the three axial locations. This is expected as the tapwater used has negligible impurities and thus, no deposition or fouling was observed within the time frame of the experiment.

The steady state values of the measured heat transfer coefficient for pure water were compared to the expected value using the Gungor & Winterton correlation[2] and the Shah correlation[3;4] for flow boiling with water in a vertical annulus. The correlations are mentioned in Table 2.4. For the calculation of the single phase heat transfer coefficient term in the Shah correlation, the single phase mixed convection flow correlation by El-Genk et al.[50] was used. The comparison between predicted and experimentally measured heat transfer coefficient values is shown in Figure 2.9. A mean absolute deviation of 10 % and 15 % between the measurement and prediction was found for Gungor & Winterton and Shah correlation respectively. This shows that flow boiling heat transfer conditions produced in the facility for pure water were comparable to previous reports.

When seawater was used as the coolant, at t = 0 min, the wall temperature for $z = 0.42$ m, which is under saturated boiling, was lower than pure water for all the three tests.

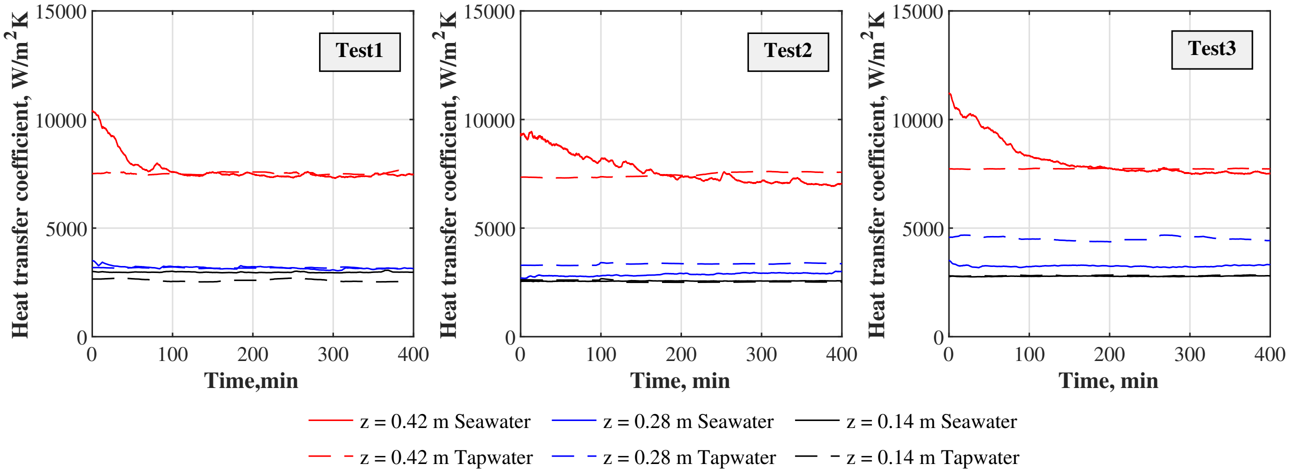

Figure 2.8: *Comparison of the temporal evolution of the heat transfer coefficient in the saturated boiling ($z = 0.42$ m) and subcooled boiling ($z = 0.28$ m) region*

This was reflected in an enhancement of the heat transfer coefficient in the initial phase of the transient as shown in Figure 2.8. After the initial asymptotic drop, the heat transfer coefficient stayed constant at a value similar to that of water. For both $z = 0.28$ m and $z = 0.14$ m, no significant transient evolution is observed in seawater. However, the heat transfer coefficient for seawater at $z = 0.28$ m is lower than pure water for the entire duration of the experiment. The thermocouple T1 at $z = 0.42$ m being under saturated boiling has a higher heat transfer coefficient in the initial transient. This can be attributed to the increase in nucleation activity due to the salt deposits acting as additional nucleation sites. This initial transient of enhanced heat transfer rate is referred to as the induction period. After the induction period, the heat transfer coefficient is reduced due to the formation of the fouling layer by the salt deposits. For thermocouple T2, which is under subcooled boiling at $z = 0.28$ m, no asymptotic stabilization of the heat transfer coefficient was seen for all the tests. It is possible that the induction period occurred before data acquisition process was started while the system was reaching a steady state.

The percentage difference in the asymptotic heat transfer coefficient between seawater and pure water for the three tests is shown in Figure 2.10. The difference at $z = 0.28$ m, which is under subcooled boiling, increased as the heat flux increased. However at a higher elevation at $z = 0.42$ m under saturated boiling, there wasn't a significant reduction in heat

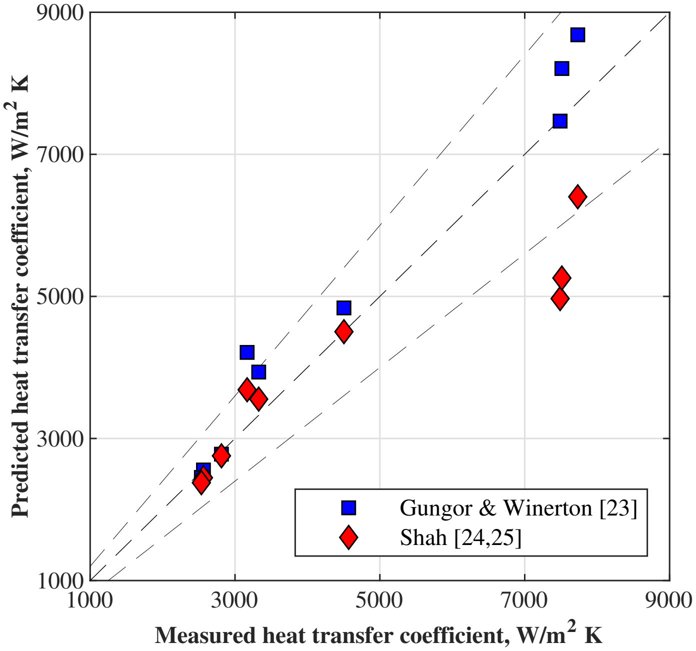

Figure 2.9: *Comparison of measured heat transfer coefficient with Gungor & Winterton*[2] *and Shah correlation*[3;4] *for pure water*

Table 2.4: *Correlations used for comparing the predicted heat transfer coefficient with the measured heat transfer coefficient (GW = Gungor & Winterton)*[2;11].

GW[2]	$q'' = h_{sp,l}(T_w - T_l) + Sh_{nb}(T_w - T_{sat})$ $S = 1/(1 + 1.15 \times 10^{-6} F^2 Re_l^{1.17})$; $F = 1 + 2.4 \times 10^4 Bo^{1.16}$
Shah[3;4]	$q'' = \psi h_{sp,l} \Delta T_{sat}; Bo = q''/Gh_{lv}$ $\psi = \begin{cases} \psi_0 \text{ for low subcooling} \\ \psi_0 + \frac{\Delta T_{sub}}{\Delta T_{sat}} \text{ for high subcooling} \end{cases} ; \psi_0 = \begin{cases} 230 Bo^{0.5} : Bo > 0.3 \times 10^{-4} \\ 1 + 46 Bo^{0.5} \text{:Bo} < 3 \times 10^{-4} \end{cases}$

transfer coefficient.

In the saturated boiling region, due to an increased nucleation activity, there exists a higher mixing between the bubbles and the bulk liquid. This causes the advection effects to promote salt mixing from the heated surface back to the bulk liquid. Therefore, the mass transfer resistance becomes negligible and the heat transfer to the seawater occurs at the same rate as that with no salts due to their similar thermophysical properties. The increased mixing also causes larger shear stresses at the heater surface, thereby increasing the removal rate of the deposit on the heater surface causing fewer deposits to attach on the surface as

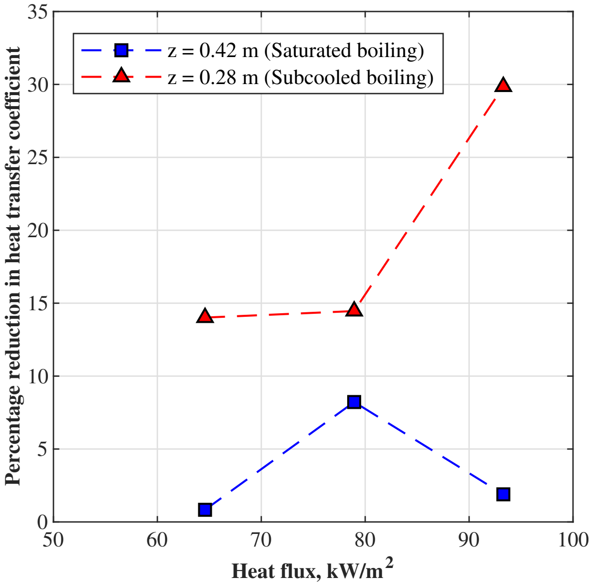

Figure 2.10: *Percentage difference of heat transfer coefficient between seawater and tapwater*

compared to subcooled boiling.

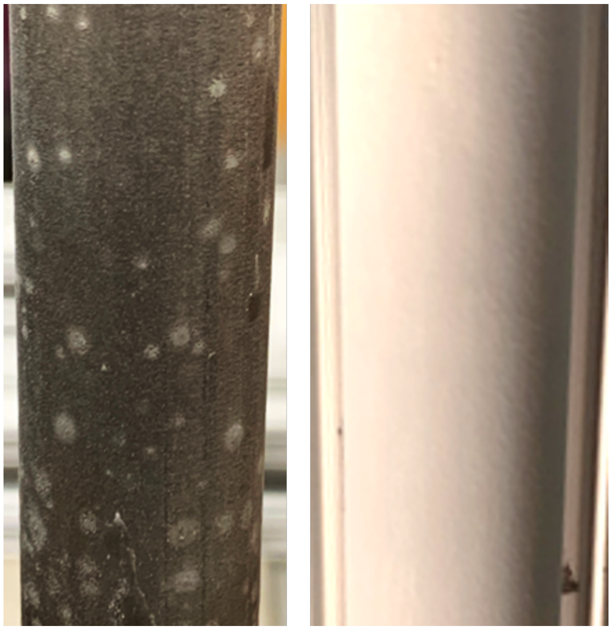

Figure 2.11: *Spotty deposition pattern in subcooled boiling (left) and uniform deposits in saturated boiling (right)*

At the lowest elevation, the heat transfer performance was very similar due to very similar thermophysical properties under single phase flow. Upon inspection of the heater surface after the end of the experiment, no deposits were found near the measurement location at $z = 0.14$ m which was under single phase flow. In the subcooled boiling region at $z = 0.28$ m, hard spotty deposits with high adhesion strength were observed. At the highest location, under saturated boiling at $z = 0.48$ m, soft deposits uniformly spread out across the heater with much lower adhesion strength were observed, as shown in Figure 2.11.

2.4.2 Effect of dissolved salts on bubble characteristics and evaporative flux

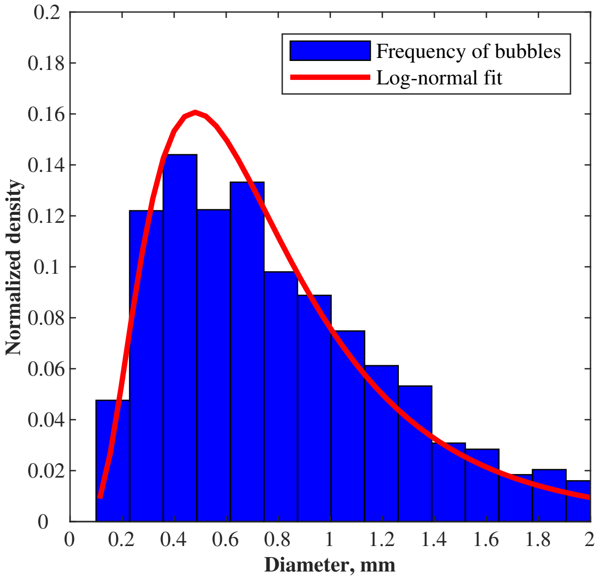

Figure 2.12: *Distribution of bubble departure diameter of seawater for Test 1 with a log-normal fit* ($\mu = 0.66mm, \sigma = 0.62mm$)

Along with the temperature measurements, high speed videos of the boiling phenomena were taken for each test. These videos were analyzed to estimate the departure diameter and the number of nucleating bubbles in the region 2 inches above and below the thermocouple T2 ($z = 0.28$ m) which is in the subcooled boiling region. The presence of isolated bubbles in the subcooled boiling region made identification and quantification of individual bubbles possible. In saturated boiling region, the presence of high bubble nucleation activity made quantification of bubble parameters not feasible. Therefore, only the subcooled boiling region

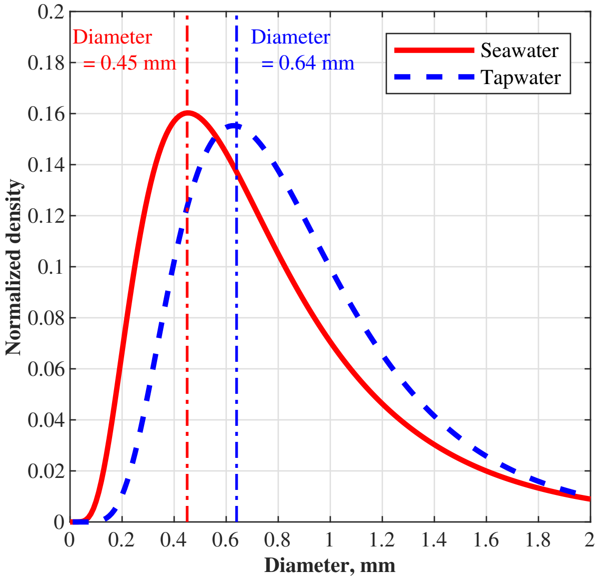

Figure 2.13: *Log-normal distribution of bubble departure diameter of seawater and pure water for Test 1 with the most probable diameters*

was investigated for the bubble characteristics. Each high speed video was recorded at 1500 frames per second for a duration of 1 second. Thus, a total of 1500 frames were analyzed. At least 100 departing bubbles were analyzed in each high speed video. The distribution of bubble departure diameter for Test 1 for both seawater and pure water is shown in Figure 2.13. Both coolants exhibited a positive skewed or a log normal distribution of departure diameter. This distribution of the bubble departure diameter is consistent with the observations of Martinez et al.[51] and Ooi et al.[52] for pure water at low pressures. For assessment of a representative diameter from the range of diameter distribution, the arithmetic mean departure diameter was selected. With both distributions exhibiting a similar range of diameters, the mean departure diameter is smaller in seawater as compared to pure water.

Log-normal probability density function was fit on the bubble departure diameter data presented in Figure 2.12. The bubble departure diameter peak, as shown in Figure 2.13, is reduced from 0.64 mm with tapwater to 0.45 mm with seawater, which is about 30% reduction. The mean departure diameter is smaller for seawater as compared to pure water for all the test cases.

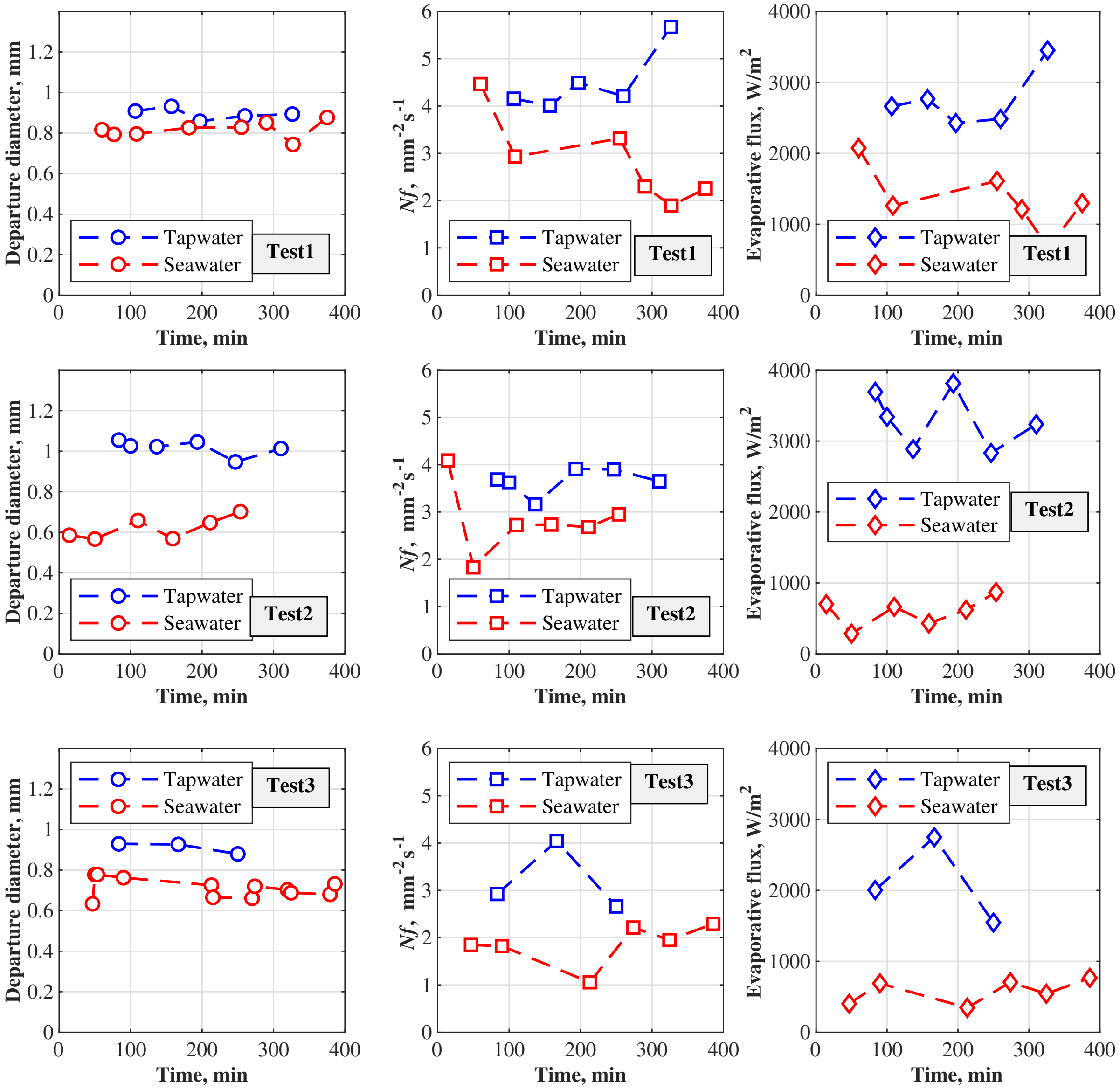

Figure 2.14: *Temporal evolution of bubble departure diameter, Nf, and evaporative flux for the three tests for both tapwater and seawater*

The temporal evolution of the arithmetic mean bubble departure diameter for each test is shown in Figure 2.14. The mean departure diameter did not show significant variation with time and stayed almost constant during the duration of the test. This is consistent with data presented in the Figure 2.7, where the wall temperature stayed constant in the subcooled boiling region. The variation of the mean departure diameter with heat flux for both coolants is shown in Figure 2.15.

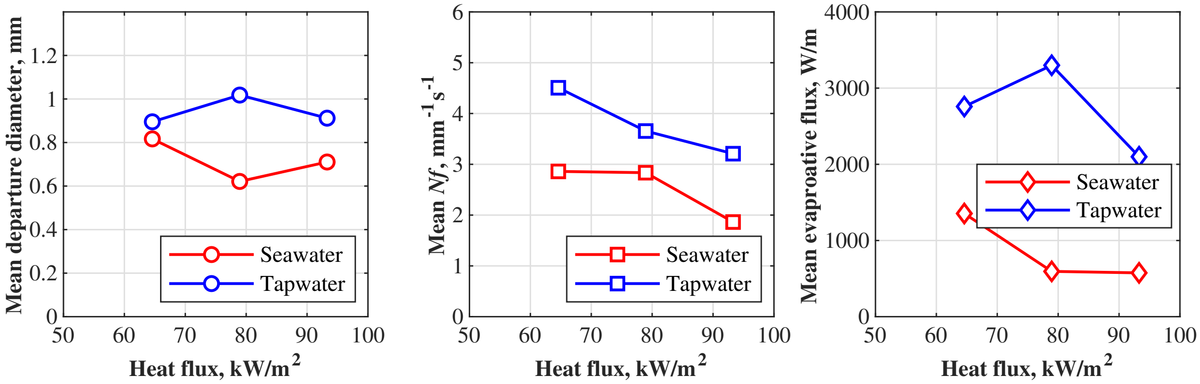

Figure 2.15: *Time averaged comparison of bubble departure diameter, Nf and evaporative flux for different heat fluxes between seawater and pure water*

In an electrolyte solution, the formation of a vapor bubble causes an increase in concentration in the microlayer beneath the bubble compared to the bulk fluid. This increase has been reported to be between 1 and 2.05 times the bulk concentration by Jamialahmadi[30]. This increase in concentration causes the effective boiling point to increase, thereby reducing the wall superheat, which causes the vapor bubble to depart at a smaller diameter with the presence of salts.

The number of departing bubbles in the 1 second interrogation window were counted to estimate the evaporative flux, which is a function of the bubble characteristics given by:

$$q''_E = (Nf)\rho_v h_l v \frac{\pi {D_d}^3}{6} \tag{2.14}$$

where (Nf) is the number of departed bubbles per unit area per second.

The variation of mean Nf with heat flux for pure water and seawater is shown in Figure 2.14. As shown in the figure, pure water had higher number of departing bubbles from a unit area per unit time as compared to seawater for all the tests. The variation of Nf with time is inconclusive, but the general trend is that the mean value is reduced in seawater.

Due to the high concentration of the solute in the microlayer beneath the bubble, the surface tension (σ) of the seawater liquid is increased[53;54] and thus, a higher superheat would be needed to activate a given nucleation site (with cavity radius r_c), as given by the Equation

$$p(T_{sat}) - p = \frac{2\sigma}{r_c} \tag{2.15}$$

Therefore, fewer nucleation sites are expected on the heater surface with seawater as compared to pure water due to the increased surface tension. Due to the increased concentration in the microlayer beneath the bubble, the local saturation temperature increases. This reduces the local superheat causing an increase in the bubble waiting time or reducing the bubble departure frequency f. The reduced bubble departure frequency was also observed by Gu and Jamialahmadi[30;55].

Using the information about Nf and D_d, the evaporative flux was calculated using Equation 2.14. The variation of the evaporative flux with heat flux for both coolants is shown in Figures 2.14 and 2.15. A lower evaporative flux was observed in seawater as compared to pure water. As the evaporative flux, or rate of vapor generation is lower, it implies that a smaller fraction of the heat is taken away due to the phase change process and a larger fraction of the heat transfer occurs due to the convection currents of the single phase liquid. Also, with fewer bubbles being generated on the surface, the boundary layer is also relatively undisturbed. Therefore, one would expect the heat transfer rate to be lower in seawater as compared to pure water. This is consistent with the wall temperature and heat transfer coefficient measurements shown in Figure 2.7 and 2.8.

2.4.3 Effect of dissolved salts on two phase flow

High speed images of the two phase flow beyond the heated region, in the riser, are shown in Figure 2.16 for both pure water and seawater. As evident from the image sequence, the flow pattern in pure water consists of large slugs of bubbles that are formed after coalescence of bubbles. This bubble coalescence is absent in seawater at the vapor generation rates under consideration. The bubbles retain their structure even when two bubbles are in close contact with each other. A thin liquid film is present between the bubbles that contains the ionic charges that have accumulated on the liquid-vapor interface, which causes repulsive forces and inhibits bubble coalescence. The presence of frothy/bubbly flow is a stable flow due to consistent vapor structure, unlike pure water, where the bubble coalescence leads to a two phase flow pattern containing large vapor slugs and large regions with no vapor.

To quantify the vapor fraction, X-ray imaging was utilized to estimate the void fraction of the two phase flow in the riser section. The X-ray radiographs of the flow are shown in Figure 2.17. For comparison purpose, the void fraction is averaged in the area above the heater as shown in Figure 2.6. As discussed earlier, pure water exhibits a non-homogeneous vapor distribution, where as seawater shows a stable homogeneous vapor distribution as shown in Figure 2.17.

The comparison between seawater and pure water cases show that as the power level increases, the void fractions observed in pure water increases, whereas the effect was the complete opposite in the case of seawater. It is also evident that under all scenarios, pure water shows lower void fraction levels compared to seawater. For all three test cases, i.e., at three different power levels, seawater had a significantly higher void fraction (Figures 2.17 and 2.18). This gap became smaller at higher power levels.

As discussed in the previous section, the presence of salts in the liquid inhibits bubble coalescence along with reducing the bubble diameter in the two phase flow. Smaller bubbles

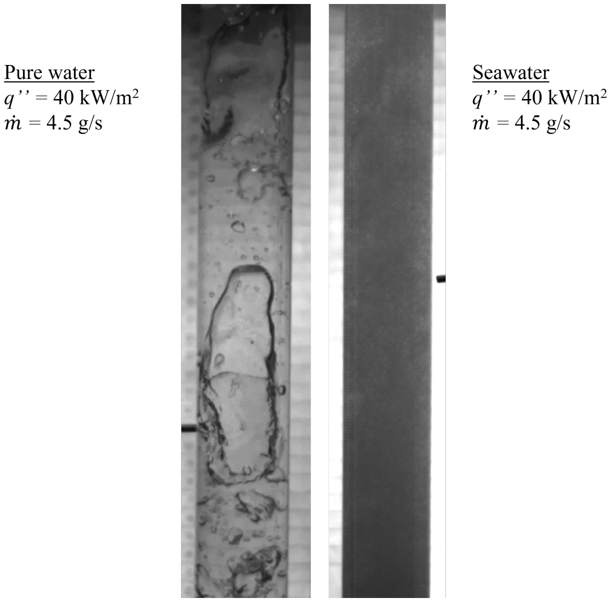

Figure 2.16: *Two phase flow pattern in pure water and seawater. Seawater exhibits bubbly flow and no slugs due to the lack of bubble coalescence*

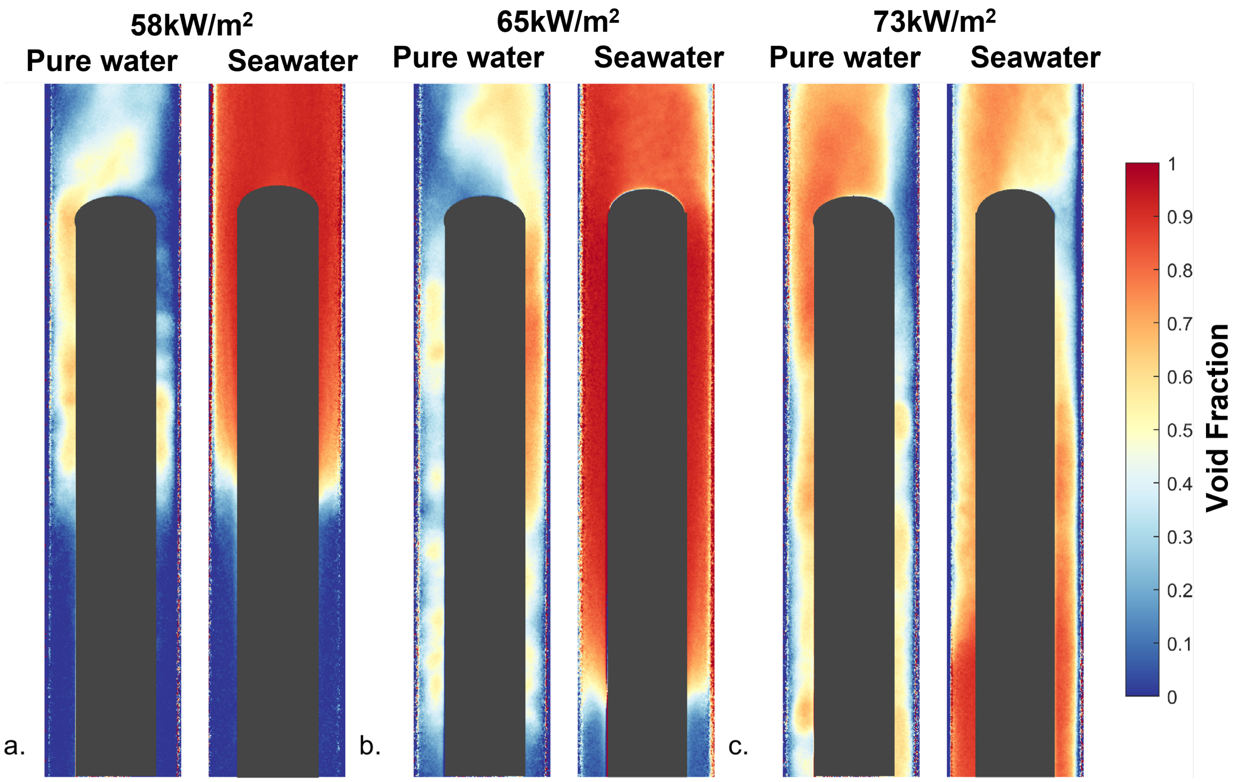

Figure 2.17: *Comparison of void fraction of pure water (left) and seawater (right) at initial steady state conditions for different power levels.* (***a***)*58kW/m*^{2}*.* (***b***) *65kW/m*^{2}*.* (***c***)*73kW/m*^{2}*.*

do not experience the same buoyancy force to drag ratio as larger bubbles and therefore move slower in the liquid relative to larger bubbles. This causes a reduction in slip ratio and can create a separated flow in which the liquid may be moving faster than the bubbles. This can create high bubble population hold up and increase void fraction locally. As the heat input increases and correspondingly the vapor generation rate increases, the high vapor generation rate causes increasing number of bubbles to coalesce and form slugs. These larger slugs experience less drag and have higher relative velocity as compared to smaller bubbles. Thus, the measured void fraction in seawater approaches the void fraction of pure water as the heat input is increased.

2.4.4 Effect of dissolved salts on pressure drop

Given the distinct void fraction characteristics between pure water and seawater, it is expected that the pressure drop would then be influenced. Dissolved salts change the fluid

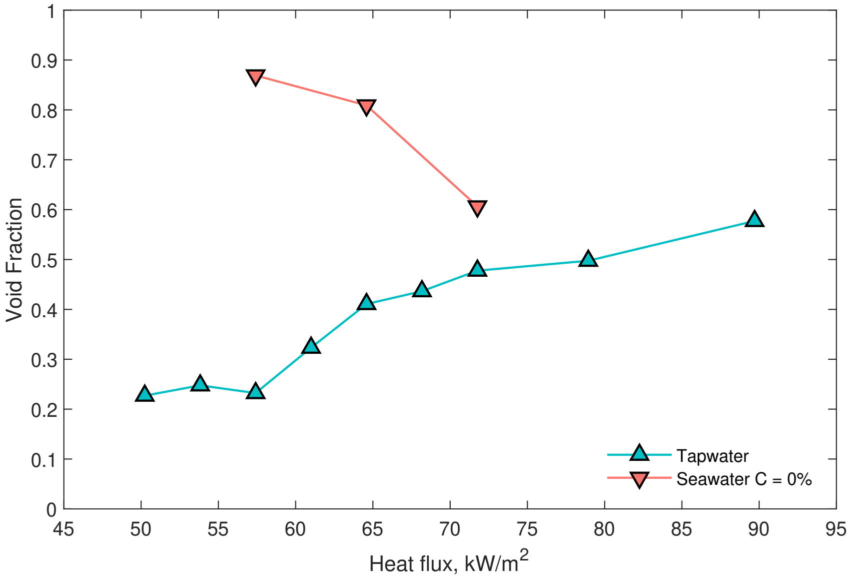

Figure 2.18: *Seawater and pure water void fraction comparisons at different power levels.*

properties in a minor way but affect flow conditions considerably, which makes using conventional pressure drop models possibly unreliable.

In the homogeneous flow model, the total pressure drop over a specific length is a sum of the contributions of the static head, momentum head and the frictional head. The change in static pressure describes the pressure change due to elevation or height differences between the locations being measured. The momentum or acceleration pressure drop takes into consideration the acceleration of the vapor needed to conserve the conservation of mass. Lastly, the frictional pressure drop is used to determine the pressure drop due to friction between the phases and the channel wall. The total pressure gradient can then be calculated by taking the sum of each component of the pressure gradient as:

$$\left(\frac{dp}{dz}\right)_{total} = \left(\frac{dp}{dz}\right)_{static} + \left(\frac{dp}{dz}\right)_{momentum} + \left(\frac{dp}{dz}\right)_{friction} \tag{2.16}$$

The static pressure gradient is calculated using the void fraction α as:

$$\left(\frac{dp}{dz}\right)_{static} = \rho_H g \tag{2.17}$$

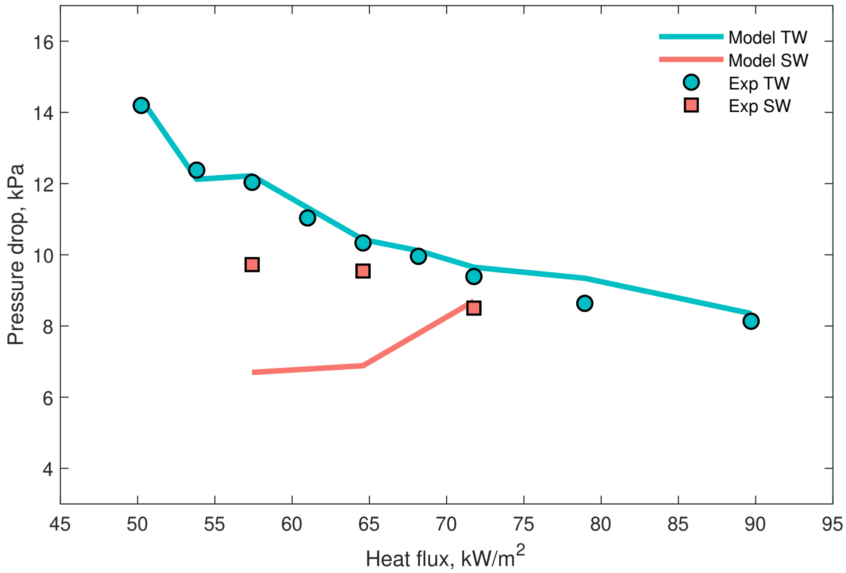

Figure 2.19: *Comparison of total pressure drop with experimental measurements for pure water and sea water.*

where ρ_H is the homogeneous density and g is the acceleration due to gravity. The homogeneous density can be calculated using:

$$\rho_H = \rho_l \left(1 - \alpha_{exp}\right) + \rho_g \alpha_{exp} \tag{2.18}$$

where α_{exp} is the experimentally measured void fraction. The momentum pressure gradient along the channel length for the total mass flux G is given by:

$$\left(\frac{dp}{dz}\right)_{momentum} = \frac{d(G^2/\rho_H)}{dz} \tag{2.19}$$

The frictional pressure gradient is found through the following equation:

$$\left(\frac{dp}{dz}\right)_{friction} = \frac{2 f_{tp} G^2}{\rho_H D_h} \tag{2.20}$$

wheref_{tp} is the two-phase friction factor and D_h is the hydraulic diameter. Here, the Blasius equation was used for f_{tp}, which is given by:

$$f_{tp} = 0.079\left(\frac{GD_h}{\bar{\mu}}\right)^{-0.25} \tag{2.21}$$

where μ_{tp} is the two-phase dynamic viscosity, which is a mass-averaged viscosity given by:

$$\mu_{tp} = x\mu_g + (1-x)\mu_{tp} \tag{2.22}$$

For the calculations presented here, the experimentally measured void fraction was used in calculating the total pressure drop across the two phase channel. Here it was assumed that there exists a linear variation of thermodynamic vapor quality between the calculated onset of nucleate boiling (ONB) point and the end of the heated section. The flow was assumed to be completely single phase in the region below the ONB point. The results of the total pressure drop obtained from the model described above with the experimentally measured total pressure drop are shown in Figure 2.19. Pure water shows that the pressure drop from the homogeneous model is a very good match with the experimental observations, even at higher power levels. However, in the case of seawater, a discrepancy is observed between experimental observations and the predictions of the model. This highlights the use of traditional two phase pressure drop models as inaccurate, especially when large amounts of bubble accumulation is expected. The discrepancy between the measurement and model can be addressed by modeling the frictional resistance of the two phase flow through proper modeling of the interfacial area. Because of the large amount of bubble accumulation, a large interfacial area exists between the liquid and vapor phase and this can have a significant impact on the frictional characteristics.

2.4.5 Discussion

The results of the experimental study reported in this section focus on the heat transfer performance of seawater in an annulus. Seawater reported lower heat transfer coefficient as compared to pure water. This reduced heat transfer coefficient is decoupled from the fouling effect as no significant salt build up was observed on the heat transfer surface in the subcooled boiling region. This reduced heat transfer coefficient was attributed to a lower evaporative flux as evident from the smaller departure diameter and low bubble departure frequency. Since the single phase heat transfer component of seawater is similar to pure water, the reduced heat transfer coefficient can be isolated to the boiling characteristics. The high concentration of the dissolved salts in the microlayer underneath the bubble is a complex phenomena to model due to the varying diffusivities of several ionic components and their interaction with each, thereby providing avenue to investigate the interaction of various ions and their diffusion coefficients in water. The heat transfer data obtained from this study can be utilized to validate the mixed salt effects models in the future to gain an accurate understanding of the kinetics of salt dissolution and precipitation. This study suggests that in a nuclear accident, seawater can be a viable coolant as the heat transfer deterioration is not significant and the effect of salt precipitation is negligible in the time scales of few hours, which is representative of the time scale in a nuclear accident. Further research on the longterm effect involving several days can perhaps provide insights into the longterm precipitation, if any.

The presence of salts although increases the local void fraction, it also increases the interfacial frictional resistance of two phase flow. The effect of liquid-vapor interfacial area on the total pressure drop should be investigated further in future studies.

2.5 Conclusions

This section reported the findings of the experimental study conducted with seawater on a vertical annulus. Hydrodynamic insights obtained from the two phase flow behavior suggest the formation of a stable dominant bubbly flow with seawater. This bubbly flow caused due to the inhibition of bubble coalescence increases the interfacial frictional resistance of the two phase flow, which was evident from the pressure drop calculations from the void fraction measurements. Flow boiling tests for heat transfer assessment indicated reduced heat transfer coefficient in seawater as compared to pure water, especially in the subcooled boiling region. With a high evaporative flux in the saturated boiling region, the disturbance of the boundary layer by the bubble induced turbulence causes heat transfer characteristics similar to that of pure water.

Chapter 3

Experimental approach to investigate Debris Bed coolability

3.1 Introduction

In a postulated severe accident scenario, a lack of sufficient heat removal from the reactor core due to failure of normal and emergency cooling systems results in tremendous heating of the core and causes a meltdown of the fuel rods. A melt pool is formed within the reactor core comprising the fuel and support structure materials, usually referred to as *corium*. Corium relocates to the residual water pool in the Reactor Pressure Vessel (RPV) due to gravitational action and during its descent through this water pool, the molten material undergoes hydrodynamic interactions with liquid water and disintegrates into small granular fragments. This Molten Fuel-Coolant Interaction (MCI) leads to the formation of a granular porous structure called as a debris bed. This phase of the accident is referred to as the *in-vessel* phase of the accident, where the debris bed is contained within the RPV.

The debris bed has a specific power between 100 W/kg and 300 W/kg, which is equivalent to power density between 0.5 MW/m^3 and 50 MW/m^3. Such high amount of heat generation should be constantly cooled to contain the accident. This is possible through sustained cooling via boiling heat transfer within the pores of the debris bed. Insufficient cooling can lead to remelting of the debris bed causing the molten mass to accumulate in the lower

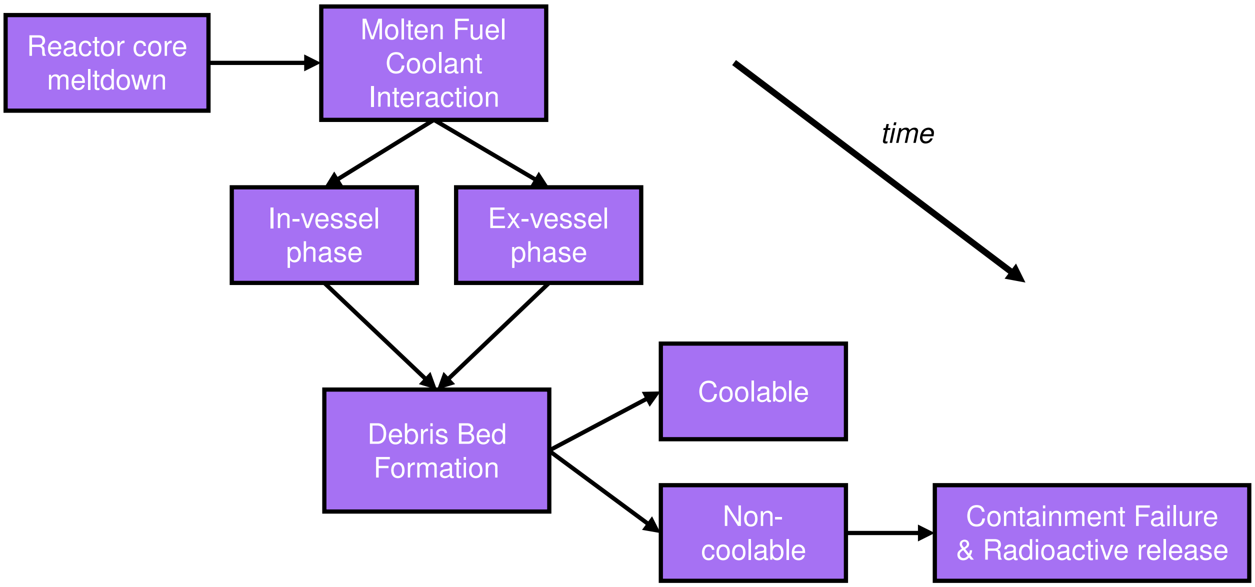

Figure 3.1: *Schematic of accident progression during formation of a debris bed.*

region of the RPV. The molten mass interacts with the RPV wall, and in extreme situations, can lead to failure of the RPV wall causing the molten mass to relocate outside the reactor containment. This phase of the accident is referred to as the *ex-vessel* phase of the accident. The accident progression is illustrated in Figure 3.1.

It is therefore extremely important to successfully remove the decay heat generated in the debris bed to contain the accident and stop its progression. A stable and coolable condition can be achieved only if the evaporated liquid in the bed is continuously replaced by additional cooling water percolation into the debris bed from the overlying pool. This complete wetting of the debris bed is absent when the heat flux is higher than the critical dryout heat flux, beyond which, the bed is rendered uncoolable. Thus, the dryout process imposes a critical cooling limit on a debris bed, and gaining an understanding of this limiting process is critical for designing various reactor safety systems.

The dryout heat flux has been studied under several conditions with pure water, both numerically and experimentally. Numerical codes like MELCOR[56], WABE[57], MEWA[58] were developed to study the dryout heat flux in multidimensional settings. Recent experimental facilities including STYX[43], DEBRIS[59], POMECO[60] and SILFIDE[61] were build to

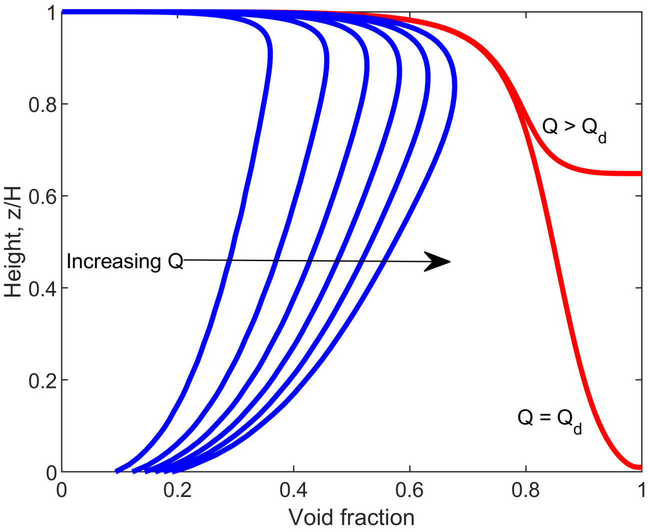

Figure 3.2: *Evolution of the calculated steady state void fraction using mass, momentum and energy conservation using Lipinski model for two phase permeability. For* $Q < Q_d$*,the void fraction increases with power.*

characterize the dryout heat flux of debris beds. Calculations involving solving the mass, momentum and energy equation in a heat generating packed bed show that the void fraction in the bed increases as the heat flux is increased. For heat fluxes beyond the critical dryout heat flux, the void fraction reaches unity at a particular elevation and no liquid percolation exists below this elevation. This is illustrated in Figure 3.2 where the Lipinski model was utilized to model the two phase frictional characteristics. Further details on modeling are shown in Section 4.4.1.

Experimentally measuring the dryout involves measurements of either local temperature in the bed and/or the pressure gradients and/or the local void fractions. These experimental facilities measured the dryout using temperature and pressure measurements[43;59–61]. Measurement of the void fraction in the bed has not been widely utilized to measure dryout because of the complexities of the measurement process. The experimental work stated above showed the dependence of the dryout heat flux on various system parameters including pressure, subcooling, particle size etc. These studies concluded that the major factor contributing to the dryout heat flux is the pressure drop characteristics. Reducing the particle diameter of the packed bed increases the frictional resistance, which therefore reduces the dryout heat flux. Similarly, experiments with non-spherical particles, particles with irregular surfaces, particles of mixed diameters have also shown that increasing the frictional pressure drop reduces the dryout heat flux[60;62]. However, there is still uncertainty in the measurement of the dryout heat flux, and different experimental facilities show slightly different dryout heat flux. One of the reasons for this uncertainty is the spatial resolution of temperature measurement. Low spatial resolution leads to over prediction of the dryout heat flux[43]. Various experimental setups in literature use discrete thermocouples to measure a spike in temperature to indicate dryout. A comparison of the resolution of various experimental setups is shown in Table 3.1.

Therefore, the changes in the bubble behaviors, pressure drop characteristics, and heat transfer characteristics with the addition of salts in water can have an impact on the short term cooling behavior of a debris bed with seawater, especially the dryout heat flux. The fouling or the deposition mechanism of salts over time can cause the geometric and thermal

Table 3.1: *Comparison of spatial and temporal resolution of temperature measurement in experimental setups found in literature compared to current study.*

Experiment	Source of heating	Spatial resolution	Temporal resolution
Hofmann[42]	Induction heating	40 mm	Thermocouple
Hu[41]	Resistance heater	20 mm	Thermocouple : 4 seconds
Lindolhm[43]	Resistance heater	42 mm	Thermocouple
Schafer[38]	Resistance heater	100 mm	Thermocouple
Li[60]	Induction heating	38 mm	Thermocouple
Atkhen[63]	Induction heating	50 mm	Thermocouple
Current study	**Induction heating**	**2.5 mm**	**SWI-DTS: 250 Hz**

characteristics of the porous medium to change over time. This deposition of salts on the heat transfer surface can degrade the heat transfer over time and can lead to the plugging of pores, leading to additional complexities in the cooling of debris beds.

3.2 Objectives

The objectives of this study are to investigate the cooling performance debris beds and to compare the performance of pure water and seawater. The two mechanisms- dryout and fouling are experimentally measured. The influence of the addition of salts in pure water on the dryout heat flux is investigated for short term cooling. For longterm cooling, for heat fluxes lower than the dryout heat flux, the degradation of heat transfer over time due to fouling is also investigated.

A high spatial resolution temperature sensor is deployed in the system that measures temperatures on the principles of Rayleigh backscattering. This temperature sensor gives a high resolution thermal response of the test section under various cooling scenarios. To measure the liquid-vapor behavior within a debris bed, a non intrusive neutron imaging technique developed using the KSU Triga nuclear reactor is utilized to capture the void fraction in the test section.

3.3 Characteristics of a debris bed

The composition and structure of a debris bed is dependent on a number of factors during an accident progression such as size of the core breach, mass flux of the molten corium, temperature of molten corium during the breach, temperature and pressure of water pool, etc. Various Fuel-Coolant-Interaction (FCI) experiments have been performed in literature to characterize the kind of debris bed formed in an accident scenario. Observations from these experiments reveal that the debris formed has an irregular and non-homogeneous porous composition with a significant uncertainty in bed porosity and size of the particles. The wide range of particle diameters, ranging from 0.2 mm to 10 mm, with porosity ranging from 0.25 and 0.7 were observed. These are summarized in Table 3.2.

Table 3.2: *Porous media characteristics of debris bed formed in FCI experiments.*

Experimental program	Particle size range (mm)	Porosity
CCM[64]	0.8 - 5	0.5-0.7
KROTOS[65]	0.1 - 2	N/A
FARO[66]	0.25 - 11	0.4-0.6
TROI[67]	<6	N/A
DEFOR[68]	2-10	0.45-0.7

3.4 Design of experimental debris bed test section

Because of the non-homogenities involved in the real scale debris bed, various assumptions need to be made about these parameters that simplify the modeling. One of the methods to simplify a complex porous debris bed is to use the concept of an *effective diameter*, where a debris bed consisting of a mixture of particle sizes can be represented by a bed of single-sized particles having an effective diameter. Effective diameter was introduced by Chikhi[40] to represent complex debris beds by a single sized mono-dispersed debris bed. This effective diameter is the diameter of spheres of a mono-dispersed debris bed that would have the same frictional pressure drop as that of a complex polydispersed debris bed. The study by Chikhi[40] has shown that an effective diameter is a suitable approximation of a polydispersed bed when the dryout or quenching characteristics of a debris bed are to be studied. Therefore, the concept of an effective diameter was applied to the test section design.

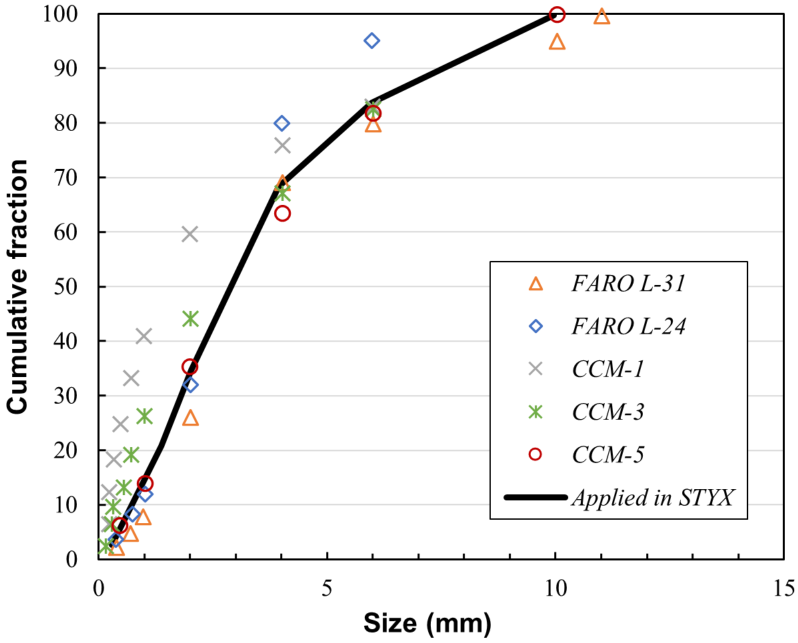

Figure 3.3: *Particle size distribution of various FCI tests and the packed bed deployed in STYX.*

As mentioned in the previous section, there exists a large uncertainties in the particle size distribution data acquired from FCI experiments. For a given particle size distribution, analytical models exist that would predict the pressure drop characteristics as a function of particle size distribution. However, the use of experimental pressure drop data has more value than using models. For this reason, the experimental data from the STYX experimental facility was used for pressure drop assessment in this study. The particle size distribution of the STYX bed, as compared to various FCI experiments is shown in Figure 3.3. As shown in the figure, the STYX particle size distribution follows the distribution of various FCI experiments.

The experimental pressure drop data of the STYX bed is shown in Figure 3.4. As shown in the figure, the pressure drop increases with the superficial velocity of the liquid phase. Here, the superficial velocity is the volumetric flowrate of the fluid divided by the total

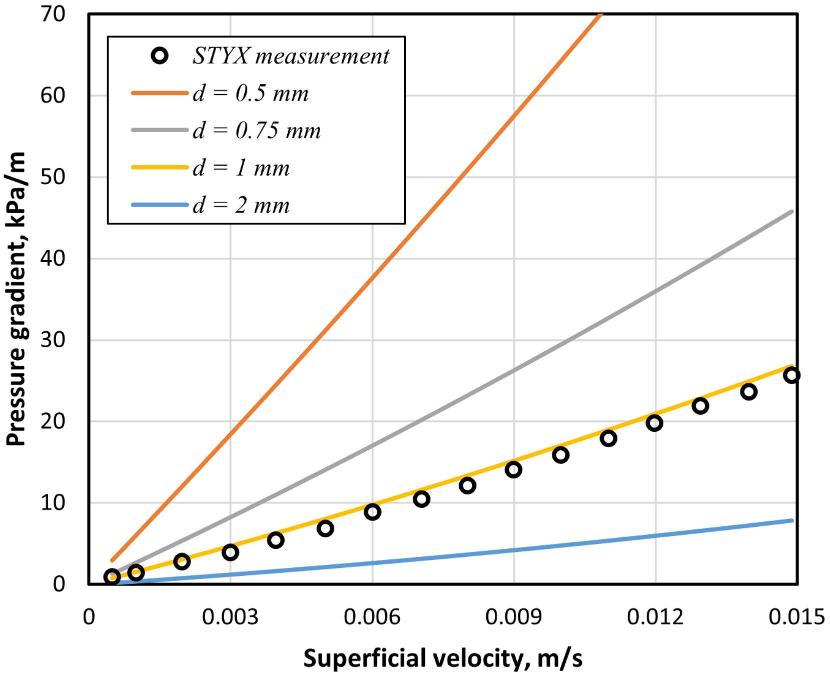

Figure 3.4: *Measured pressure gradient in STYX polydispersed bed compared with prediction of Ergun's equation for a monodispersed bed.*

area. The frictional resistance or the pressure drop, Δp across a bed of height H containing spherical particles of diameter d can be calculated using the Ergun equation as:

$$\frac{\Delta p}{H} = 150\frac{(1-\epsilon)^2}{\epsilon^3}\frac{\mu V}{d^2} + 1.75\frac{(1-\epsilon)}{\epsilon^3}\frac{\rho V^2}{d} \tag{3.1}$$

where ϵ is the porosity of the bed, and V is the superficial velocity of the fluid. For a bed randomly packed with uniform size spherical particles, the porosity is around 40%. The pressure drop in such monodispersed bed with varying superficial velocity was calculated for different particle sizes using Equation 3.1. The calculated pressure drop was then compared against the experimentally measured pressure drop in the polydispersed bed used in the STYX experiments. The results are shown in Figure 3.4.

For a bed with uniform 1 mm diameter particles, the calculated pressure drop matches well with the STYX pressure drop. This implies that the frictional resistance offered to the flow by the bed with polydispersed particle size distribution is similar to the one offered by a monodispersed bed of particle size 1 mm. Hence, an effective diameter of 1 mm can be used to model the polydispersed bed with single size particles. The packed bed is a monodispersed bed of single sized particles, with a bed porosity of about 0.4, in which the sphere diameter is close to the *effective diameter* of the STYX facility.

3.5 Experimental setup

3.5.1 Overall system description

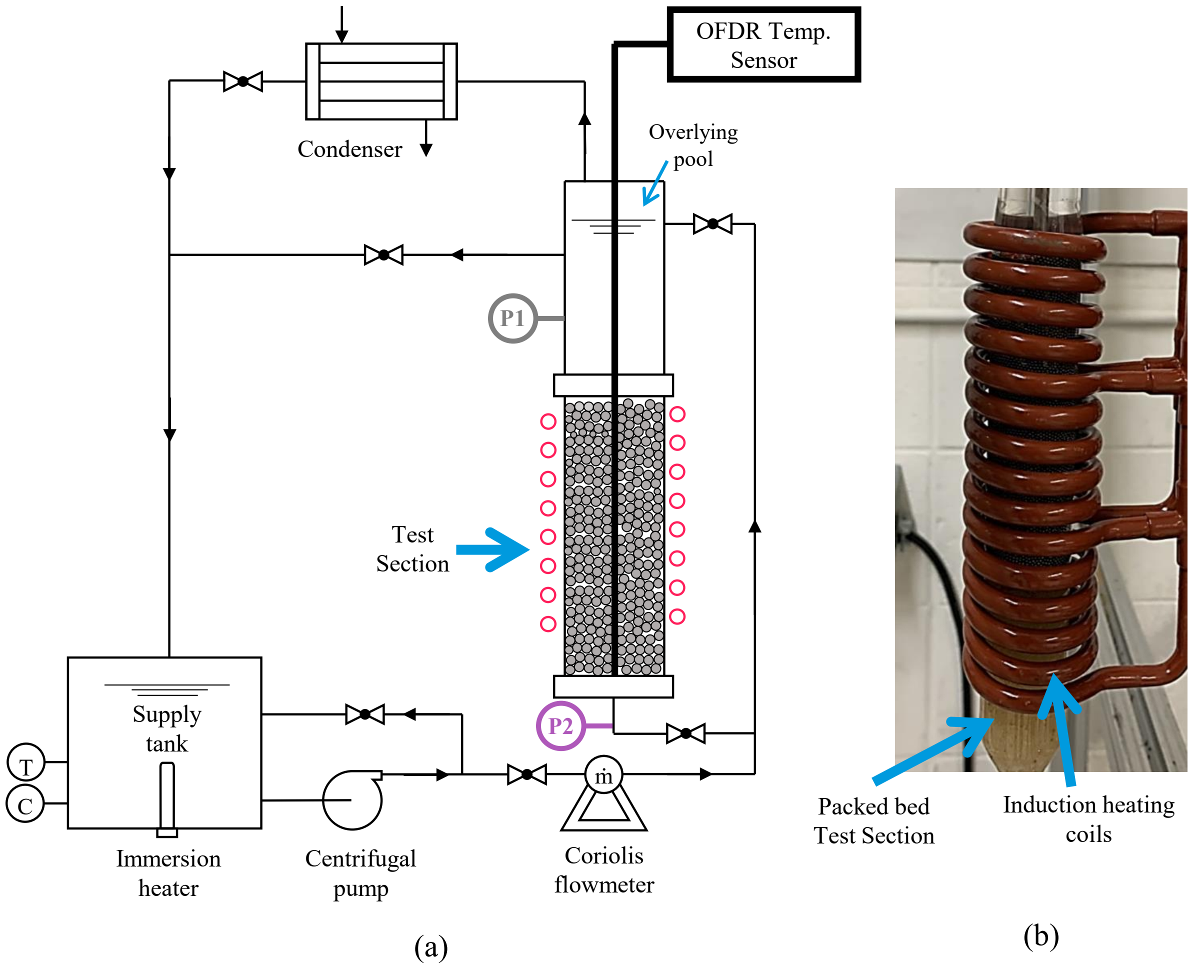

(a)

(b)

Figure 3.5: *Thermal-hydraulic loop*

The experimental facility was designed and built to study the coolability characteristics of seawater in a packed bed of spherical particles with volumetric heat generation within the spheres. The layout of the setup with its main components is shown in Figure 3.5. The coolant flows in a loop that consists of the test section, the supply tank, the pump, the condenser and various instrumentation. An induction heater is deployed to heat the spheres volumetrically. The coolant is supplied to the test section from the supply tank where it is

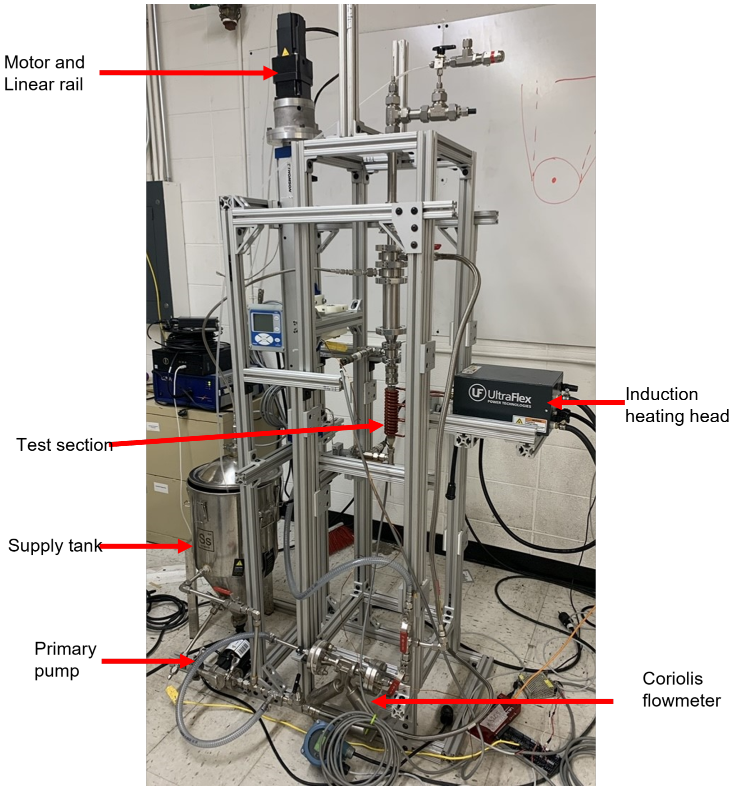

Figure 3.6: *Picture of the experimental setup with the major components.*

heated to and maintained at a desired temperature via an immersion heater. The coolant is circulated constantly within the supply tank to ensure uniform concentration & temperature and no local fouling within the tank. The pump can supply the coolant to the overlying pool and through the packed bed test section at a maximum mass flow rate of 50 g/s. The heat exchanger condenses any residual steam and sends it back to the supply tank.

3.5.2 Test Section

The test section consists of a 25 mm inner diameter, 180 mm tall cylindrical tube made of quartz glass, that houses the spheres. The spheres are of uniform 1 mm in diameter and are made of AISI 304 Stainless Steel. 304 Stainless steel spheres were chosen due to their corrosion resistant nature in saline environments, and due to the formation of an oxide layer on the surface, that causes the spheres to be electrically isolated from each other, thereby causing uniform induction heating.

3.5.3 Induction heating system

The principle of induction heating is applied to heat the spheres to simulate the decay heat of the debris bed. The test section is placed between a coil that has an alternating current flowing through it at a high frequency. The high frequency current in the coils produces a rapidly changing magnetic field around the spheres. This rapidly changing magnetic field causes eddy currents to develop on the surface of the spheres that lead to Joules heating and thus heat up the spheres. The induction heating system can supply a maximum of 5 kW at a frequency of 250kHz. The efficiency of the induction heating process is attributed to thermal and electrical efficiency. The thermal efficiency can be attributed to the thermal losses that occur due to convective and/or radiative losses to the surroundings or surrounding support structures. The electrical efficiency depends on the electrical receptivity ratio of the coil-workpiece and the relative magnetic permeability of the the workpiece[69]. To estimate the total efficiency of the induction heating system, energy balance tests were performed to measure the power input into the packed bed. This was done by having the pure water coolant flow through the heated packed bed from bottom to top at a fixed flowrate. The temperature at the inlet and outlet of the packed bed test section was then measured via RTD probes. The efficiency was then estimated by measuring heat input into the packed bed by the induction heating system using

$$\eta_o = \frac{\dot{m} C_p (T_o - T_i)}{Q_i} \tag{3.2}$$

where Q_i is the energy input into the coils,N $\dot{m}$ is the mass flowrate through the packed bed, C_p is the specific heat capacity of the fluid, and T_o and T_i are the bulk temperature of the fluid at the outlet and inlet of the packed bed, respectively.

The calculated power output as a function of the power input into the coils is shown in Figure 3.7. This calibration curve was used in estimating the power induced in the packed bed for a given power input into the coils of the induction heater.

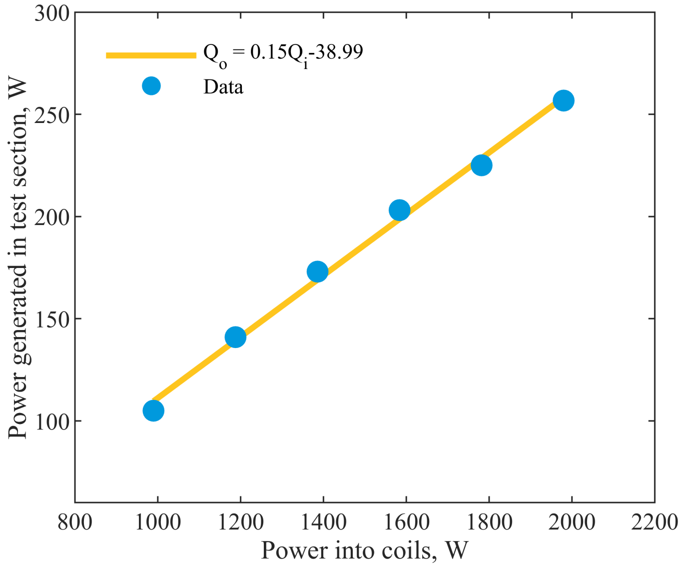

Figure 3.7: *Calibration of induction heater*

3.5.4 Swept Wave Interferometry - Distributed Temperature Sensing system (SWI-DTS)

The swept wavelength coherent interferometry distributed temperature sensor (SWI-DTS) system is able to interpret measurement distributed along its entire probe path, i.e. the entire axial length, as stated above. This allows for novel measurements using Rayleigh back-scattering principles with predictable fiber responses due to changes in temperature. The principle of operation is based on optical frequency domain reflectometery, and any localized strain in the optical fiber due to temperature change is detected by a shift in optical frequency of the Rayleigh backscattered signal. The sensor has a diameter of 1/16" and is housed in a stainless steel sheath of 1/8" outer diameter.

3.5.5 Neutron radiography setup

The test section was placed in front of the beam port of the TRIGA Mark-II reactor which provided a constant beam of neutrons for the imaging. The reactor was operated at a power of 450 kW, with an equivalent neutron flux of $2\times10^8/\text{cm}^2$. The fast to thermal neutron ratio was 2:1. The port has a series of lead collimators that create a flat beam, with the flat beam

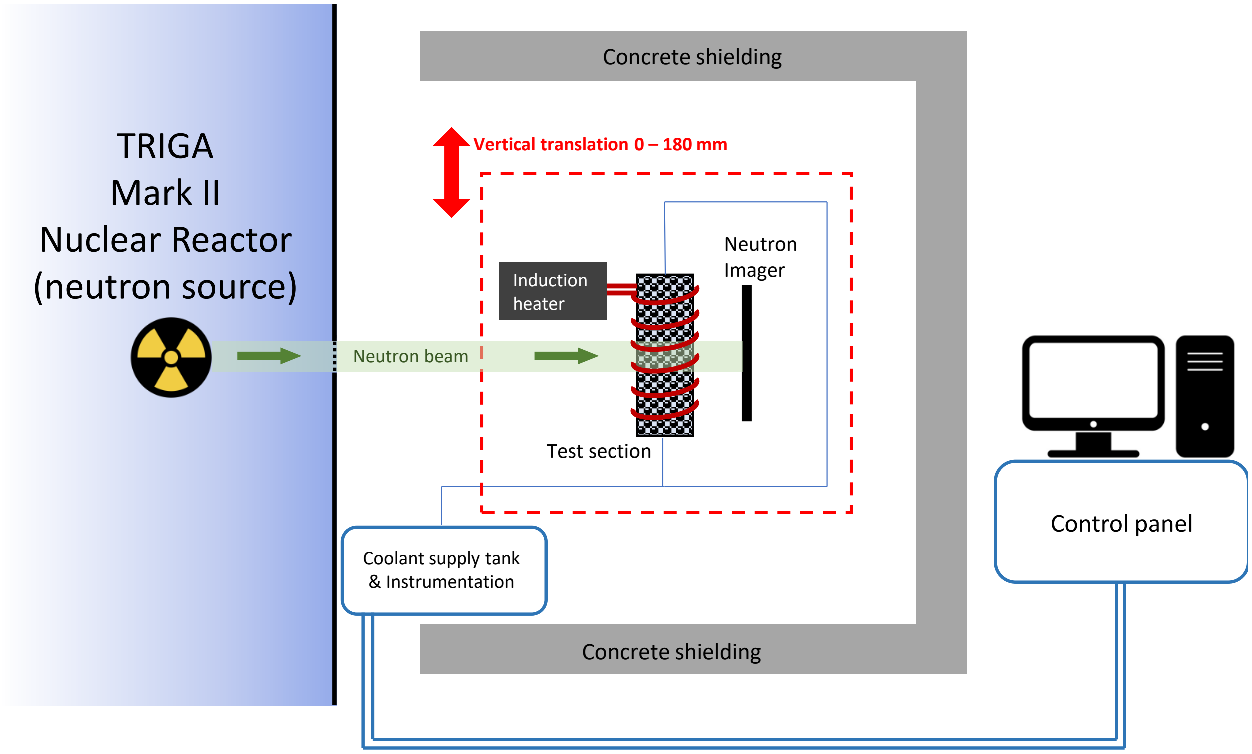

Figure 3.8: *Schematic of the neutron imaging setup with the thermal-hydraulic loop placed infront of the neutron beam for image acquisition.*

diameter of slightly greater than 1 inch. The reactor was operated at a steady power during the course of the imaging process.

A PerkinElmer XRD 0822 Flat Panel Detector was used to detect the neutron count for radiography. The detector has a pitch of 200 μm corresponding to a pixel-to-length scaling of 5 pixels/mm.

To capture the 6 inch height and 1 inch diameter of the test section using a 1 inch diameter neutron beam, the test section was mounted on a linear rail that allowed vertical translation of upto 8 inches. This allowed for a full sweep of the total length of the test section. Along with the test section, the induction heater, and the detector were mounted on the linear rail to keep their relative positions fixed with respect to each other. The linear rail had a precision of $\pm$0.1mm, allowing the test section to go back to a set elevation with high accuracy. At a set test section elevation, 5 images of 5 sec exposure each were captured, with a total of 25 sec exposure at each elevation. A total of 13 elevations were captured

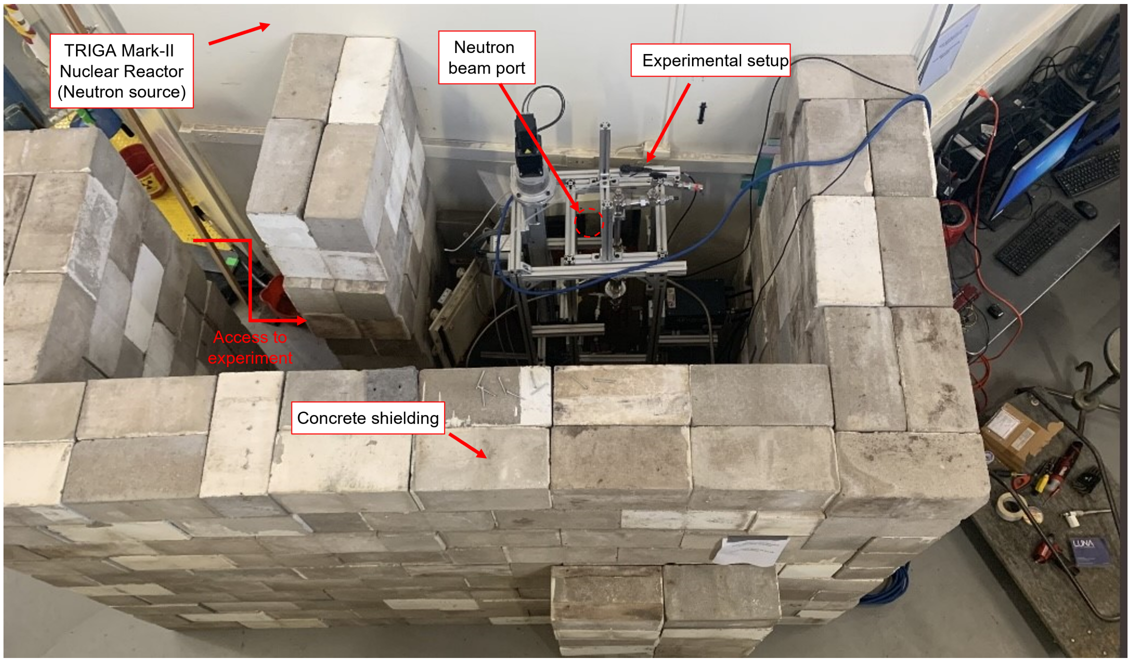

Figure 3.9: *Picture of the experimental setup in front of the reactor neutron port for neutron imaging.*

to cover the entire boiling length of the test section. Therefore, the total imaging time was just over 6 minutes for a given test run. The images taken at various elevations were stitched/stacked to create a radiograph covering the entire boiling length in the test section. To quantify the void fraction of the two phase flow from radiographs, the entire length of the test section with no water (100% void fraction) and only water (0% void fraction) was captured as the reference measurement. This methodology is discussed in the next section.

3.5.6 Start up procedure

To begin a test, the coolant was set to the desired temperature in the supply tank and was continuously pumped in the overlying pool of the test section to enable steady flooding of the test section from the top. A steady state was achieved when all the temperature measurements in the system and the pressure plateau at a steady value. Upon reaching a steady state, the induction heater was turned on. For dryout tests, the induction heating power was set to low values to achieve steady state boiling. Once steady state boiling conditions were achieved, as measured from the pressure and temperature measurements, the heating power was incremented in small steps of 50 W until the dryout conditions were observed. At each power step, the power was kept at a constant value for about 600 s, to allow the system to stabilize and reach steady conditions. When dryout was detected, the experiment was shut off at the point where the peak local temperature in the bed reached 200 °C. For the fouling tests, a constant power lower than the dryout power was set and the measurements of temperature and pressure were made over time.

3.6 Void fraction quantification methodology using Neutron radiographs

This section presents the post processing procedure and the calculations for quantifying the vapor void fraction from the neutron radiographs. MATLAB 2020b code was used for all numerical calculations and data processing.

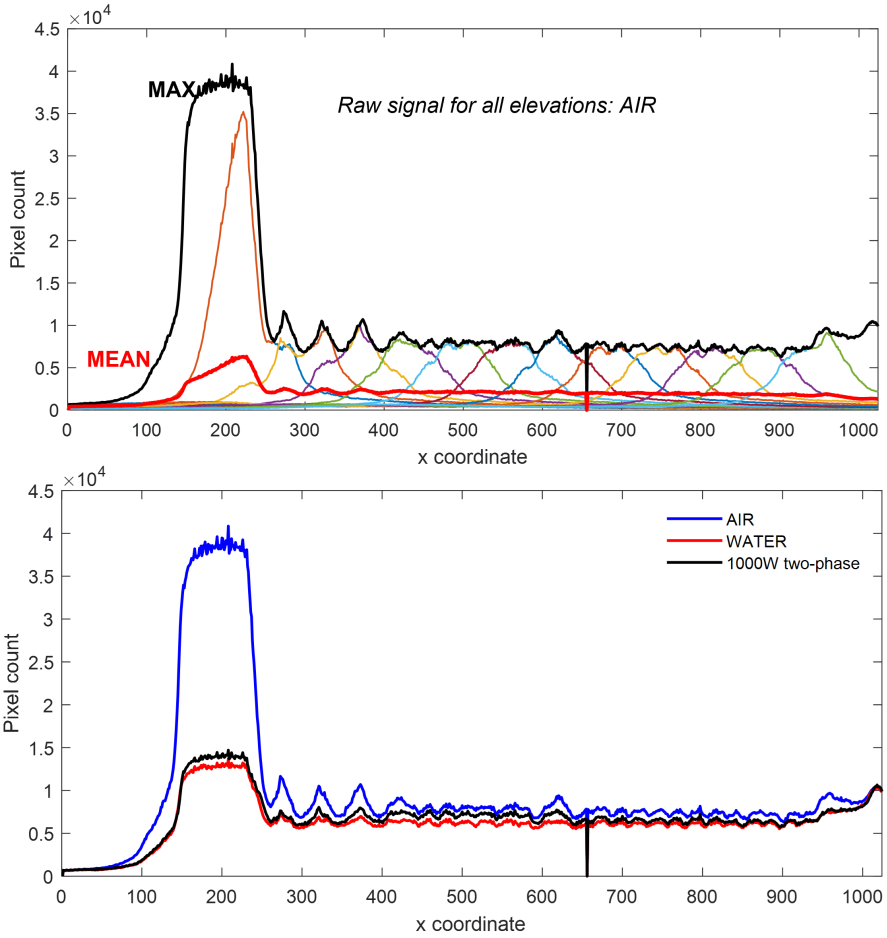

Figure 3.10: *Axial pixel values showing the stacking of images using local maxima (top). The axial pixel values for the reference cases of air and water and the test case of two phase flow show the contrast in the signal (bottom).*

3.6.1 Image post-processing

Before calculating the void fraction, a median filter was applied to reduce salt-and-pepper noise from the radiographs. The window size of the median filter was adjusted to have optimum signal/noise ratio. Following the median filter, the maximum pixel value at a pixel coordinate across all the radiographs at varying elevations was used for stitching the radiographs. This stitching method causes the radiographs captured at 13 different locations to combine and produce a single radiograph covering the entire length of the test section. This is shown in Figure 3.11. A comparison of the axial pixel values for the radiographs are shown in Figure 3.10. The image was then cropped to remove unimportant background and increase image processing speed.

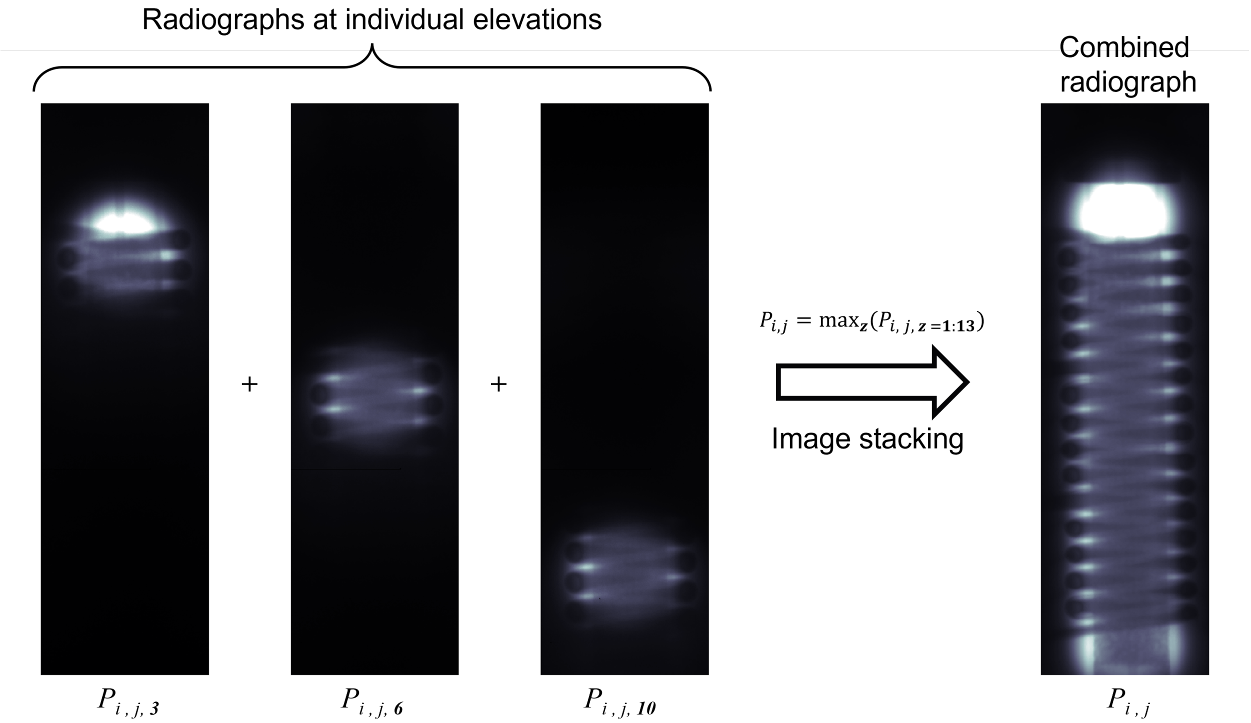

Figure 3.11: *Image stitching/stacking of radiographs at various elevations to create a radiograph of the entire test section length.*

3.6.2 Void fraction quantification

A quantitative estimate of the vapor void fraction can be performed using the neutron attenuation principles. The attenuation of neutrons through a material follows the Beer-Lambert law,

$$\frac{I}{I_0} = e^{-\Sigma_f t} \tag{3.3}$$

The pixel value measured by the detector is directly proportional to the neutron flux incident on the detector and is given by the equation,

$$P_f = Ce^{-\Sigma_f t} \tag{3.4}$$

The subscript f denotes particular experiment test run. Similarly, for air (100% void) and water filled (0% void) reference cases, the pixel relationships are $P_a = Ce^{-\mu_a t}$ and $P_w = Ce^{-\mu_w t}$ respectively. The attenuation coefficient for fluid comprising two phases (vapor and water), can be assumed to be linearly related to water or void fraction and expressed as:

$$\mu_f = \alpha\mu_a + (1 - \alpha)\mu_w \tag{3.5}$$

Taking the log-transform of the pixel-values, P, leads to the following after some algebraic manipulation:

$$\alpha = \frac{\log(P_f) - \log(P_w)}{\log(P_a) - \log(P_w)} \tag{3.6}$$

This gives the ratio of the total path traveled by the neutron in vapor to the total path length within the pores in the test section. The highest signal to noise ratio would be at the largest neutron path distance ie. at the axis of the test section, and near wall measurements would have a lower signal to noise ratio.

The axial variation of the void fraction, α_z was calculated using a weighted average of the void fraction across a given cross section. The weighting was performed as a function of the neutron travel path, or the chord length of the test section at various distances from the central axis of the test section, represented by x. This is formulated in Equation 3.7.

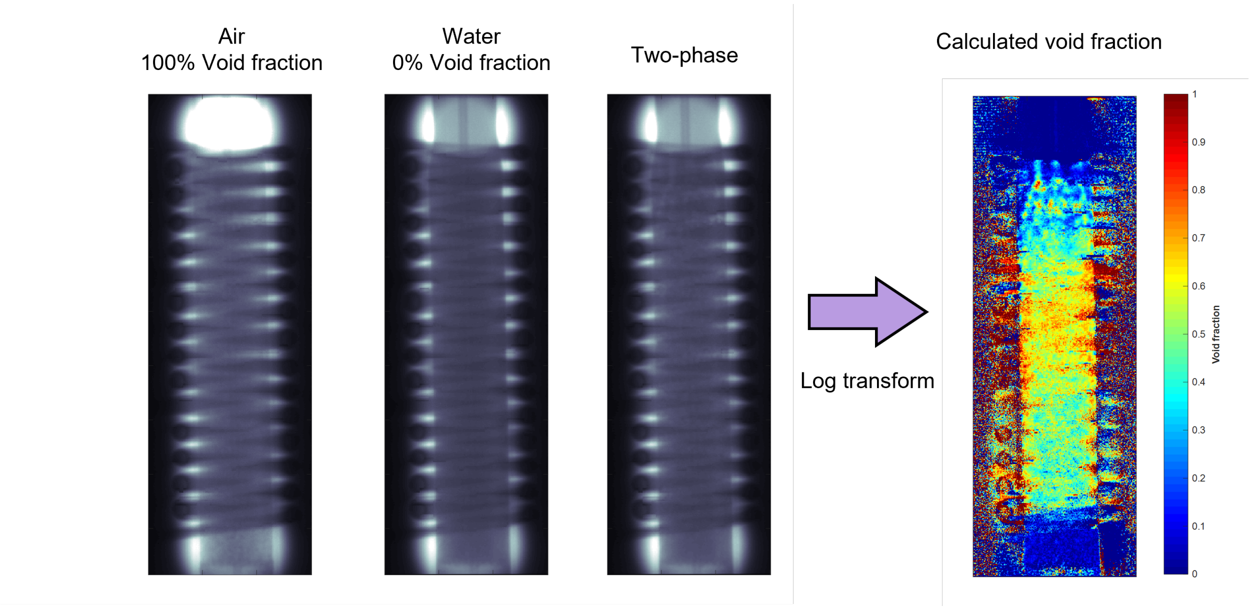

Figure 3.12: *The log transform shown in equation 3.6 was applied to the stitched neutron radiographs to extract void fraction information.*

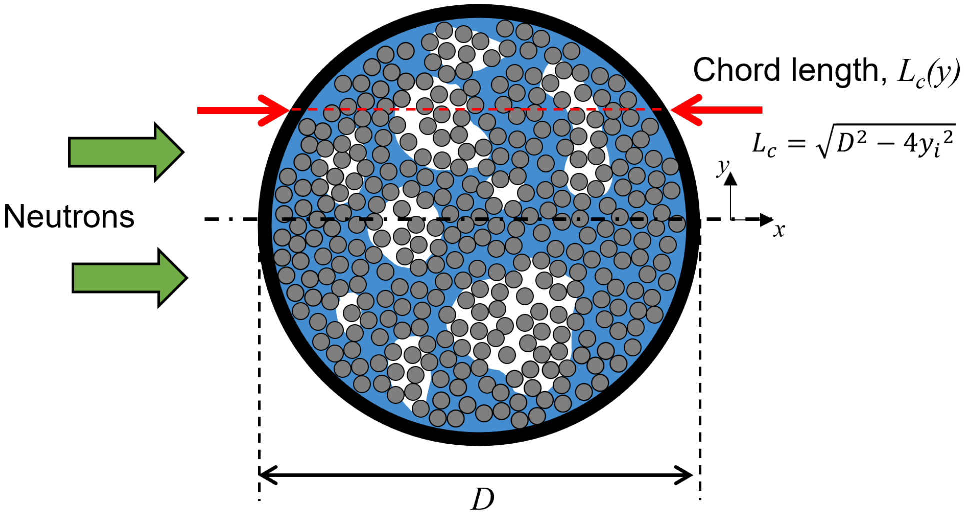

Figure 3.13: *Test section cross-section with chord length varying with radial dimension*

Here, D is the diameter of the test section, and $\alpha_{x,z}$ is the void fraction measured at a given coordinate.

$$\alpha_z = \sum_{y=-r}^{y=r} \alpha_{y,z} \frac{L_{c,y}}{A_y} \tag{3.7}$$

with cross sectional area in pixel squared,

$$A_y = \sum_{y=-r}^{y=r} L_{c,y} \tag{3.8}$$

Here, L_c is the chord length in pixels at radial position given by $L_c = \sqrt{D^2 - 4y_i^2}$, as depicted in Figure 3.13. This yields the area wise vapor fraction, or the fraction of the area, within the pore space of the packed bed, that is filled with vapor.

Chapter 4

Experimental results and discussion

This section presents the results of the experiments conducted on the debris bed facility. Thermal response of the test section is presented along with void fraction measurements. Steady state boiling measurements are presented to establish baseline performance under fixed conditions. The transient of the dryout is measured and the critical dryout heat flux at which dryout occurs is measured at varying parameters. The longterm thermal response of the bed is represented to demonstrate the long term effects of using seawater in debris bed cooling.

4.1 Steady state boiling

Steady state boiling tests were conducted for pure water and seawater for heat fluxes lower than the critical dryout heat flux. The temperature response of the system as measured from the SWI-DTS system is shown in Figure 4.1. Once the induction heater was turned on, the temperature throughout the test section increased from the initial temperature and stabilized at the saturation temperature, indicating a steady liquid-vapor counter current flow in the packed bed. During the steady state, the temperature and pressure stay constant throughout the time scale of the experiment. For longer timescales, a temperature transient is observed with seawater, which will be discussed in a later section.

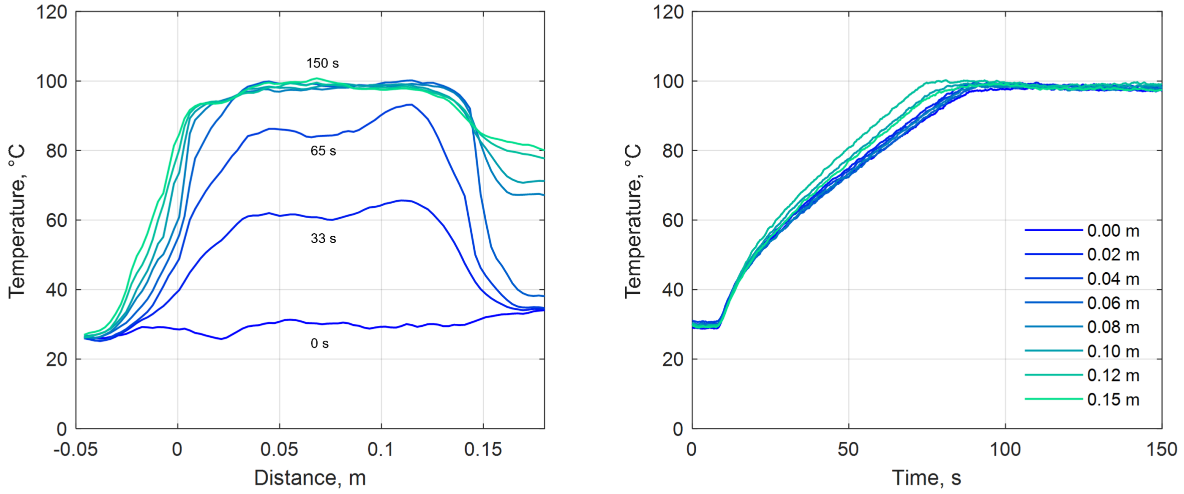

Figure 4.1: *Thermal response data of the test section from SWI-DTS system during initial transient to reach steady state*

The measured void fraction from the neutron radiographs is shown in Figure 4.2. The three images at increasing heat fluxes show steady boiling with regions of low void fraction in the lower and upper region, with the maximum void fraction in the upper half of the test section. In the lower region, the void fraction increases with the elevation in the test section. The volumetric vapor generation rate is constant in the region where saturated boiling occurs, and this generated vapor moves upwards due to the buoyancy effects. Therefore, with an increase in elevation, the vapor generated locally and the vapor generated below that elevation accumulates and leads to an increase in void fraction with height. However, this increase in void fraction with elevation is only valid in the region where the liquid is in the

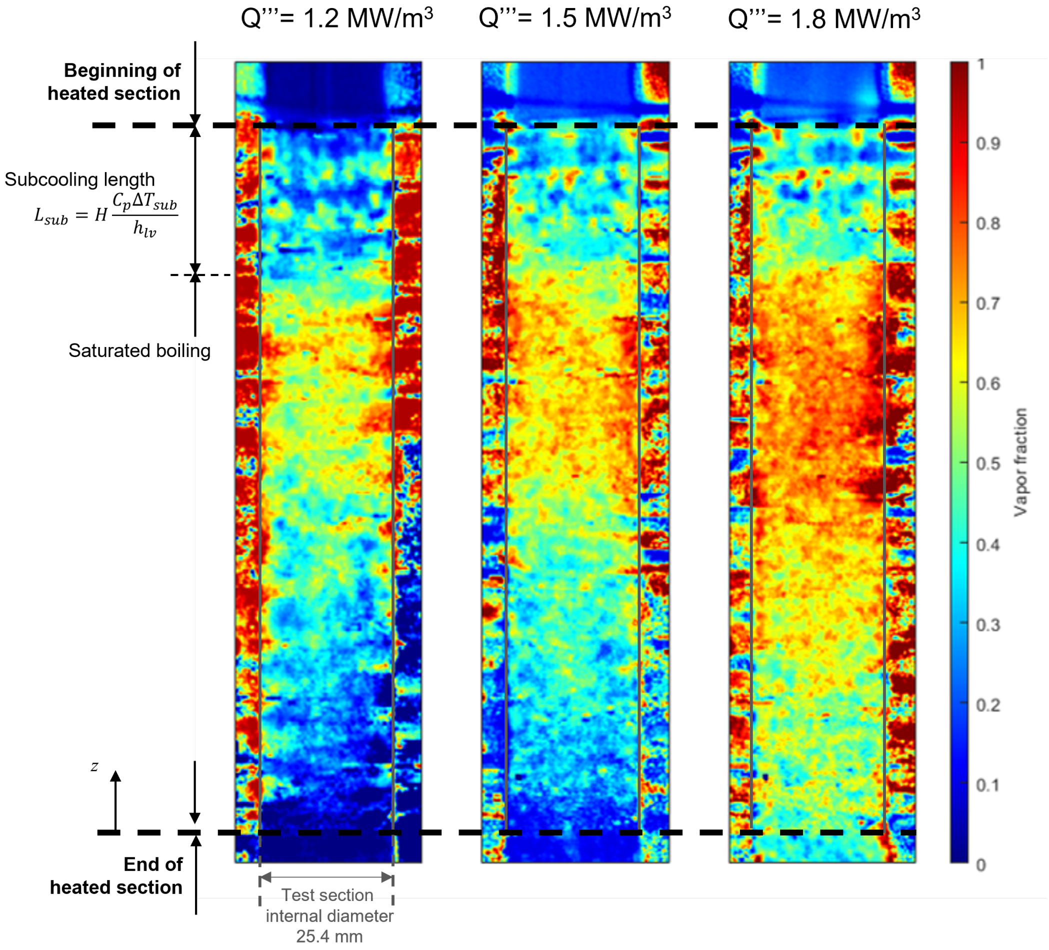

Figure 4.2: *Measured void (vapor) fraction in the packed bed test section from neutron radiographs. The void fraction increases with elevation in the saturated boiling region, with a region of subcooled boiling in the upper regions. The maximum void fraction increases with increase in the heat generation rate.*

saturated conditions undergoing saturated boiling. In the upper region, the percolating liquid is in a subcooled state, which percolates for a certain amount of distance before it reaches the saturation conditions. This region of subcooled boiling is coupled with the quenching of vapor from the lower regions of the test section, leading to a decreasing void fraction with elevation in the upper regions of the test section.

4.2 Experimental measurement of dryout

4.2.1 Measurement of dryout in pure water

To measure the volumetric heat flux at which dryout occurs, the power of the induction heater was increased gradually in steps. A dryout was observed when a rapid temperature excursion was observed in the bed. Figure 4.3 shows the power increments taken to measure the dryout. The first power step was taken to heat up the fluid in the packed bed to reach steady boiling conditions. At 1000 s, upon further increment of power, a rapid rise in temperature at a rate of 0.34°C/s in the lower region of the bed was observed, as shown in Figure 4.4. This rapid rise in temperature is an indication of the the occurrence of dryout in the bed. This rise in temperature was preceded by a smaller spike in temperature that indicates the formation of an unstable dry zone that soon progresses into a stable dry zone. The unstable dryzone can be expected to occur near the critical dryout heat flux[43;63].

Upon reaching the dryout power, an immediate drop in pressure in the lower region of

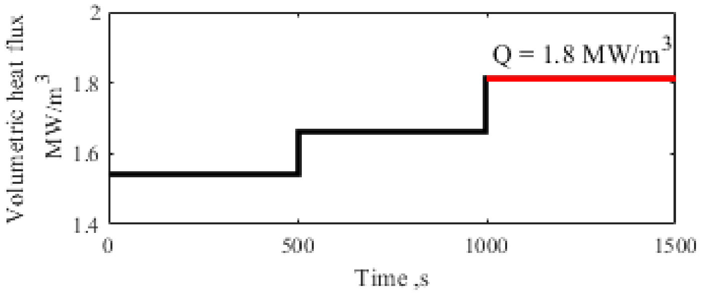

Figure 4.3: *Pure water (0% conc.): Power steps taken to measure the dryout heat flux. The dryout occurred at 1.8 MW/m^3 for the test shown in Figure 4.4 and 4.5.*

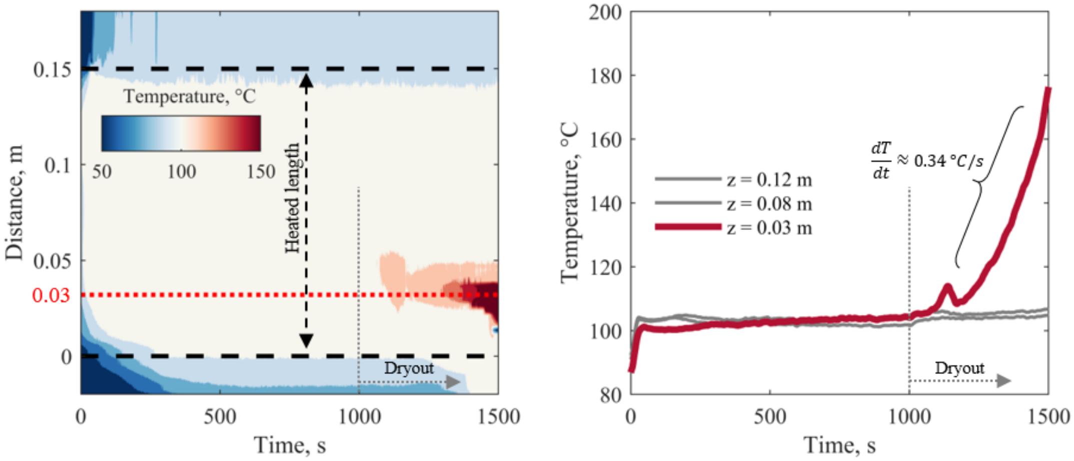

Figure 4.4: *Pure water (0% conc.): The temperature contour plot (left) shows that the temperature throughout the bed stays at saturation temperature of 100 °C until the increment to the dryout power, after which a region of high temperature is observed in the lower region of the bed at z = 0.032 m. The line plot (right) shows a steady increase in temperature at a rate of 0.34 °C/s at z = 0.032 m while the rest of the packed bed stays at constant saturation temperature.*

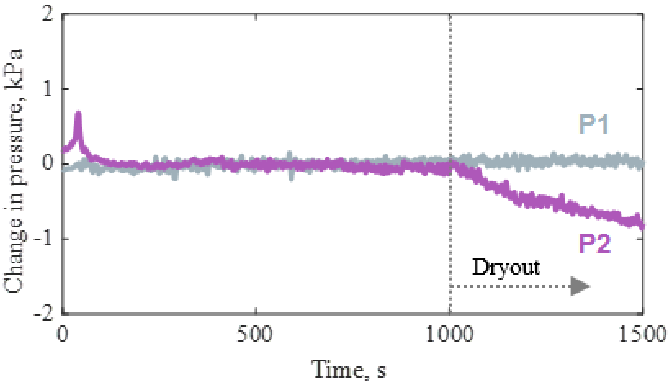

Figure 4.5: *Pure water (0% conc.): A constant pressure at the top (P1) and a reduction in the pressure at the bottom (P2) indicates a reduction in the liquid hold-up during dryout.*

the bed was observed as shown in Figure 4.5. This drop in pressure is indicative of the net hydrostatic head reduction, due to the formation of the dry zone. As the dry zone is formed, the liquid hold-up in the packed bed is gradually reduced below the initial dryout location due to the lack of access of the replacement liquid to the lower region. This reduction in the liquid hold-up results in a reduction in the hydrostatic pressure, and this is reflected in the pressure measurements shown in Figure 4.5. Therefore, an incipient dryout volumetric heat

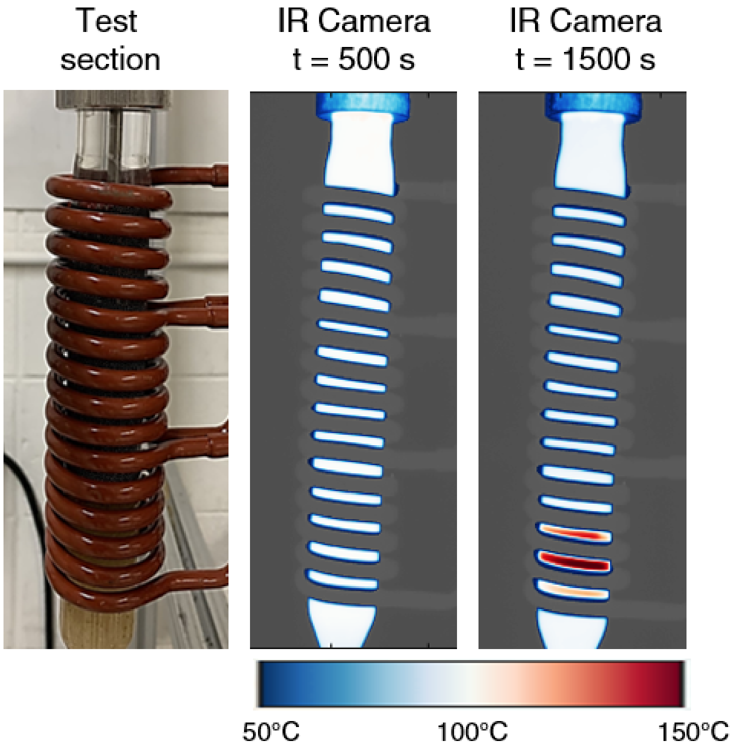

Figure 4.6: *The dry spot (indicated by temperature ¿ 100°C) covers the entire cross section suggesting no percolation from low porosity region near the walls.*

flux of 1.8 MW/m^3 was measured for the test with pure water.

The formation of this dry zone is not restricted along the axis of the test section, but rather spreads azimuthally to cover the entire cross section with vapor. This is verified by temperature measurements of the outside walls using an infrared camera as shown in Figure 4.6. This suggests that the formation of the dry zone also prevents the fluid from percolating from the higher porosity regions near the walls of the test section, indicating that the effect of multidimensional flooding is not dominant in the current experimental setup.

4.2.2 Variation of dryout heat flux with bed height

With the dryout heat flux measurement established, the variation of dryout heat flux was measured with varying bed height. This is presented in Figure 4.8. The dryout heat flux varied inversely with the height. With an increase in bed height, the increased total mass of vapor generated causes an increase in the mass flux of vapor leaving the top of the test

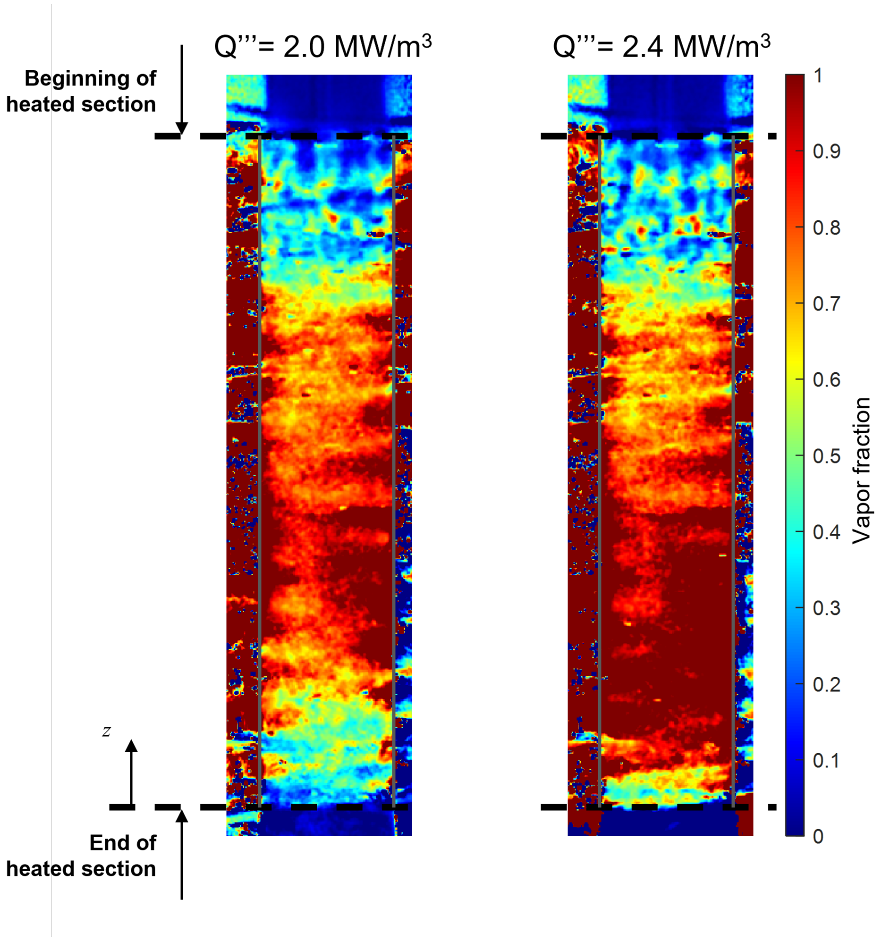

Figure 4.7: *Measured void fraction for* $Q''' \approx Q''_d$*(left) and* $Q''' > Q'''_d$*(right)*

section. This increase in mass flux adds additional resistance to the liquid percolating from the top of the bed. This causes a decrease in dryout heat flux with an increase in the bed height.

4.2.3 On the location of dryout with excess superheat

As shown in Figure 4.4 and Figure 4.6, dryout occurs in the lower region of the debris bed. The location of the occurrence of the dry spot is dependent on the degree of super heat, or the magnitude of heat flux higher than the critical dryout heat flux. For heat fluxes near the critical dryout heat flux, the dryout can be expected to be at the bottom of the test section. Increasing the heat flux results in the dryout occurring higher up in the bed. This is verified by experimental results shown in Figure 4.9. In these set of experiments, the heat

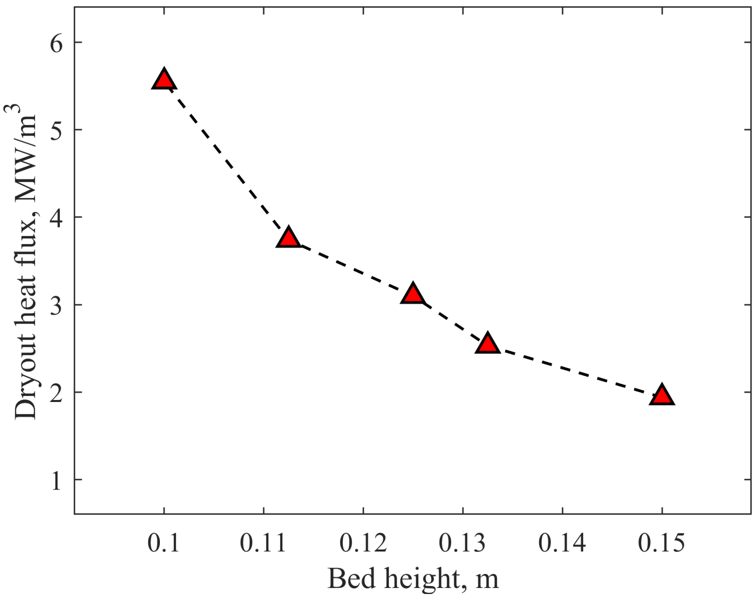

Figure 4.8: *Variation of measured dryout heat flux with bed height.*

flux was set to be slightly lower than the dryout heat flux and a varying power steps were taken to achieve dryout. As shown in Figure 4.9, at heat flux equal to the dryout heat flux, the dryout occurs at the bottom. Stepping the heat flux from below the dryout heat flux to 1.3 times the dryout power increases the height of the dryout zone by to 0.055 m. Similarly, a stepping of heat flux from below dryout heat flux to 1.7 times and 2 times the dryout heat flux raises the dryout location to 0.081 m and 0.103 m respectively. Increasing the heat flux increases the vapor generation rate which adds additional resistance to the incoming percolating liquid. Thus the depth of percolation of the incoming cooling water is further reduced leading to a dry spot occurring higher up in the bed.

4.2.4 Measurement of dryout in seawater

The measurement of the dryout process for salt water at a concentration of 7%, twice that of seawater is presented in Figure 4.10. As shown in Figure 4.11, a power step was taken every 300 s until the dryout was observed. The smallest power step of 50 W was taken. The temperature measurements shown in Figure 4.10 show that there was a gradual temperature rise in the lower region of the bed, until the power step at 2200s, after which the rate of

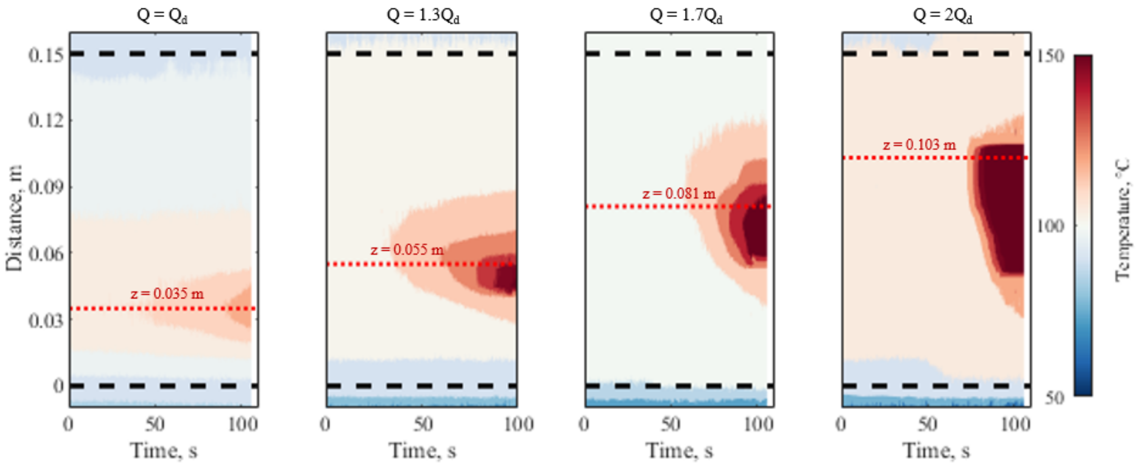

Figure 4.9: *The axial temperature measurements from the time of dryout (t_d) show that the dryout location depends on the degree of excessive heat flux above the critical dryout heat flux.*

change of temperature rise increased. The reduction in absolute pressure in the lower test section occurred at this power step at 2200 s as shown in Figure 4.12, and thus this power step was considered as the dryout volumetric heat flux.

The rise in temperature in the the bed can be contributed to two mechanisms : fouling and dryout. For heat fluxes below the dryout heat flux, a fraction of the percolating liquid is

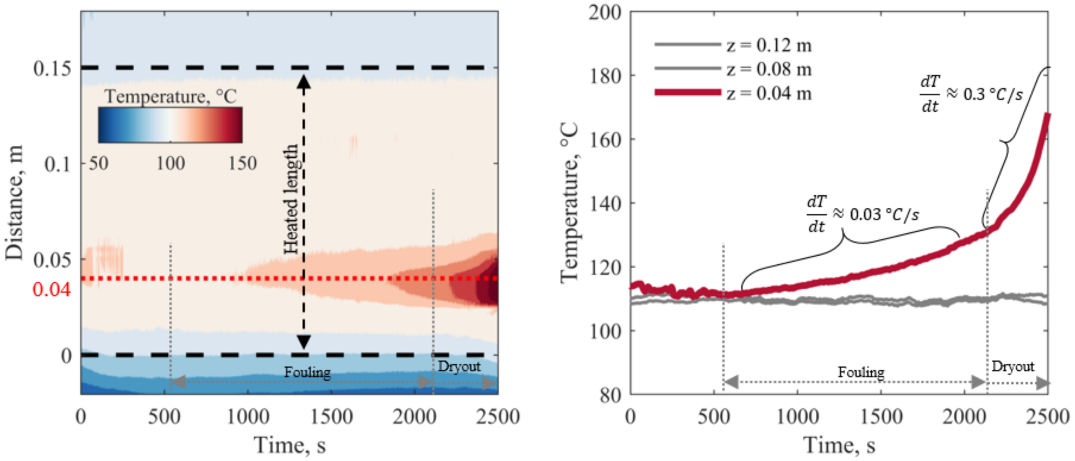

Figure 4.10: *Salt water (7% conc.): The temperature contour plot (left) shows that the temperature throughout the bed stays at saturation temperature except in the lower region where a gradual increase in temperature is observed indicating fouling. After the increment to the dryout power, a steep temperature rise is observed indicating dryout.*

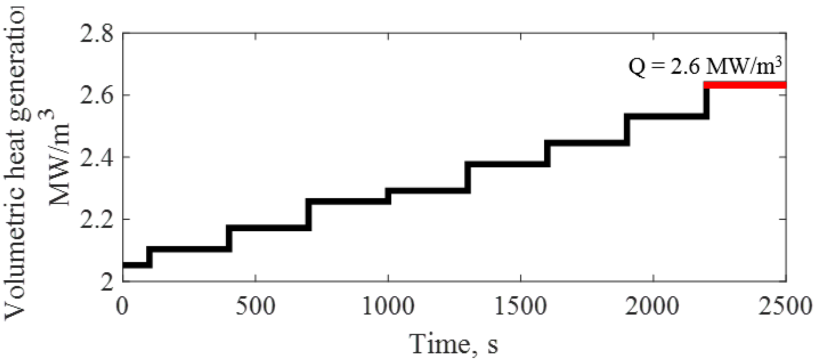

Figure 4.11: *Salt water (7% conc.): Power steps taken to estimate the dryout heat flux. The dryout occurred at 2.6 MW/m^3 for the test shown in Figure 4.10 and 4.12.*

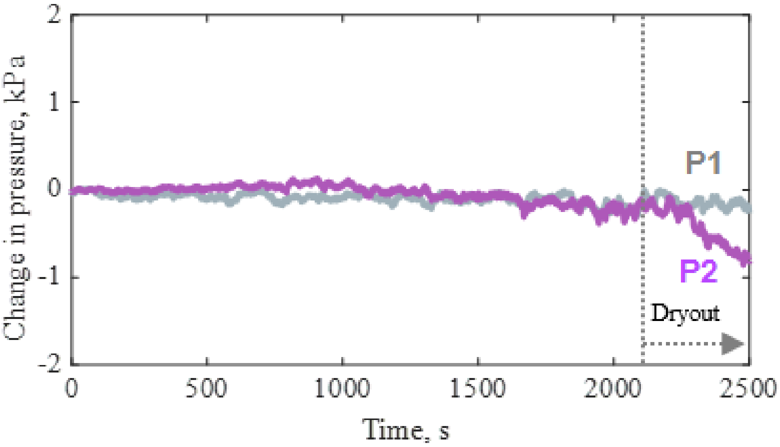

Figure 4.12: *Salt water (7% conc.): A constant pressure at the top (P1) and a reduction in the pressure at the bottom (P2) indicates a reduction in the liquid hold-up during dryout.*

converted into vapor that moves up and out of the bed, while the dissolved salt stays in the remaining liquid percolating downwards. This causes the concentration of the dissolved salts in the fluid to increase as the fluid percolates further in the bed. Thus the highest concentration of the dissolved salts can be expected to be in the lowest regions of the debris bed. With the progression of time, as more and more liquid boils off, the dissolved constituents start to precipitate out and deposit on the surfaces of the spheres. This causes the thermal resistance to build up on the spheres along with a reduction in porosity in the region of high salt concentration. This deposition mechanism or the fouling mechanism causes the local heat transfer coefficient to reduce linearly with time and thus a linear increase of temperature is observed in the bed before the dryout. When the volumetric heat exceeds the critical dryout power, the slope of temperature rise increases. This second region of temperature increase is attributed to the occurrence of dryout, where the liquid percolation is restricted and the major mode of cooling in the dry zone is convection into the vapor phase.

During salt deposition in the pores, the geometric characteristics of the packed bed change over time. To isolate the dryout phenomena from fouling, the test with salt water at 7% concentration was repeated with different incremental power time steps.

It was observed that a small time step for a power increment causes an instability and induces a premature dryout. On the other side, if a longer time is taken between power steps, then the geometric characteristics (porosity) of the debris bed can change due to the fouling process. Thus, the experiment was repeated at multiple time steps to measure its effect on the dryout volumetric heat flux. The results of different repeats are summarized in Table 4.1. The variation in the dryout power at different time steps is negligible as even a 300 s time step wasn't long enough for the fouling process to change the geometric characteristics of the bed to have a significant effect on the volumetric dryout heat flux.

Measurements of dryout for seawater at varying heights show similar trend to that of pure water. The dryout heat flux reduces with an increase in the bed height. However, the dryout heat flux is higher in seawater at all bed heights as shown in Figure 4.13.

Measurements of the dryout heat flux at a fixed height and varying concentration of dissolved salts show that there is a gradual increase of dryout power as the concentration is increased. This is depicted in Figure 4.14. Multiple repeats of the dryout power measurement show the nature of the spread of dryout power measurement for a given concentration, and show that the overall trend of the dryout power is an increase in coolability with an

Table 4.1: *Salt water (7% conc.): The measured dryout heat flux as a function of power time step increments.*

Time interval between power increment, s	Measured volumetric dryout heat flux, MW/m^3
150	2.75
150	2.63
200	2.63
300	2.63

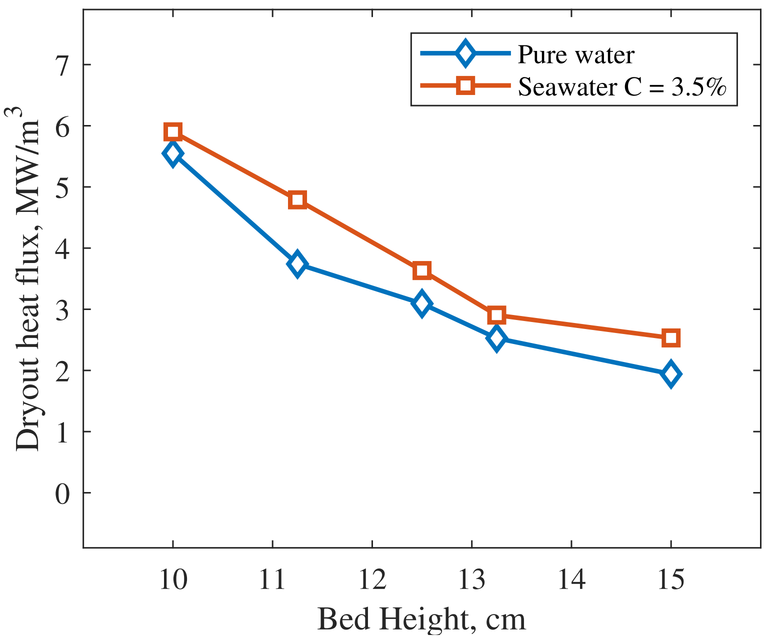

Figure 4.13: *Comparison of dryout heat flux with height between pure water and seawater.*

increase in the concentration of dissolved salts. The higher dryout heat flux can be explained with the help of pressure drop. The addition of salts into water has shown to reduce the frictional characteristics or pressure drop during two phase flow. This reduction in frictional characteristics results in an increase in the dryout heat flux.

4.3 Longterm effect of dissolved salts on coolability

The increase in the dryout heat flux with the addition of dissolved salts is a temporary enhancement of coolability. The fouling process causes a thermal resistance buildup over time that leads to plugging of the pores with the precipitated salts. The salt deposition over time causes an increase in flow resistance to the transport of liquid and vapor phases in the bed, and over time can cause the pores to plug and completely restrict the movement of the fluid inside the bed. This plugging causes the temperature in the heated bed to increase and can progress the meltdown of the reactor.

Experiment at a constant heat flux below the dryout heat flux show that the gradual build

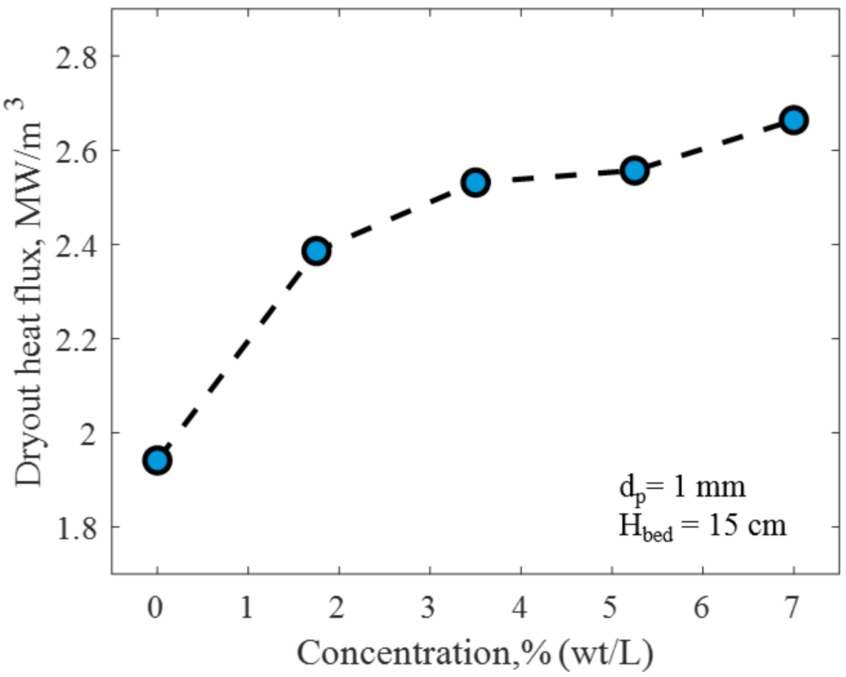

Figure 4.14: *Variation of the measured dryout heat flux with salt concentration*

up of salts leads to a gradual increase in temperature in the lower regions of the bed where higher concentration of salts is expected. The temperature and pressure measurements for an experimental case for a packed bed of height 15 cm and 1.5 MW/m^3 is shown in Figure 4.15 and 4.16. The temperature rises gradually from 100 °C to 112 °C over the course of 6000 s. After 6000 s, a steeper temperature rise is observed. At 7900s, the spike in pressure measurements indicate the plugging of the entire cross section of the packed bed with the salts at a certain elevation, and these plugged pores restrict the movement of vapor out of the bed. This causes the pressure in the lower region of the bed to build up over time. This pressure build up only in the lower region indicates that the region above the bed is cooling under stable conditions, but the plugging of the cross section at a certain elevation causes the bed below the plugged cross section to increase in pressure.

These results suggest that the cooling with seawater is a transient process, even for heat fluxes lower than the dryout heat flux. The addition of salts adds a restricted timeline during which the bed is coolable. During this time, the dryout heat flux is higher for salt water as compared to pure water. After a certain amount of time, the growth of the salts

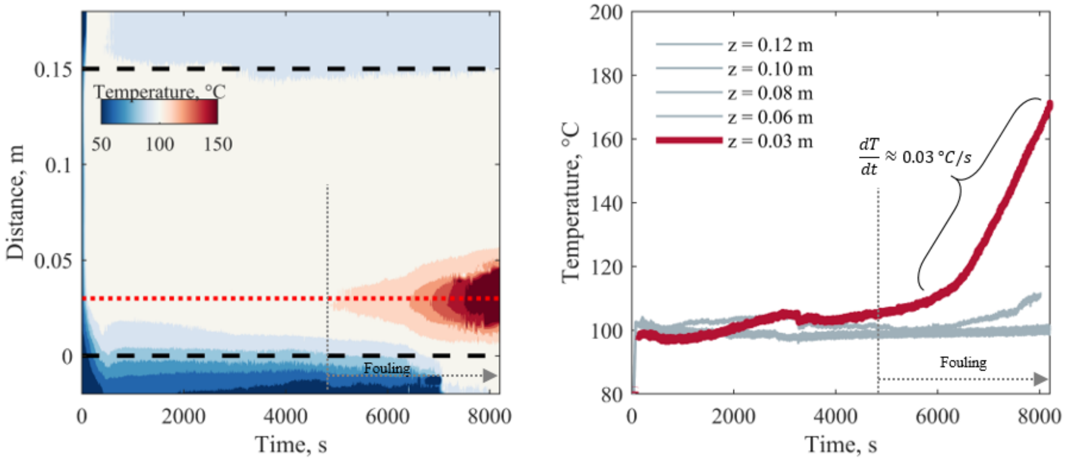

Figure 4.15: *Salt water (3.5 % conc): At a constant volumetric heat flux of 1.5 MW/m*^{3}*, the temperature contour plot (left) shows that the temperature throughout the bed stays at saturation temperature except in the lower region where a gradual increase in temperature is observed indicating fouling.*

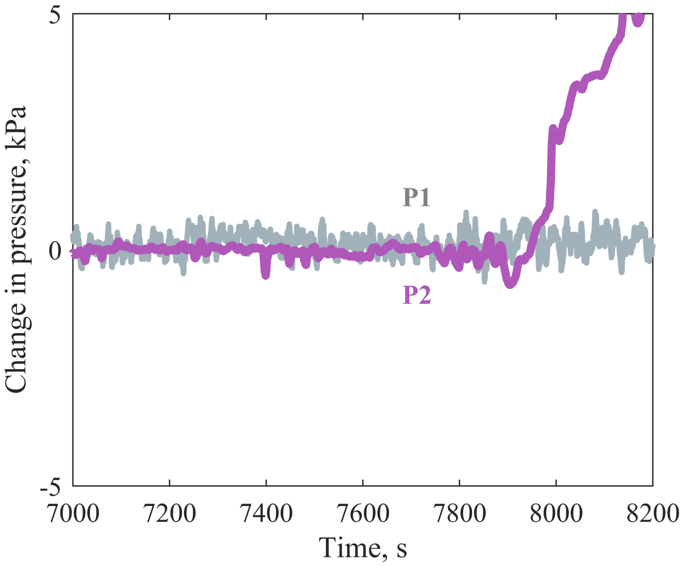

Figure 4.16: *Salt water (3.5 % conc): Pressure measurements show a constant pressure at the top (P1) and a build up of pressure at the bottom (P2) due to plugging of cross section after a certain amount of time.*

in the pores contribute to an increase in temperature in the bed, followed by an increase in pressure below the cross section that is plugged. This increase in pressure due to the build up of salts can have tendencies to disrupt the geometry of the debris bed and may lead to additional complications including an explosive spread of the debris in the reactor cavity area. Therefore, further research and modeling is required to fully understand the time scales at which the debris bed can have its cross section plugged when salt water is used as a coolant.

4.4 Comparison of experimental measurements with analytical models

4.4.1 Debris bed coolability model description

To assess debris bed coolability in reactor safety analysis, a great number of analytical models and empirical correlations were developed for prediction of single/two-phase flow (friction) and heat transfer (dryout heat flux) in particulate beds. Satisfactory predictions of frictional pressure gradient of single-phase flow in the porous media can be obtained with the use of semi-empirical models such as the Ergun equation[70]:

$$-\frac{dp}{dz} = 150\frac{(1-\epsilon)^2\mu}{d^2\epsilon^3}v + 1.75\frac{(1-\epsilon)\rho}{d\epsilon^3}v^2 \tag{4.1}$$

where μ is the viscosity, d is the particle diameter, ϵ is the porosity and v is the fluid superficial velocity.

This equation can be modified for two-phase liquid-vapor flow as:

$$-\nabla P_v = \rho_v g + \frac{F_{pv}}{\epsilon\alpha} + \frac{F_i}{\epsilon\alpha} \tag{4.2}$$

$$-\nabla P_l = \rho_l g + \frac{F_{pl}}{\epsilon(1-\alpha)} - \frac{F_i}{\epsilon(1-\alpha)} \tag{4.3}$$

where ρ, g, α, and F_i are the density, gravitational acceleration, void fraction of vapor, and interfacial friction, respectively. The subscript "g" denotes gas and "l" denotes the liquid phase. To include the effective cross-section of each fluid phase, the relative permeability and passability, denoted as K_r and η_r, respectively, are additionally considered in the solid-fluid friction force in the two-phase friction models. They are listed in Tables 4.2. For the Rahman model, the relative permeability and passability are dependent on the two-phase flow regime, and are presented in Table 4.3. The friction between the particles and the gas phase (F_{pv}) and the friction between the particles and the liquid phase (F_{pl}) are expressed as:

$$F_{pv} = \epsilon\alpha\left[\frac{\mu_v}{KK_{rv}}j_v + \frac{\rho_v}{\eta\eta_{rv}}|j_v|j_v\right] \tag{4.4}$$

$$F_{pl} = \epsilon(1-\alpha)\left[\frac{\mu_l v}{KK_{rl}}j_l + \frac{\rho_l}{\eta\eta_{rl}}|j_l|j_l\right] \tag{4.5}$$

where μ, j are the dynamic viscosity and superficial velocity, respectively. The permeability (K) and passability (η) are defined by Ergun[70] as:

$$K = \frac{\epsilon^3 D_p^2}{150(1-\epsilon)^2} \tag{4.6}$$

$$\eta = \frac{\epsilon^3 D_p^2}{1.75(1-\epsilon)} \tag{4.7}$$

Table 4.2: *Relative permeability, passability and interfacial drag terms in models.*

Model	K_{rl}	η_{rl}	K_{rv}	η_{rv}	F_i
Lipinski[71]	$(1-\alpha)^3$	$(1-\alpha)^3$	α^3	α^3	-
Muller[8]	$(1-\alpha)^3$	$(1-\alpha)^5$	α^3	$0.1\alpha^4(\alpha \leq 0.3)$ $\alpha^6(\alpha > 0.3)$	$C_1(1-\alpha)^7\alpha(\frac{j_g}{\alpha} - \frac{j_l}{1-\alpha})^2$ $C_1 = 350\frac{\rho_l K}{\eta\sigma}(\rho_l - \rho_g)g$
Rahman[6]	$(1-\alpha)^3$	$(1-\alpha)^6$	Table 4.3		Table 4.4

Table 4.3: *Relative permeability and passability of Rahman model*[6].

Flow pattern	K_{rv}	η_{rv}
Bubbly & Slug	α^4	α^4
Transition	$\frac{\alpha^4}{1-W(1-\alpha)}$	$\frac{\alpha^4}{1-W(1-\alpha)}$
Annular	α^3	α^3

Table 4.4: *Interfacial friction utilized in the Rahman model*[6].

Flow pattern	F_i
Bubbly	$\frac{D_p}{0.012}(18C_1\alpha f j_r + 0.34C_2(1-\alpha)^3\alpha f^2\vert j_r\vert j_r)$
Slug	$\frac{D_p}{0.012}\left(5.21C_1\alpha j_r + 0.92C_2(1-\alpha)^3\vert j_r\vert j_r\right)$
Annular	$\frac{0.25D_p}{0.006^2}\left(\epsilon(1-\alpha)\left[\frac{\mu_g}{KK_{rg}}j_r + \frac{\rho_g}{\eta\eta_{rg}}\vert j_{r,ann}\vert j_{r,ann}\right]\right)$

$C_1 = \frac{\mu_l}{D_b^2}, C_2 = (\rho_l(1-\alpha) + \rho_v\alpha)/(\epsilon D_b),\ f = 0.5(1 + \frac{D_p}{D_b}ln(1 + \frac{2D_p}{D_b})$
Bubble diameter : $D_b = 1.35\sqrt{\frac{\sigma}{g(\rho_l - rho_v)}}$
Relative superficial velocity : $j_r = \frac{1-\alpha}{\alpha}j_v - j_l$
Relative superficial velocity for annular flow: $j_{r,ann} = j_v - \frac{\alpha}{1-\alpha}j_l$

Rahman[6] proposed flow pattern maps by modifying the by Tung & Dhir flow pattern map[5] by accounting for the differences in flow patterns due to particle sizes. The flow pattern map proposed is shown in Figure 4.17.

The importance of incorporating the interfacial friction between liquid and vapor phase was identified by Tutu[72] based on pressure drop experimental data. Rahman[6] utilized the interfacial drag according to the flow regime in the packed bed. The interfacial friction of the Rahman[6] model is presented in Table 4.4.

The governing equations were solved numerically by considering the difference in pressure between liquid and vapor phase as the capillary pressure in the porous bed as a function of local void fraction yielding,

$$P_c = \sigma\sqrt{\frac{\epsilon}{K}}J(\alpha) \tag{4.8}$$

where $J(\alpha)$ is the Leverett[73] function given by:

$$J(\alpha) = \frac{((1-\alpha)^{-1} - 1)^{0.175}}{\sqrt{5}} \tag{4.9}$$

Under an isotropic packed bed assumption, with a constant single phase porosity and permeability in all directions, the governing equations can be solved at a given Volumetric

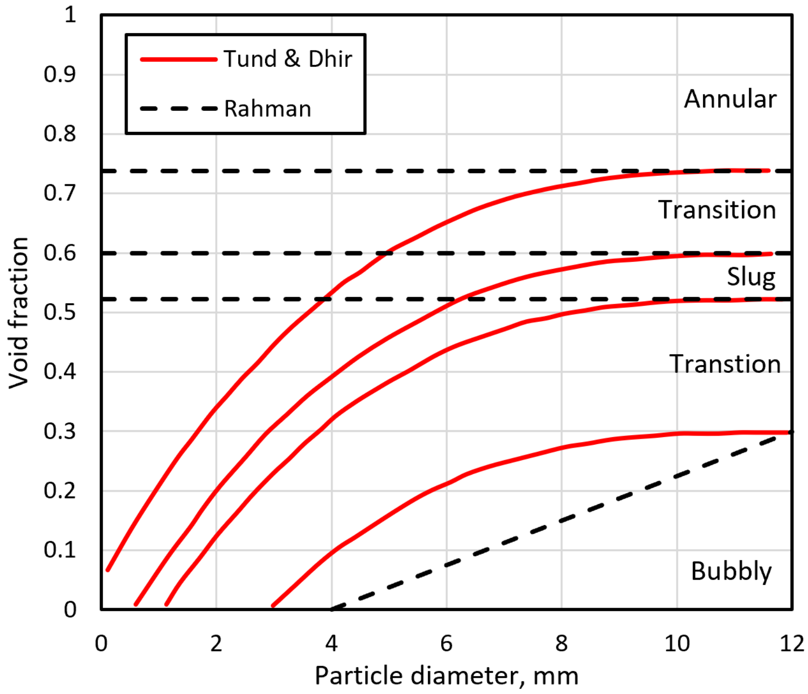

Figure 4.17: *Flow pattern boundaries in packed bed as a function of particle diameter and void fraction by the classical T&D*[5] *and Rahman*[6] *model.*

heat generation rate, Q, to yield the void fraction profile within the debris bed. The governing equations were solved iteratively at incrementing heat generation rates to obtain the dryout heat flux, which is indicated by the local void faction in the bed reaching a value of unity. This variation of void fraction with bed height, and the onset of dryout as predicted by the model, was shown previously in Figure 3.2.

4.4.2 Void fraction comparison

The axial variation of void fraction as measured through neutron imaging were compared to the classical Lipinski[7] model in Figure 4.18. In the model, the subcooled length L_{sub} is incorporated, which is given by,

$$\frac{L_{sub}}{H} = \frac{C_p \Delta T_{sub}}{h_f g} \tag{4.10}$$

where ΔT_{sub} is the subcooling of the liquid entering the bed. Within the saturated boiling region, good agreement between the model and experiment is observed.

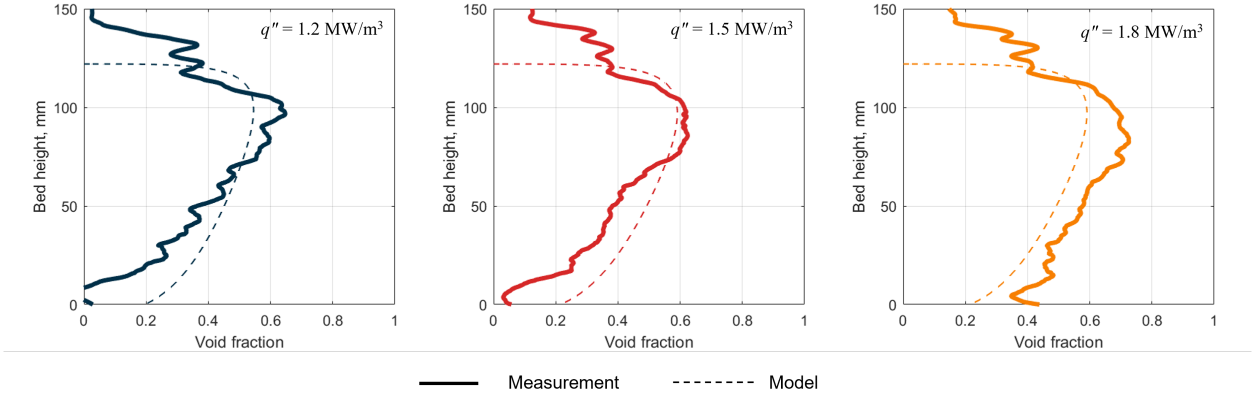

Figure 4.18: *Axial variation of void fraction for measurements shown in Figure 4.2. The measurements are compared with the predictions of Lipinski 1D*[7] *model.*

Figure 4.19 shows the comparison of the predicted void fraction with the measurements, spatially averaged over 2 mm, at various elevations in the test section. The models predict the overall trend of the void fraction, in the pre-dryout region, but overpredict the heat flux at which dryout occurs. The Rahman[6] model, involving the interfacial friction as a parameter of the flow regime of the two phase flow, gives the closest prediction with respect to the dryout. The impact of only involving the interfacial friction independent of the flow regime leads to an overprediction of the dryout heat flux, as the interfacial friction increases significantly when the flow is in an annular regime, especially at high void fractions. Including the effect of the flow regime is done by flow regime specific interfacial friction and relative permeabilities. This however leads to an overprediction of the void fraction, but leads to accurate prediction of the dryout heat flux. Although large uncertainty in the prediction of the dryout heat flux exists in various studies in literature leading to conservative estimates in design of safety systems. The accurate high spacial resolution void fraction data presented in this paper can assist the modelers in validating their refined models. These models may include detailed modeling of the bubble characteristics and their coalescence due to the stochastic nature of the pore size and shape in the porous media.

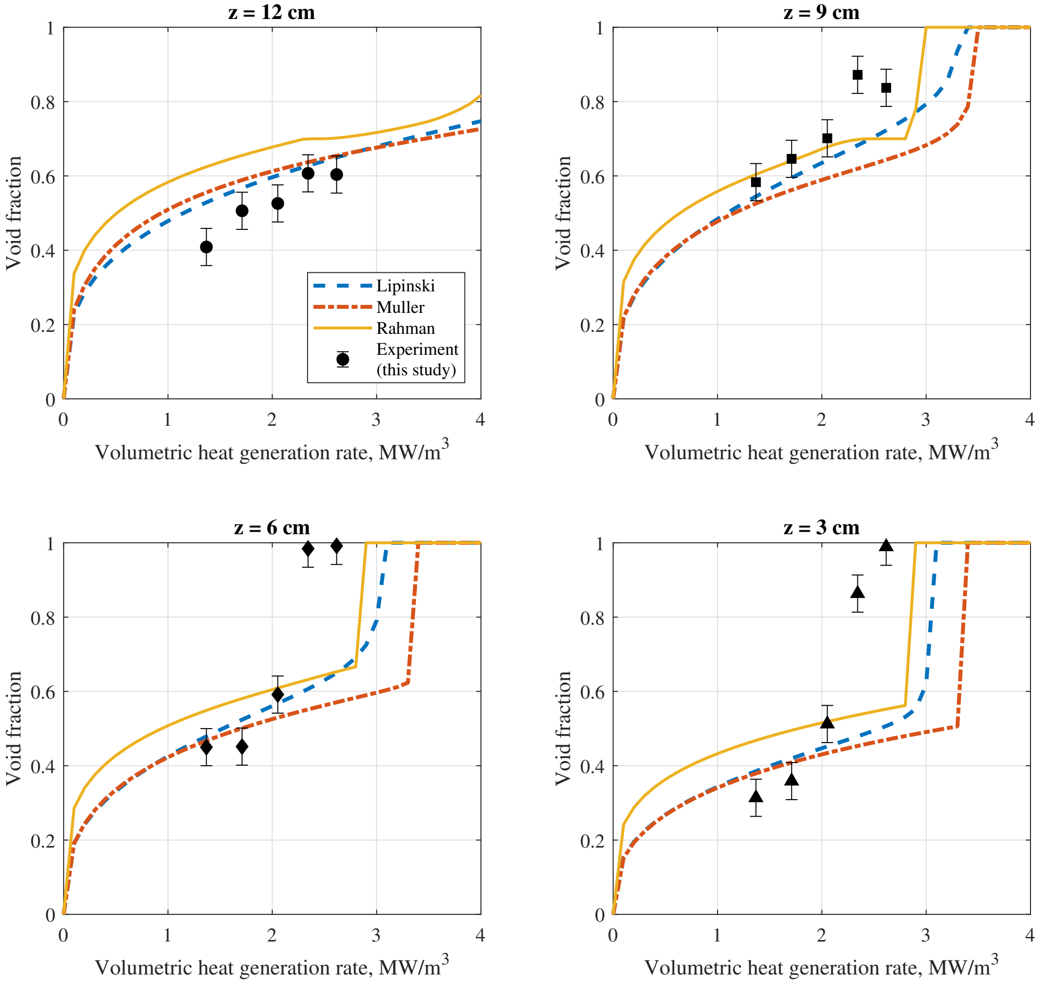

Figure 4.19: *Comparison of the measured void fraction at various locations with Lipinski*[7]*, Muller*[8]*, and Rahman*[6] *models.*

4.5 Conclusions

Experiments with an inductively heated particle bed with a focus on the coolability limits have been carried out. The measurement of the dryout process for pure water using the high resolution temperature sensor shows that the dryout heat flux reduces with an increase in the total bed height and the occurrence of the dry spot is dependent on the degree of excessive heat beyond the dryout heat flux in the packed bed.

The measurement of dryout process for pure water shows a steep increase in temperature and a drop in pressure during the dryout process. Experiments with varying degrees of excessive heat above the dryout heat flux show that the location of occurrence of dryout increases in elevation within the packed bed as the heat flux above dryout heat flux is increased.

A comparison of the cooling performance between pure water and water with added salts in a range of concentrations 0% - 7% show that the dryout heat flux increases with an increase in the concentration of the dissolved salts. This increase in dryout heat flux could be attributed to a reduction in pressure drop characteristics with concentration due to the formation of smaller bubbles and lack of bubble coalescence in homogeneous flow found in salt water. Further modeling of the pressure drop characteristics with addition of salts is required.

For stable cooling conditions where the heat flux is below the critical dryout heat flux, a gradual increase in temperature is observed. The crystallization fouling process causes the pores at a certain cross section in the debris bed to plug and this can cause a build up of pressure in the lower regions of the debris bed.

This implies that using salt water can enhance the coolability of debris beds for a short amount of time, and longterm cooling with salt water causes fouling of the dissolved salts. This causes the coolability to deteriorate over time, until the point of complete plugging of a cross section, beyond which, further complications can be expected due to the pressure build up in the debris bed. These limiting cooling mechanisms- the dryout and the fouling mechanism, should be considered when seawater is injected into the reactor core to cool the decay heat generated by the debris beds. The pressure drop characteristics and the fouling process in a boiling debris bed will be investigated in future research activity.

The TRIGA Mark-II reactor at Kansas State University was utilized to measure the void fraction in a boiling particle bed heated via an induction heater. Neutron images were taken at several elevations in the test section and stitched to generate a complete void fraction profile across the axial length of the test section. The void fraction increased along the height of the test section. The overall void fraction increases with the heat input into the test section. The measured steady state void fraction was compared with predictions from various model and a good agreement between them was obtained.

Chapter 5

Conclusions and Future Work

Assessing the feasibility of seawater cooling on Nuclear Reactors during accidents is important as many reactors are located next to large water bodies and oceans. The presence of dissolved salts in water complicates the understanding of coolability, especially during boiling because the dissolved salts can affect the hydrodynamics of the flow and can also precipitate out and deposit on surfaces, thereby adding thermal and hydraulic resistance. This is further complicated in a heat generating porous debris bed. The work presented in this thesis sheds light on the cooling performance of seawater in two geometries- an annulus and an emulated packed bed.

The heat transfer coefficient during flow boiling in a vertical annulus was measured at varying heat fluxes. Transient evolution of the heat transfer coefficient in saturated boiling and subcooled boiling was determined. These measurements were coupled with quantified bubble departure characteristics to estimate the evaporative heat flux. Seawater was shown to have a lower evaporative heat flux as compared to pure water during subcooled boiling. Correspondingly, the heat transfer rates were also reduced in the subcooled boiling region in seawater. A frothy homogeneous two phase flow with a lack of bubble coalescence was observed with seawater. X-ray radiography was utilized to quantify the void fraction in the two phase flow. The measurements indicated a higher void fraction in seawater as compared to pure water, due to the hydrodynamics of the frothy flow causes by the reduced bubble rise velocity. A pressure drop model was used to predicted the total pressure drop across the test section by using void fraction measurements from X-rays radiography. A good agreement between model prediction and experimental measurements was obtained for pure water. For seawater, a higher contribution of the frictional resistance to the total pressure drop was obtained. To accurately model the pressure drop in seawater, generic pressure drop models need to be modified to to incorporate the characteristics of frothy flows in the future.

An emulated debris bed experimental setup consisting of a packed bed test section was designed and built using data from large scale FCI experimental reports. Design considerations for the experiment also included constraints from accommodation of the SWI-DTS system and neutron imaging for void fraction quantification. The SWI-DTS system provided high spatio-temporal resolution thermal response of the debris bed during steady state and transient boiling. Non-intrusive void fraction measurement utilizing thermal neutrons from the KSU Triga reactor were used to quantify the vapor fraction within the pores of the boiling debris bed. First of a kind void fraction measurements inside the boiling debris bed were presented and various models were compared with the experimental data. The dependence of the limiting dryout heat flux on various parameters was investigated. Increasing the height of the debris bed reduced the dryout heat flux. Increasing the excessive superheat increased the elevation at which dryout occurred. Contrary to expectations, increasing the concentration of the dissolved salts increased the dryout heat flux. The presence of salts also deteriorated the heat transfer over time due to salt deposition on the particles, until the pores were plugged in the debris bed and rendered the bed uncoolable. These observations indicate an enhanced cooling with seawater in a debris bed temporarily, but the presence of salts created long term issues with plugging of the pores, that can prove to be detrimental in exacerbating the severe nuclear accident. The well known classical models for estimating two phase flow void fraction in a debris bed were validated for the first time using neutron imaging.

Future work on debris bed coolability can include quantifying the dryout heat fluxes with varying particle size diameters as the monodispersed packed bed used in this study poses certain approximations and may lead to acceleration of the accident, especially due to the salt deposition in smaller sized pores. The longterm thermal response of the debris bed under varying parametric conditions should be also investigated.

Modeling the cooling performance of seawater in debris beds should utilize appropriate flow regime transition criteria as the transition from bubbly to slug flow is extended to higher vapor fraction and vapor flux in seawater. The simpler models that do not incorporate the flow regime effects are inaccurate in predicting the cooling limits of seawater in a debris bed. Focused effort on developing models that incorporate the enhanced cooling and longterm coolability of using seawater in a debris bed need to be evaluated. These models can be validated using the experimental data provided in this study.

References

[1] Zayed Ahmed, Chance Jordan, Prashant Jain, Kevin Robb, Hitesh Bindra, and Steven J Eckels. Experimental investigation on the coolability of nuclear reactor debris beds using seawater. *International Journal of Heat and Mass Transfer*, 184:122347, 2022.

[2] K.E. Gungor and R.H.S. Winterton. A general correlation for flow boiling in tubes and annuli. *International Journal of Heat and Mass Transfer*, 29(3):351–358, 1986.

[3] M.M. Shah. A new correlation for heat transfer during boiling flow through pipes. *ASHRAE transactions*, 82(2):66–68, 1976.

[4] Mohammed Shah. Chart correlation for saturated boiling heat transfer: equations and further study. *ASHRAE transactions*, 88:185–195, 1982.

[5] VX Tung and VK Dhir. A hydrodynamic model for two-phase flow through porous media. *International journal of multiphase flow*, 14(1):47–65, 1988.

[6] Saidur Rahman. Coolability of corium debris under severe accident conditions in light water reactors. 2013.

[7] Ronald J Lipinski. A coolability model for postaccident nuclear reactor debris. *Nuclear technology*, 65(1):53–66, 1984.

[8] T Schulenberg and U Müller. An improved model for two-phase flow through beds of coarse particles. *International journal of multiphase flow*, 13(1):87–97, 1987.

[9] Mostafa H Sharqawy, John H Lienhard, and Syed M Zubair. Thermophysical properties of seawater: a review of existing correlations and data. *Desalination and water Treatment*, 16(1-3):354–380, 2010.

[10] MJ J Atkinson, C Bingman, P O Box, C Bingman, and P O Box. Elemental composition of commercial seasalts. *Journal of Aquariculture and Aquatic Sciences*, VIII(2):39–43, 1997. ISSN 1939-3210. doi: 10.1080/19393210.2010.520340. URL `http://www.rudyv.be/Aquarium/sels.pdf`.

[11] Mirza Shah. A new correlation for heat transfer during boiling flow through pipes. 1976.

[12] Randall Gauntt, Donald Kalinich, Jeff Cardoni, Jesse Phillips, Andrew Goldmann, Susan Pickering, Matthew Francis, Kevin Robb, Larry Ott, Dean Wang, et al. Fukushima daiichi accident study (status as of april 2012). *Sandia Report Sand*, 6173, 2012.

[13] Ritsuo Yoshioka and Kenji Iino. Technical report: Fukushima accident summary (aug. 19, 2011). *Association for the Study of Failure*, 2011.

[14] Joon-Eon Yang. Fukushima dai-ichi accident: lessons learned and future actions from the risk perspectives. *Nuclear Engineering and Technology*, 46(1):27–38, 2014.

[15] Aranyak Chakravarty, Priyankan Datta, Koushik Ghosh, Swarnendu Sen, and Achintya Mukhopadhyay. Coolability of heat-generating porous debris beds in severe accident situations. In *Two-Phase Flow for Automotive and Power Generation Sectors*, pages 305–336. Springer, 2019.

[16] Neil E Todreas and Mujid S Kazimi. *Nuclear systems volume I: Thermal hydraulic fundamentals*. CRC press, 2021.

[17] Abbas Helalizadeh, H Müller-Steinhagen, and M Jamialahmadi. Mixed salt crystallisation fouling. *Chemical Engineering and Processing: Process Intensification*, 39(1): 29–43, 2000.

[18] Daniel Franken, Zayed Ahmed, Seth Eckels, Steven Eckels, and Hitesh Bindra. Impact of dissolved salts on two-phase flow and boiling heat transfer in a natural circulation loop. *Chemical Engineering Science*, 206:463–470, 2019.

[19] Frank J Millero, Rainer Feistel, Daniel G Wright, and Trevor J McDougall. The composition of standard seawater and the definition of the reference-composition salinity scale. *Deep Sea Research Part I: Oceanographic Research Papers*, 55(1):50–72, 2008.

[20] Lawrence A Hardie and Hans P Eugster. Evaporation of seawater: calculated mineral sequences. *Science*, 208(4443):498–500, 1980.

[21] M Babel and BC Schreiber. 9.17-geochemistry of evaporites and evolution of seawater. *Treatise on geochemistry*, pages 483–560, 2014.

[22] Chr Balarew. Solubilities in seawater-type systems: Some technical and environmental friendly applications. *Pure and applied chemistry*, 65(2):213–218, 1993.

[23] Theodore Reginald Bott. *Fouling of heat exchangers*. Elsevier, 1995.

[24] SH Najibi, H Mu¨ ller Steinhagen, and M Jamialahmadi. Calcium carbonate scale formation during subcooled flow boiling. 1997.

[25] A. B. Helali. Effects of water contamination on sub-cooled flow boiling heat transfer. *Energy Conversion and Management*, 52(5):2288–2295, 2011. ISSN 01968904. doi: 10.1016/j.enconman.2010.11.025. URL `http://dx.doi.org/10.1016/j.enconman.2010.11.025`.

[26] AB Helali. Effects of water contamination on sub-cooled flow boiling heat transfer. *Energy conversion and management*, 52(5):2288–2295, 2011.

[27] Mohammad Mohsen Sarafraz and Faramarz Hormozi. Experimental studies on the effect of water contaminants in convective boiling heat transfer. *Ain Shams Engineering Journal*, 5(2):553–568, 2014.

[28] Zayed Ahmed, Seth Eckels, Steven J Eckels, and Hitesh Bindra. Forced convective boiling in a vertical annular test section with seawater coolant. *Journal of Nuclear Engineering and Radiation Science*, 7(3):031405, 2021.

[29] Yuanjie Li, Shuai Ren, Shiwei Zhang, Xingchi Jiang, and Chin Pan. Subcooled flow boiling of seawater in a vertical annulus. *International Journal of Heat and Mass Transfer*, 164:120591, 2021.

[30] M Jamialahmadi, A Helalizadeh, and H Müller-Steinhagen. Pool boiling heat transfer to electrolyte solutions. *International Journal of Heat and Mass Transfer*, 47(4):729–742, 2004.

[31] Tzu-Chen Huang and Chin Pan. Pool boiling in seawater, nacl solution and de-ionized water. *Nuclear Engineering and Design*, 344:46–53, 2019.

[32] M Jamialahmadi, R Blöchl, and H Müller-Steinhagen. Bubble dynamics and scale formation during boiling of aqueous calcium sulphate solutions. *Chemical Engineering and Processing: Process Intensification*, 26(1):15–26, 1989.

[33] Wei Liu, Taku Nagatake, Kazuyuki Takase, Hiroyuki Yoshida, and Fumihisa Nagase. Research of seawater effects on thermal-hydraulic behavior at severe accident: 1—research plan and results of preliminary experiments. In *International Conference on Nuclear Engineering*, volume 55812, page V004T09A108. American Society of Mechanical Engineers, 2013.

[34] Seyed Hesam Najibi. *Heat transfer and heat transfer fouling during subcooled flow boiling for electrolyte solutions.* University of Surrey (United Kingdom), 1997.

[35] SH Najibi, H Müller-Steinhagen, and M Jamialahmadi. Boiling and nonboiling heat transfer to electrolyte solutions. *Heat transfer engineering*, 17(4):46–63, 1996.

[36] Nilanjana Basu, Gopinath R Warrier, and Vijay K Dhir. Wall heat flux partitioning during subcooled flow boiling: Part 1—model development. *J. Heat Transfer*, 127(2): 131–140, 2005.

[37] Gopinath R Warrier and Vijay K Dhir. Heat transfer and wall heat flux partitioning during subcooled flow nucleate boiling—a review. 2006.

[38] Patrick Schäfer, Manfred Groll, and Rudi Kulenovic. Basic investigations on debris cooling. *Nuclear engineering and design*, 236(19-21):2104–2116, 2006.

[39] Bernd Schwinges, C Journeau, T Haste, L Meyer, W Tromm, K Trambauer, et al. Ranking of severe accident research priorities. *Progress in Nuclear Energy*, 52(1):11–18, 2010.

[40] N Chikhi, O Coindreau, LX Li, WM Ma, Veikko Taivassalo, Eveliina Takasuo, S Leininger, R Kulenovic, and E Laurien. Evaluation of an effective diameter to study quenching and dry-out of complex debris bed. *Annals of Nuclear Energy*, 74:24–41, 2014.

[41] K Hu and TG Theofanous. On the measurement and mechanism of dryout in volumetrically heated coarse particle beds. *International journal of multiphase flow*, 17(4): 519–532, 1991.

[42] G Hofmann. On the location and mechanisms of dryout in top-fed and bottom-fed particulate beds. *Nuclear Technology*, 65(1):36–45, 1984.

[43] Ilona Lindholm, Stefan Holmström, Jaakko Miettinen, V Lestinen, J Hyvärinen, Pekka Pankakoski, and H Sjövall. Dryout heat flux experiments with deep heterogeneous particle bed. *Nuclear engineering and design*, 236(19-21):2060–2074, 2006.

[44] Shinichiro Uesawa, Wei Liu, Lifang Jiao, Taku Nagatake, Kazuyuki Takase, Mitsuhiko Shibata, and Hiroyuki Yoshida. Effect of seawater on heat transfer without boiling in internally heated annulus. *Nippon Genshiryoku Gakkai Wabun Ronbunshi (Online)*, 15 (4):183–191, 2016.

[45] Shibata Nagatake Uesawa, Koizumi and Yoshida. Study on forced convective boiling heat transfer of seawater with sea salt deposits. *Multiphase flow*, 31(2):162–170, 2017.

[46] Mohammad Mohsen Sarafraz and Faramarz Hormozi. Experimental studies on the effect of water contaminants in convective boiling heat transfer. *Ain Shams Engineering*

Journal, 5(2):553–568, 2014. ISSN 20904479. doi: 10.1016/j.asej.2013.11.006. URL `http://dx.doi.org/10.1016/j.asej.2013.11.006`.

[47] J Fernández-Seara, FJ Uhia, and J Sieres. Laboratory practices with the wilson plot method. *Experimental heat transfer*, 20(2):123–135, 2007.

[48] Peter Kovesi. Matlab functions for computer vision and image analysis, 2004.

[49] Donald F Swinehart. The beer-lambert law. *Journal of chemical education*, 39(7):333, 1962.

[50] Dasari Rao Mohamed S., El-Genk. Heat transfer experiments and correlations for low-reynolds-number flows of water in vertical annuli. *Heat transfer engineering*, 10(2): 44–57, 1989.

[51] Raúl Martínez-Cuenca, Caleb S Brooks, J Enrique Juliá, Takashi Hibiki, and Mamoru Ishii. Stochastic nature of wall nucleation and its impact on the time average boundary condition. *Journal of Heat Transfer*, 137(2), 2015.

[52] Zhiee Jhia Ooi, Vineet Kumar, Joseph L Bottini, and Caleb S Brooks. Experimental investigation of variability in bubble departure characteristics between nucleation sites in subcooled boiling flow. *International Journal of Heat and Mass Transfer*, 118:327–339, 2018.

[53] Mostafa H. Sharqawy, John H. Lienhard, and Syed M. Zubair. The thermophysical properties of seawater : A review of existing correlations and data. *Desalination and water treatment*, 16:354–380, 2013.

[54] Kishor G. Nayar, Mostafa H. Sharqawy, Leonardo D. Banchik, and John H. Lienhard. Thermophysical properties of seawater: A review and new correlations that include pressure dependence. *Desalination*, 390:1–24, 2016. ISSN 00119164. doi: 10.1016/j.desal.2016.02.024.

[55] Junping Gu, Yuxin Wu, Guoli Tang, Qinggong Wang, and Junfu Lyu. Experimental study of heat transfer and bubble behaviors of NaCl solutions during nucleate flow boiling. *Experimental Thermal and Fluid Science*, 109(109907), 2019.

[56] RM Summers, RK Cole Jr, EA Boucheron, MK Carmel, SE Dingman, and JE Kelly. Melcor 1. 8. 0: A computer code for nuclear reactor severe accident source term and risk assessment analyses. Technical report, Nuclear Regulatory Commission, Washington, DC (USA). Div. of Systems . . . , 1991.

[57] Manfred Bürger, Michael Buck, Werner Schmidt, and Walter Widmann. Validation and application of the wabe code: investigations of constitutive laws and 2d effects on debris coolability. *Nuclear engineering and design*, 236(19-21):2164–2188, 2006.

[58] M Buck, M Bürger, S Rahman, and G Pohlner. Validation of the mewa model for quenching of a severely damaged reactor core. Technical report, 2011.

[59] Patrick Schäfer, Manfred Groll, and Rudi Kulenovic. Basic investigations on debris cooling. *Nuclear engineering and design*, 236(19-21):2104–2116, 2006.

[60] Liangxing Li, Weimin Ma, and Sachin Thakre. An experimental study on pressure drop and dryout heat flux of two-phase flow in packed beds of multi-sized and irregular particles. *Nuclear engineering and design*, 242:369–378, 2012.

[61] K Atkhen and G Berthoud. Silfide experiment: Coolability in a volumetrically heated debris bed. *Nuclear Engineering and Design*, 236(19-21):2126–2134, 2006.

[62] PP Kulkarni, M Rashid, R Kulenovic, and AK Nayak. Experimental investigation of coolability behaviour of irregularly shaped particulate debris bed. *Nuclear engineering and design*, 240(10):3067–3077, 2010.

[63] K Atkhen and G Berthoud. Silfide experiment: Coolability in a volumetrically heated debris bed. *Nuclear Engineering and Design*, 236(19-21):2126–2134, 2006.

[64] BW Spencer, K Wang, CA Blomquist, LM McUmber, and JP Schneider. Fragmentation and quench behavior of corium melt streams in water. Technical report, Nuclear Regulatory Commission, Washington, DC (United States). Div. of . . . , 1994.

[65] I Huhtiniemi and D Magallon. Insight into steam explosions with corium melts in krotos. *Nuclear Engineering and Design*, 204(1-3):391–400, 2001.

[66] D Magallon. Characteristics of corium debris bed generated in large-scale fuel-coolant interaction experiments. *Nuclear Engineering and Design*, 236(19-21):1998–2009, 2006.

[67] Jin Ho Song, Seong Wan Hong, Jong Hwan Kim, Young Jo Chang, Yong Seung Shin, Beong Tae Min, and Hee Dong Kim. Insights from the recent steam explosion experiments in troi. *Journal of nuclear science and technology*, 40(10):783–795, 2003.

[68] Aram Karbojian, WM Ma, Pavel Kudinov, and Truc-Nam Dinh. A scoping study of debris bed formation in the defor test facility. *Nuclear Engineering and Design*, 239(9): 1653–1659, 2009.

[69] Valery Rudnev, Don Loveless, and Raymond L Cook. *Handbook of induction heating*. CRC press, 2017.

[70] Sabri Ergun. Fluid flow through packed columns. *Chem. Eng. Prog.*, 48:89–94, 1952.

[71] Ronald J Lipinski. A coolability model for postaccident nuclear reactor debris. *Nuclear technology*, 65(1):53–66, 1984.

[72] NK Tutu, T Ginsberg, and JC Chen. Interfacial drag for two-phase flow through high permeability porous beds. 1984.

[73] MoC Leverett. Capillary behavior in porous solids. *Transactions of the AIME*, 142(01): 152–169, 1941.

[74] Robert J Moffat. Describing the uncertainties in experimental results. *Experimental thermal and fluid science*, 1(1):3–17, 1988.

[75] Vincent Aeschlimann, Stéphane Barre, and Samuel Legoupil. X-ray attenuation measurements in a cavitating mixing layer for instantaneous two-dimensional void ratio determination. *Physics of Fluids*, 23(5):055101, 2011.

Appendix A

Uncertainty analysis and error propogation

This section presents the uncertainty of instrumentation and computes the propagation of uncertainty for computed quantities. Table A.1 contains the uncertainty of various instrumentation deployed in the system. The uncertainties of the experimental results are analyzed by the procedures proposed by Moffat[74]. The method is based on careful specifications of the uncertainties in the various primary experimental measurements.

Table A.1: *Instrumentation uncertainty*

Instrumentation	**Uncertainty**
Emerson Coriolis Flow Meter	±0.03 g/s
Emerson Conductivity Probe	±4% of reading
Type K Thermocouples	±0.2°C
RTD probes	±0.1 °C
Pressure Transducers	±0.4% FS
Heater power input	±5 W

The calculated uncertainties in various measured quantities are summarized in Table A.2 below. The following section expands on the details of the analysis.

In the annular experimental setup, the uncertainty in the heat transfer coefficient through the heater wall, ($q'' = h\Delta T$) is dominated by the uncertainty in the wall temperature measurement and the inlet temperature measurement, and is given by,

$$\delta\Delta T = \sqrt{\delta T_{TC}^2 + \left(\frac{\delta\dot{m}}{\dot{m}}(\frac{\pi d Q z}{\dot{m} C_p A})\right)^2 + \delta T_{li}^2} \tag{A.1}$$

The corresponding uncertainty in heat transfer coefficient is calculated as,

$$\frac{\delta h}{h} = \frac{\delta\Delta T}{\Delta T} \tag{A.2}$$

For estimating the uncertainty in the mean bubble parameters, the standard error of 1 standard deviation was used.

For estimating the void fraction uncertainty, the procedure described by Aeschlimann[75] was used. The measured intensity by the detector corresponds to the number of photons detected during the imaging period. This number of photons follows a Poisson law, and statistical uncertainties on the void fraction due to photons statistics is given by,

$$\sigma_\alpha^2 = \left[\frac{ln\left(\frac{I_\alpha}{I_0}\right)}{I_0\left(ln\left(\frac{I_0}{I_1}\right)\right)^2}\right]^2 \sigma_{I_0}^2 + \left[\frac{ln\left(\frac{I_0}{I_\alpha}\right)}{I_1\left(ln\left(\frac{I_0}{I_1}\right)\right)^2}\right]^2 \sigma_{I_1}^2 + \left[\frac{1}{I_\alpha\left(ln\left(\frac{I_0}{I_1}\right)\right)^2}\right]^2 \sigma_{I_\alpha}^2 \tag{A.3}$$

where I_0 is the intensity at 100% void fraction, I_1 is the intensity at 0% void fraction, and I_α is the intensity of the two phase flow. The reference images with 0% and 100% void fraction were averaged over several frames, leading to a negligible corresponding uncertainties, $\sigma_{I_0}^2$ and $\sigma_{I_1}^2$. The calculated error in void fraction for X-ray imaging and neutron imaging was

Table A.2: *Uncertainty estimates of various measured quantities through error propagation*

Parameter	**Uncertainty**
Wall temperature difference, °C	±0.25
Heat transfer coefficient, W/m^{2}K	±100
Departure diameter, mm	±0.6
Nf	±1
Evaporative flux, W/m^2	±800
Void fraction - Xray imaging.	±3%
Temperature from OFDR, °C	±5
Dryout heat flux, MW/m^3	±0.2
Void fraction -neutron imaging	±5 %

calculated to be ±3% and ±5% respectively.

For estimating the uncertainty in the rest of the measurements, a standard error of 1 standard deviation around the mean was used. The uncertainty in the dryout heat flux was calculated based on the magnitude of the power steps taken.